The University of Nottingham

Highly active TiO_2-based photocatalaysts for indoor air remediation

GEORGE GREEN LIBRARY OF
SCIENCE AND ENGINEERING

Valeria Puddu

Thesis submitted to the University of Nottingham for the degree of Doctor of Philosophy

August 2008

ABSTRACT

Energy saving policies applied to modern buildings and air recirculation systems promote the build up of high levels of VOCs in indoor air. The growing concern related to the air quality in indoor environments requires the replacement of ineffective traditional purification methods, with an efficient and cost effective technology. Photocatalytic oxidation that utilise TiO_2, represents a promising candidate for this purpose. However, the formulation of photocatalysts that can efficiently utilise a sustainable energy source (i.e. solar light), still represents an ambitious target in this field.

In this study, different TiO_2-based photocatalysts were synthesised by modified sol-gel and/or hydrothermal routes. The materials were characterised by XRD, SEM, N_2 sorption (BET and BJH methods), UV-vis Spectroscopy and XPS. The photocatalytic activity of TiO_2-based materials was systematically investigated at different light intensities, in a gas-phase flat-plate photoreactor, using trichloroethylene (TCE) as model pollutant, and compared with that of the commercial product TiO_2 Degussa P-25.

This research provides insights into the influence of preparation parameters on different synthetical pathways for the preparation of highly active TiO_2-based photocatalysts. The general approach to this investigation is based on the study of the influence of several processing parameters on morphological, textural and crystallographic properties of the photocatalysts, in order to correlate the material's features with their photocatalytic properties.

The preparation of a wide range of pristine TiO_2 allowed assessing a clear correlation between phase composition and crystal size and the photocatalytic

performance. A series of highly active anatase photocatalysts was prepared. The best photocatalyst has an optimum crystal size of 28 nm and exhibits a photocatalytic activity that exceeds that of P-25 by a factor of over 2 times.

A new TiO_2/WO_3 nanocomposites with peculiar crystallographic properties of the W component was developed by a novel one-step hydrothermal synthesis. The synthesis conditions were optimised with respect to the photocatalytic activity.

Overall, the optimisation of the properties that enable an efficient interfacial charge transfer rate at the catalyst surface was found to be of fundamental importance for the design of improved TiO_2-based photocatalysts.

PUBLISHED PAPERS

The following papers based on the work reported in this thesis have been published in refereed journals or international conferences:

- PUDDU, V., MOKAYA, R. and LI PUMA, G., 2007. Novel one step hydrothermal synthesis of TiO_2/WO_3 nanocomposites with enhanced photocatalytic activity. **Chemical Communications**, (45), 4749-4751.

- PUDDU, V., CHOI H., LI PUMA, G. and DYONYSIOU, D. D., 2007. Gas phase photocatalytic decomposition of trichloroethylene by immobilized TiO_2 film reactor: effect of TiO_2 properties and UV light intensity. *In:* TiO2-12, 12th International Conference on TiO_2 Photocatalysis: Fundamentals & Applications, Niagara Falls, USA, 24-27 September 2007

- PUDDU, V., MOKAYA, R. and LI PUMA, G., 2007. Mesoporous TiO_2 photocatalysts with improved activity for trichloroethylene degradation. *In:* SP-2, Second International Conference on Semiconductor Photochemistry, Aberdeen, UK, 23-25 July 2007

At the time of writing, the following papers are in preparation:

- PUDDU, V., CHOI H., LI PUMA, G. and DYONYSIOU, D. D., 2008. TiO_2 photocatalysts for indoor air remediation: influence of crystallinity and UV light intensity on trichloroethylene photodegradation. Applied Catalysis B: Environmental
- PUDDU, V. & LI PUMA, G. 2008. Novel highly active TiO_2/WO_3 nanocomposites: synthesis optimisation and light intensity studies. Applied Catalysis B: Environmental
- PUDDU, V. & LI PUMA, G. 2008. Effect of synthesis parameters on photocatalytic activity of mesoporous TiO_2. Applied Catalysis B: Environmental.

ACKNOWLEDGEMENTS

My sincere gratitude goes to my Supervisor, Dr. Gianluca Li Puma, for giving me the opportunity to carry out this challenging research project and for motivating me during the course of this PhD.

Many people have contributed to the realization of this work. First of all, I would like to express my gratitude to Dr. Ignasi Salvado-Estivill that designed and built the photocatalytic reactor. I would also like to acknowledge the work of Dr. Hyeok Choy and Jenia Georgieva for preparing some of the samples tested.
Special thanks to Dave Clift for his help with XRD analysis, Martin Roe for the SEM imaging analysis, and all the technical stuff in Schee.
I also wish to express my appreciation to Professor Mokaya, for his help in interpreting the adsorption properties of my samples, and for his contribution to the published paper from this work.

A special thanks goes to Professor Marc Anderson and Dr. Isabel Tejedor-Tejedor for their hospitality at the University of Winsconsin, and for their contribution in making my stay in US an amazing experience.

I would like to acknowledge the Engineering and Physical Sciences Research Council (EPSRC) for the financial support, and the Business-Engineering and Science travel Scholarship (BEST).

All my friends in Nottingham deserve a special mention just for their friendship and support during the last four years: from all my colleagues in Schee to the Italian/Sardinian community in Nottingham, thank you everybody!

The last but the most important acknowledgement is for my family: my parents Raffaele and Ignazia and my lovely sister Claudia. Your love, support and faith in me are, and will always be, the moving forces for everything I do.

TABLE OF CONTENTS

Chapter 3- Analytical Techniques

Chapter 4- Methodology

Chapter 5- Pristine TiO_2

Chapter 8- Conclusions

LIST OF TABLES

LIST OF FIGURES

Chapter 1

Introduction

1.1. Indoor Air Quality (IAQ)

In the past few decades Indoor Air Quality (IAQ) has increased scientific and public interest in developed countries as a consequence of the growing incidence rate of respiratory diseases such as asthma, allergies, building related illness (BRI) and the so-called sick building syndrome (SBS). In the UK, the IAQ matter was officially acknowledged in 1991 when the House of Commons Select Committee published the Sixth Report on 'Indoor Pollution' containing the recommendation to "develop guidelines and code of practice for indoor air quality in buildings, which specifically identify exposure limits for an extended list of pollutants...". In 2004 the Committee of Medical Effects of Air Pollutant (COMEAP, 2004) set guidelines for most common indoor pollutants in home indoor environments. COMEAP guidelines provide some advice on how to minimise the production of indoor air pollution. They are aimed at individuals concerned about indoor air quality, and also at material manufactures, architects and engineers that are involved in building design.

Principal sources of indoor pollution are: tobacco smoke, combustion products from heating systems, particulates such as dust, microorganisms, moulds and Volatile Organic Compounds (VOCs). Infiltration of polluted air from outdoors can also be a pollution source, but the most characteristic components of indoor pollution are VOCs (Yu *et al*, 2008).

VOCs are a wide and heterogeneous class of organic chemicals including alcohols, aldehydes, aromatic compounds and halogenated compounds, that have in common a high vapour pressure, thus evaporate at ambient temperature and pressure conditions (Doucet *et al*, 2006). They are largely used in the

manufacturing process of furniture, carpet, building material and house holdings, and are slowly released from these sources to the surrounding environment (IEH, 2001). The use of cleaning products, deodorants and some human activities or hobbies contribute to increase the VOCs contamination loading in indoors. Moreover, energy saving policies applied to modern air recirculation systems reduce the ventilation rate and promotes the build up of high levels of indoor pollution (Yu *et al*, 2008) .

Usually, in indoor environments, VOCs concentrations are in the ppb or ppm range, however, during or after activities such as wall painting or paint stripping VOCs levels can reach levels up to 1000 times higher than outside (EPA, 2002).

Table 1.1 Examples of VOCs found in indoor air and their source materials.

Compound	Source material(s)
Formaldehyde	Pressed wood and insulation products, adhesives
p-dichlorobenzene	Moth crystals, room deodorants
Styrene	Insulation, textiles, disinfectants, plastics, paints
Benzene	smoking
Tetrachloroethylene, trichloroethane	Dry cleaned clothes, aerosol sprays, fabric protectors
Aromatic hydrocarbons (i.e. toluene, xylenes)	Paints, adhesive, gasoline
PAHs	Combustion products
Alcohols	Aerosols, window-cleaners, paints, cosmetics and adhesives
Ketones	Varnishes, polish remover, adhesives
Ethers	Resins, paints, dyes, soaps, cosmetics
Esters	Plastics, resins, plasticisers, flavours, perfumes

Some VOCs like benzene and formaldehyde have been classified as carcinogenic and their short and long term harmful effects on human health have been extensively demonstrated. The risk associated with pollution exposure is not just a function of pollutant concentration but also a function of

exposure length. Thus, considering that people spend most of their time in indoors, it is reasonable to assume that exposure to even extremely low concentrations of VOCs may have adverse effects on human health in the short or long term (EPA, 2002).

Three strategies are generally recommended to improve IAQ (EPA, 2002):

- Source control
- Ventilation improvement
- Air cleaners

Source control and ventilation improvements represent the most effective strategies to prevent the build up of dangerous pollution levels (Guo *et al*, 2003). However, not much can be done to reduce the ordinary emission from house holdings and fittings normally installed in houses and buildings. Thus, the use of air cleaners as supporting remediation solution is highly recommended in those environments where natural ventilation is not possible (Kim *et al.*, 2008).

The air cleaning systems available in the market are usually designed to remove particles by mechanical filtration, and to adsorb gaseous contaminants on solid adsorbents like activated carbon or specifically developed chemisorbents able to remove specific compounds or class of compounds (Metts and Batterman, 2006). However, information available on the effectiveness of these adsorption devices for removal of gaseous contaminants at indoor concentrations are limited (Yu *et al*, 2008). Moreover, the adsorption technology employed in commercial devices for indoor air purification does not represent a definitive solution to the issue. In fact, the pollutants are only

transferred from the air to the absorbent, which thus requires further treatment before disposal (EPA, 2002).

1.2. Advanced Oxidation technology (AOTs) for Air Remediation

Since classic remediation technologies based on filtration and adsorption are proving to be insufficient to achieve adequate air cleaning, the development of an effective and environmentally friendly solution must be accomplished.

Advanced Oxidation Technologies (AOTs) are one of the main remediation technologies for water purification, and have been considered also for application in air treatment. AOTs involve the *in situ* production of free radicals, mainly hydroxyl and peroxyl, which are characterised by strong oxidative power. These radicals can initiate radical chain reactions on organic substrates, leading to the complete mineralisation of organic compounds to CO_2 and H_2O. AOTs usually can achieve a higher degree of mineralization compared with traditional chemical oxidation (i.e. peroxidation) and are effective also for refractant chemicals (Dhananjay S Bhatkhande, 2002).

Among AOTs, ozonation has found some commercial application in air cleaning devices (EPA, 2008). Ozonation is based on a photolytic oxidation process, where radicals are produced by a reaction between high-energy photons and ozone, and have been widely used for purification of wastewater (Gogate and Pandit, 2004). However, the recognised irritant properties of ozone at high concentration increase the safety concerns regarding devices that employ this system. Moreover, scientific evidences show that ozone has little

potential to remove indoor air contaminants at concentrations that do not exceed public health standards (EPA, 2008).

1.3. Photocatalysis for indoor air remediation

Photocatalysis represents a cheaper and safer alternative to ozonation and its potential as a remediation technology for polluted air is well established. As will be extensively reported in the Literature review of this thesis, titania based materials show the best performance at laboratory scale for VOCs remediation.

Much of the work available in literature focuses on the study of the reaction mechanism through identification of reaction intermediates as well as development and validation of kinetic models. However, to allow extensive commercialisation and utilisation of photocatalysis at industrial scale, the efficiency of the systems must be optimised and made economically feasible.

From an engineering point of view, the reactor design optimisation is a crucial point. Different reactor configurations with different scale levels have been investigated and in many cases mathematical models have been applied to predict and control the photocatalytic efficiency. However, for practical applications the optimisation of the photocatalytic material employed in the photocatalytic process is also very important. Indeed, the development of improved photocatalysts represents a dynamic and challenging aspect of research in the field of applied photocatalysis.

The main drawback of TiO_2 as photocatalyst is the continuous requirement of UV light that activates the catalyst, thus starting the photocatalytic reaction. This requirement increases the overall cost of a photocatalytic process. An ideal photocatalyst would be activated by solar illumination, therefore be able

to work under this natural and renewable form of energy. Another disadvantage of titania is its fast electron-hole recombination rate that reduces the photocatalytic activity. In order to optimise the material's photocatalytic properties, two approaches can be used:

1) The extension of absorption spectrum of the catalyst into the visible range usually by means of doping
2) The development of catalyst with improved efficiency under UV light

Both effects can be obtained by modifying the structural and electronic characteristics of the materials employed as will be extensively described in this thesis.

1.4. Aims of the Project

Principal aim of this research project is the production, comparison and optimisation of titania based photocatalysts with improved activity for photooxidation in the gas phase of volatile organic compounds under UV and/or visible radiation. Trichloroethylene (TCE) was chosen as probe pollutant.

To achieve the above aims the following objectives have been investigated:

- To develop TiO_2-based nanomaterials, using sol-gel, modified sol-gel and hydrothermal methods.
- To characterise the physical and morphological properties of synthesised photocatalyst.
- To study the effect of various synthesis parameters on crystallographic and structural properties of the catalysts.

- To investigate the photocatalytic properties of synthesised TiO_2 in a gas phase flat plate photoreactor using TCE as model pollutant.
- To compare synthesised TiO_2-based photocatalyst with photocatalytic activity of commercial TiO_2 Degussa P-25.
- To study the correlation between structural and crystallographic properties of the photocatalysts and their photocatalytic activity.

1.5. Thesis Outline

The present thesis is composed of eight chapters.

Chapter 1- Introduction.

Chapter 2- Literature Review - an overview of several topics that have been studied to carry out this research project is reported. The general principles of photocatalysis as AOP and the characteristics and properties of TiO_2 as photocatalyst are reported. Principles of Sol-gel chemistry and hydrothermal synthesis for synthesis of nanomaterials are introduced along with TiO_2 modification by doping and coupling effects with other semiconductors are discussed and relevant literature outcomes presented. Also an overview of photocatalytic reactors employed gas-phase photocatalysis is outlined.

Chapter 3- Analytical techniques- deals with a brief description of theory and application of the major analytical techniques adopted during this work.

Chapter 4- Methodology – A detailed description of photocatalysts synthesis and characterisation procedures are presented. Also, the specifications and the optimisation of the gas-phase photocatalytic reactor

used, as well as experimental conditions employed during evaluation of the catalysts are reported.

In Chapters 5, 6 and 7 report the experimental evidences and the discussion of the results for three different sets of TiO_2 samples.

Chapter 5- Pristine TiO_2- the preparation, characterisation and photocatalytic activity of pristine TiO_2 nanoparticles obtained by modified sol-gel methods are reported. The impact of different hydrolysis-condensation conditions and crystallisation processes on material properties and photocatalytic activity have been evaluated and discussed.

Chapter 6- Nitrogen doped TiO_2 - reports the work carried out in the attempt to develop doped TiO_2 active under visible light.

Chapter 7- TiO_2/WO_3 systems- describes the studies on TiO_2/WO_3 photocatalysts. The first part concerns studies carried out on a TiO_2/WO_3 layered system. The second part describes the development and optimisation of hydrothermal synthesis for novel TiO_2/WO_3 nanocomposites with high activity.

Chapter 8 - Conclusions and recommendations- presents a summary of the research outcomes and provides recommendations for future work on the topic.

Chapter 2

Literature review

2.1 Introduction to Heterogeneous Photocatalysis

Photocatalysis is defined as "a change in the rate of chemical reactions, or their generation, under the action of light in the presence of substances — *photocatalysts* that absorb light quanta and are involved in chemical transformations of the reaction participants" (IUPAC, 2007). This definition by IUPAC combines photochemistry and catalysis and it can apply to any chemical reaction where light and a catalyst are necessary to achieve or to accelerate a chemical transformation as described by Eq. 2.1. (Parmon *et al.*, 2002). Like classic catalysis, the catalyst is regenerated in its original chemical state, at the end of the catalytic cycle.

$$A + h\nu + Cat \rightarrow B + Cat \qquad \text{(Eq. 2.1)}$$

Photocatalytic processes can be classified as homogeneous or heterogeneous. Homogeneous processes are carried out in single-phase system (liquid) and the catalyst is a photon absorbing species, such as a transition metal complex (Ciesla *et al.*, 2004, Hennig, 1999), an organic dye (Arques *et al.*, 2007) or an iron salt solution (Andreozzi *et al.*, 2006). In homogeneous photocatalysis the reaction is accelerated through an excited state of the catalyst, which is generated as a result of radiation absorption.

Heterogeneous processes occur in binary phase system (solid-liquid or solid-gas) where a semiconductor is usually used as the photocatalyst. In this case, the absorption of light leads to the formation of active sites on the photocatalyst surface i.e. electron-hole pairs, that interact with the substrate absorbed on its surface (Parmon *et al.*, 2002).

Since the discovery of water photoelectrolysis on a TiO_2 electrode made by Fujishima and Honda (Fujishima and Honda, 1972), heterogeneous photocatalysis has been the object of intensive study. Research on semiconductors as photocatalysts has initially focused on energy conversion and photovoltaic applications (Fujishima *et al.*, 1975). However, it has shifted into environmental application for water treatment and air remediation (Akira Fujishima, 2000).

It has been largely established that the most common water and air pollutants can be oxidised through the breakdown of C-C bonds by photocatalytic oxidation, often achieving complete mineralisation to H_2O and CO_2. Compared with traditional oxidation methods, photocatalysis is more active towards degradation of refractive compounds such as pesticides and oestrogens (Gora *et al.*, 2006).

The photocatalytic process is a red-ox process; thus a reduction reaction always accompanies the oxidation reaction. The photoreduction process has been studied for the removal of heavy metal ions such as Cr(VI), Hg(II), Ag(I), Pb(II), Pd(III) (Litter, 1999). Indeed, one of the advantages of photocatalytic treatment in wastewater treatment is the possibility to treat at the same time organic and inorganic pollutants (Park *et al.*, 2006, Schrank *et al.*, 2002).

The use of suspended catalyst particles in slurry systems is very common, as it allows the maximisation of catalyst surface that is exposed to light irradiation. However, slurries require the separation and recycling of the photocatalyst at the end of the process. The immobilisation of the photocatalyst as thin or thick films on suitable supports like glass, stainless steel or other

metals, solves the problem of catalyst separation and make it possible the application of photocatalytic technologies also for air cleaning.

With a primary focus on TiO_2 as photocatalyst, heterogeneous photocatalysis has been applied in a wide range of environmental issues. As a result of the intense work on fundamental and applied studies on heterogeneous photocatalysis, a range of reviews have been published over the years (Akira Fujishima, 2000, Hoffmann *et al.*, 1995, Linsebigler *et al.*, 1995, Dhananjay S Bhatkhande, 2002, Chatterjee and Dasgupta, 2005, Zhao and Yang, 2003, Malato *et al.*, 2002, Mills and Hunte, 1997).

In the following sections the principles and applications of heterogeneous photocatalysis with particular attention on gas phase systems are reviewed.

2.1.1 Semiconductors as photocatalysts

Photocatalysts used in heterogeneous photocatalysis are usually solid semiconductors due to a combination of properties among which their peculiar electronic structure, light absorption properties and excited state lifetimes.

It is well known that interaction between matter and photons of suitable energy leads to promotion of electrons from the ground state to an excited state. The energy of the photon that can be absorbed depends on the energy difference between ground and excited states. In a single molecule, the ground state and the excited state are respectively the HOMO (Highest Occupied Molecular Orbital) and the LUMO (Lowest Unoccupied Molecular Orbital). The band theory model derives from the extension of molecular orbital theory to a large number of monomeric units i.e. atoms and is generally used to

describe the electronic structure of solids (Fig. 2.1). According to this model the electronic structure in a semiconductor is composed by a valence band (VB) filled with electrons and an empty conductive band (CB) separate by a bandgap Eg, which corresponds to a region of forbidden energies for the electrons. This void region extends from the top of the filled VB to the lowest edge of vacant CB (Linsebigler *et al.*, 1995).

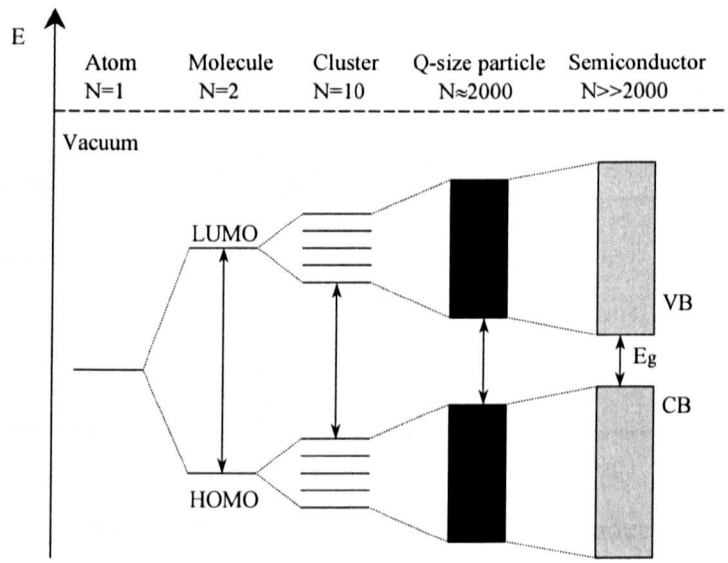

Fig. 2.1. Change in the electronic structure with increase of monomeric units. (Adapted from Hoffmann *et al.*, 1995).

Usually the bandgap is small enough that both thermal or photo excitation can take place leading to the formation of positive holes (h^+) with oxidative properties in the valence band and excited electrons (e^-) with reductive properties in the conductive band. In case of photoexcitation, the absorption of light occurs only if the energy of the photon is equal or higher than the bandgap energy, creating the active sites on the semiconductor surface responsible for the heterogeneous photocatalytic process.

The lifetime of charge carriers created during photoexcitation of semiconductors is sufficient, in time frame of nanoseconds, for the electron-hole pair to undergo photochemical reaction by electron transfer at the catalyst surface (Linsebigler *et al.*, 1995). TiO_2, ZnO, Si, WO_3, CdS, ZnS, Fe_2O_3 are typical semiconductors and Table 2.1 gives their band gap energies (Dhananjay S Bhatkhande, 2002).

Table 2.1. Bandgap energies Eg of various photocatalysts (Dhananjay S Bhatkhande, 2002)

Photocatalyst	Bandgap (eV)	Photocatalyst	Bandgap (eV)
Si	1.1	ZnO	3.2
TiO_2 (rutile)	3.0	*TiO_2 (anatase)*	3.2
WO_3	2.7	CdS	2.4
ZnS	3.7	$SrTiO_3$	3.4
SnO_2	3.5	WSe_2	1.2
Fe_2O_3	2.2	α- Fe_2O_3	3.1

The energy bandgap Eg is typical of every semiconductor and its value is related to the semiconductor absorbance threshold λg by the equation:

$$\lambda g\ (nm) = 1240/Eg\ (eV) \qquad \text{(Eq. 2.2)}$$

The absorption threshold is an important property for practical applications, as it defines the kind of light source needed for photoexcitation. The absorbance edge of wide Eg semiconductors falls in the UV region of the spectra (λ<320 nm), while semiconductors with narrow Eg show a shift of absorbance threshold to longer wavelength and can absorb also in the visible range of the spectrum. An ideal photocatalyst should be able to absorb in the visible range or near UV, in order to efficiently utilise the solar radiation as the source of photons.

The potential of the conductive or valence bands are another important factor for the applicability of a semiconductor in photocatalysis.

In fact, the photo-reduction can occur only if the CB of the semiconductor is more negative than the reduction potential of the oxidant species. Conversely, the photo-oxidation can only occur if the potential of the valence band of the semiconductor is more positive than the oxidation potential of the reductant species.

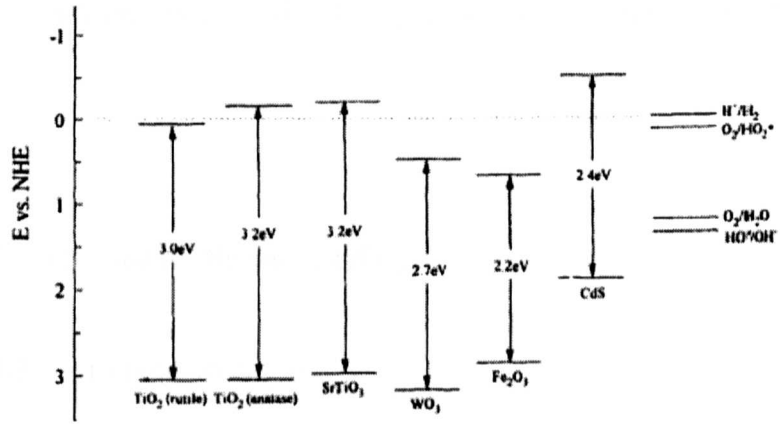

Fig. 2.2. VB and CB positions of various semiconductors, and reduction potentials of relevant redox couples (in liquid phase) at pH=0 (Mills and Hunte, 1997).

These two conditions must be realized at the same time to finalize the photocatalytic process. As shown in Fig 2.2, among various semiconductors the titanium oxide based semiconductors (anatase, rutile and $SrTiO_3$) and CdS satisfy this requirement.

Among various semiconductors, TiO_2 has been proven to be highly active toward a wide range of organic compounds; therefore it is the most commonly used. TiO_2 is a very stable, biologically and chemically inert, non-toxic, photostable, inexpensive and commercially available semiconductor. The main

drawback of TiO_2 is its wide bandgap that limits its application under sunlight. TiO_2 bandgap is Eg=3.0 and 3.2 eV for rutile and anatase respectively, requires UV light for photoexcitation, which represent only around 5% of the solar spectrum (Mills and Hunte, 1997). Other catalysts with narrower bandgap, such as WO_3, can absorb larger portion of the solar radiation, however, WO_3 shows lower photocatalytic activity than TiO_2. ZnO and CdS do not show long term stability in aqueous media, while metal sulfide semiconductors (ZnS or CdS) and iron oxides are subject to photocorrosion during the photocatalytic process.

2.1.2 Titanium Dioxide (TiO_2)

2.1.2.1 Crystal structures

Titanium dioxide exists in three main different crystalline states: anatase, rutile and brookite. Anatase and rutile are the most common crystalline forms and the most studied for photocatalytic applications.

Table 2.2 Some properties of titania polymorphs

Phase	Symmetry	Refractive Index	Density (g/cm^3)
Rutile	Tetragonal	2.76	3.899
Anatase	Tetragonal	2.52	4.250
Brookite	Orthorhombic	-	4.17

The titania crystal unit is composed of Ti^{4+} ion surrounded by six octahedrally coordinated O^{2-} ions. The TiO_6 octahedron in both crystal structures is not regular and shows orthorhombic distortion (Linsebigler *et al.*,

1995). The different crystal structures arise from different arrangements of the octahedral TiO_6 units. As shown in Fig 2.3, chains of edge-sharing octahedral form the rutile crystal, while in anatase the octahedron chains share four corners (Chichina *et al.*, 2005). Due to different spatial arrangement of octahedral chains, the rutile structure is more densely packed than anatase. This fact reflects in the mass densities of the materials: 3.899 g/cm^3 for anatase and 4.250 g/cm^3 for rutile (Navrotsky, A. and O.J. Kleppa, 1967).

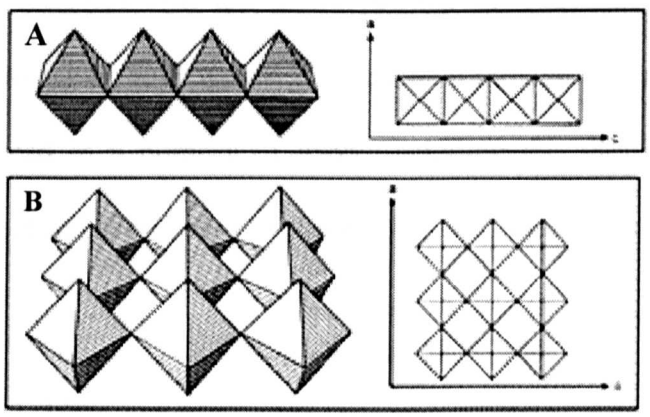

Fig. 2.3. Polyhedral diagrams of rutile (A) and anatase (B) crystal. From (Chichina *et al.*, 2005).

Noticeable property of titania, especially in rutile crystals, is its very high refractive index (Table 2.2). For this reason, titanium dioxide in powder form is widely used as white pigment for providing whiteness and opacity to a variety of materials: e.g. paints and coatings, plastics, paper, inks and cosmetics.

Rutile is the thermodynamically stable form of titania. This is shown by thermochemical data shown in Figure 2.4: the free energy of rutile formation ΔG_f is always lower than the free energy of anatase formation, making rutile the most stable structure at all examined temperatures (Chichina *et al.*, 2005).

Anatase is metastable and reverts spontaneously to rutile at high temperatures (Navrotsky *et al.*, 1967, Shannon *et al.*, 1965). However, different onset temperature and rate of conversion for anatase to rutile transformation depend on several factors such as crystal size and purity of material (Gouma and Mills, 2001).

The generally accepted mechanism for the anatase to rutile phase transformation at high temperatures involves the breakdown of two Ti-O bonds in the anatase structure and the rearrangement of Ti-O octahedra to rutile phase. The breaking of Ti-O bonds is accelerated by lattice disruptions, which can be introduced in a number of ways, including the addition of dopants, variation in the atmosphere (oxygen partial pressure), and method of synthesis.

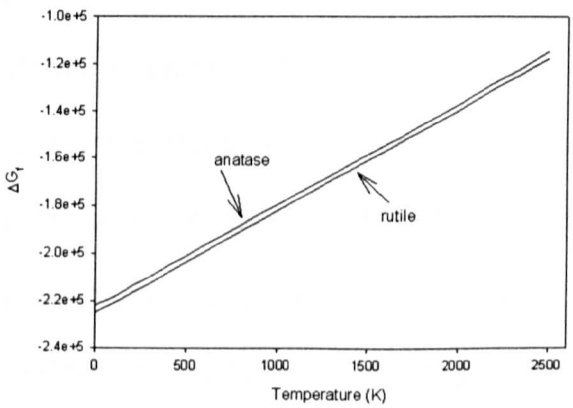

Fig. 2.4. Thermodinamic free energy of rutile and anatase at different temperatures (Chichina *et al.*, 2005).

Brookite is the less common of the three phases. It has an orthorhombic crystal structure and spontaneously transforms to rutile around 750°C (McColm, 1983).

2.1.3 Mechanism of heterogeneous photocatalysis

The overall heterogeneous photocatalytic process can be outlined by the following steps:

(a) migration of the reactants to the catalyst surface

(b) adsorption of reactants on the catalyst surface

(c) reaction of the adsorbed reactants

(d) desorption of reaction intermediates and products

(e) removal of intermediates and product from the interfacial region.

The main difference of photocatalysis with classic heterogeneous catalysis is the initiation of the chemical transformation during step (c), which is photoexcitation in case of photocatalysis instead of thermal activation of classic catalysis.

The photocatalytic reaction in Step (c) is a complex surface process that starts with the absorption of a photon with energy E equal or higher than the energy bandgap Eg of the photocatalyst (i.e. TiO_2). The photon absorption leads to the generation of charge carriers: the photoexcited electron e_{cb}^- and the hole h_{vb}^+ (Eq. 2.3) that is the initiating step of the photocatalytic process.

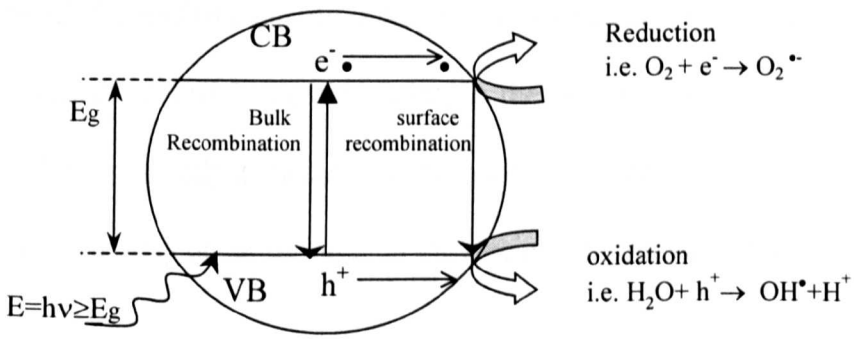

Fig. 2.5. Mechanism scheme of photocatalysis.

$$TiO_2 + h\nu \rightarrow h_{vb}^{+} + e_{cb}^{-} \qquad \text{charge carrier generation} \qquad \text{(Eq. 2.3)}$$

The electron-hole pair can follow different de-excitation pathways (Linsebigler *et al.*, 1995). Charge carriers can undergo bulk recombination, with release of heat in the crystal lattice (Eq 2.4). A fraction of charge carriers migrate at the catalyst surface to get trapped by absorbed species (Eq 2.5a, 2.5b and 2.5c). Typical trapping sites in TiO_2 are adsorbed H_2O, chemisorbed OH groups or surface titanol groups Ti-OH on the catalyst surface (Hoffmann *et al.*, 1995).

$$h_{vb}^{+} + e_{cb} \rightarrow \textit{heat} \qquad \text{bulk recombination} \qquad \text{(Eq. 2.4)}$$

$$h_{vb}^{+} + Ti^{IV}OH \rightarrow Ti^{IV}OH^{\bullet +} \qquad \text{charge carrier trapping} \qquad \text{(Eq. 2.5a)}$$

$$e_{cb}^{-} + Ti^{IV}OH \leftrightarrow Ti^{III}OH \qquad \text{(Eq. 2.5b)}$$

$$e_{cb}^{-} + Ti^{IV} \rightarrow Ti^{III} \qquad \text{(Eq. 2.5c)}$$

The electron trapping might occur via two mechanisms: Eq. 2.5b represents a dynamic equilibrium, which involves the reduction of hydroxylated Ti^{IV}. Reaction in Eq. 2.5c is irreversible and leads to reduction of Ti^{IV} to Ti^{III}. On the other hand, the positive charge is trapped on hydroxilated Ti giving rise to the cation radical $Ti^{IV}OH^{\bullet +}$. At this point, in the presence of suitable scavengers adsorbed on the catalyst surface (electron donor D and electron acceptor A), a redox reaction may occur through an interfacial electron transfer mechanism:

$$Ti^{IV}OH^{\bullet +} + D \rightarrow Ti^{IV}OH + D^{\bullet +} \qquad \text{oxidation} \qquad \text{(Eq. 2.6)}$$

$$e_{tr}^{-} + A \rightarrow Ti^{IV}OH + A^{\bullet -} \qquad \text{reduction} \qquad \text{(Eq. 2.7)}$$

In the absence of such scavengers, electrons and holes recombine in few nanoseconds and dissipate the energy as heat. (D. S. Bhatkhande, 2001)

$$h_{vb}^{+} + Ti^{III}OH \rightarrow Ti^{IV}OH \qquad \text{(Eq. 2.8)}$$

$$e_{cb}^{-} + Ti^{IV}OH^{\bullet+} \leftrightarrow Ti^{IV}OH \qquad \text{(Eq. 2.9)}$$

The excellent activity of TiO_2 can be explained with considerations about redox potential values of excited CB and VB's holes. The oxidation of many organic pollutants requires high potentials. The redox potential of the photogenerated valence band holes in TiO_2 is sufficiently positive to react with the hydroxylated surface to produce $OH^{\bullet}$ radicals, which are the most potent oxidising agents after fluorine. On the other hand the redox potential of the conduction band electrons is sufficiently negative to reduce an electron acceptors such as adsorbed O_2 (Fig 2.2). However, the oxidation process may occur by either indirect oxidation via the surface-bound hydroxyl radical (i.e. a trapped hole at the particle surface) or directly via the valence band hole before it is trapped.

The bulk and surface charge carrier recombination and the oxidation and reduction at the catalyst surface are competitive processes. The balance of this competition defines the overall efficiency of a photocatalyst.

The charge carrier recombination is a very fast process and occurs in nanoseconds, while the timescale necessary for redox processes to take place is 10^{-5} s. It has been estimated that in pure TiO_2 colloids, around 90% of photogenerated charge carriers recombine within 10 ns, therefore are not available for the surface redox processes (Serpone, 1997). One strategy to improve the activity of TiO_2 is to slow down the charge carrier recombination

rate by enhancing e^-/h^+ pair lifetime. Charge separation is often achieved by introducing suitable dopants in the crystal lattice or at the surface of the photocatalyst or by coupling different semiconductors (Section 2.2.5).

2.1.4 Titania properties influencing the photocatalytic activity

The photocatalytic activity of TiO_2 strongly depends on its chemical and physical properties. Many authors have focused their attention on the role of TiO_2 structural parameters such as crystal phase, particle size, surface area, surface hydroxylation etc.... These parameters are reviewed in the following paragraphs. Nowadays it is generally accepted that the differences in the photocatalytic activity of titania cannot be undoubtedly ascribed to only one of the above parameters. Therefore, the general trend is to consider the joined effect of several electronic, textural and structural factors. In this sense, it was recently reported that an efficient TiO_2 photocatalyst should possess simultaneously an appropriate phase structure with textural and electronic properties; the lack of one of these conditions yields to a sharp reduction of its photoactivity (Kolen'ko *et al.*, 2004, Yu *et al.*, 2007).

2.1.4.1 Crystalline phase and composition

It is widely accepted that anatase is the most active TiO_2 polymorph for photooxidation of organic compounds in heterogeneous systems, while rutile is generally considered less active, despite its narrower bandgap (Hurum *et al.*, 2005). Sclafani and Hermann (1996) explained the higher activity of anatase by mean of photoconductance measurements, which is evidenced by two distinct feautures:

(a) anatase is more efficient in the formation of the electron-hole pair than rutile.

(b) anatase has a higher attitude in photoadsorbing O_2 on its surface compared with rutile (Sclafani and Herrmann, 1996).

Moreover, the anatase surface is highly hydroxylated, thus with significant chemisorption properties for O_2 and other species on its surface. On the other hand, rutile is characterised by poor surface hydroxylation possibly due to the high temperatures reached during its preparation (Morterra, 1988, Primet *et al.*, 1971).

However, TiO_2 catalyst made up of mixtures of anatase and rutile often show unexpectedly high photocatalytic activity and sometimes higher than pure anatase (Hoffmann *et al.*, 1995, Kolen'ko *et al.*, 2004). A typical example of this kind of TiO_2 catalyst is the commercial material Degussa P-25, the specifications and structural characteristic of TiO_2 P-25 are reported in section 2.1.4.4.

The first model developed to rationalize the high activity of mixed phases considers anatase as the active component, absorbing the photon and giving rise to e^-/h^+ formation. Electron phase transfer occurs from anatase CB to rutile trapping site, providing an efficient charge separation, hence reducing the recombination rate of the anatase phase (Fig 2.6A).

Hurum and Gray carried out several fundamental studies using electron paramagnetic resonance spectroscopy (EPR) to understand the phenomena responsible for P-25 and other mixed phases TiO_2 improved activity (Hurum *et al.*, 2003, Hurum *et al.*, 2005, Hurum *et al.*, 2006). Their results provide evidences of photogenerated electron transfer from rutile to anatase lattice

trapping sites. The electron is then further transferred from the anatase trapping sites to the surface trapping sites. The whole electron-transfer results in a significant charge separation in the semiconductor system, and allows rutile originating holes to take part in the photocatalytic reactions (Hurum *et al.*, 2003).

The photogenerated electron transfer from rutile to anatase can take place at the interface between anatase and rutile particles only in case of intimate contact between the two phases. This implies good contact between particles with comparable dimension (Hurum *et al*, 2003).

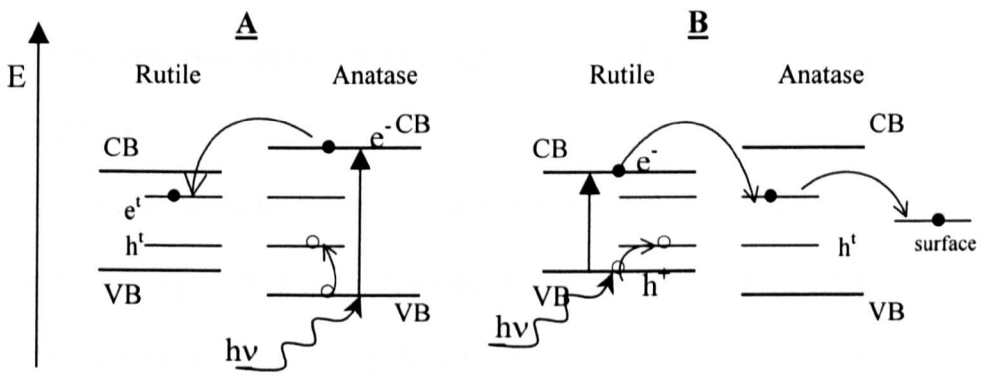

Fig. 2.6. Models of mixed phase TiO_2 activity: A) traditional model where rutile acts as electron sink B) model proposed on the base of EPR results, where electron transfer occurs from rutile to anatase. (Adapted from Hurum *et al*, 2003).

2.1.4.2 Particle size and surface area

Particle size and surface area are properties inversely correlated, as the direct consequence of the growth of titania crystals is the decrease of the surface area. A large surface area is widely considered a desirable property for a photocatalyst. With large surface area the adsorption rate of reactants on the

surface increases; it increases also the number of active sites and consequently the interfacial charge transfer rate at the surface (Zhang *et al.*, 1998).

On the other hand, the particle size influences the electron-hole recombination properties of the material. In fact the dominant electron-hole recombination pathway is different for TiO_2 of different particle sizes. In large crystals, the main pathway is the bulk recombination, while in small crystals the predominant recombination process is the surface recombination. TiO_2 with high crystallinity is characterized by longer charge carrier lifetime associated with a more efficient electron-hole utilization (Ohtani *et al.*, 1997). A linear correlation between photocatalytic activity and anatase crystal size at constant surface area, was found for the degradation of TCE in the gas phase (Jung *et al.*, 2002).

An increase in the photocatalytic activity with increasing the surface area (or decreasing particle size) has been reported (Zhang *et al*, 1998, Maira *et al*, 2000). However, the activity does not increase monotonically and an optimum surface area (or particle size) is usually found. Zhang (1998) found an optimum particle size of 10 nm for the degradation of chloroform in the liquid phase. The authors attribute this phenomenon to the increased surface electron-hole recombination rate that occurs in small particles and offsets the benefits from high surface area (Zhang *et al.*, 1998). In the gas-phase, Maira *et al* (2000) found an optimum TiO_2 crystal size of 7 nm for the photodegradation of TCE. A red shift of the absorption properties in crystals smaller than 11 nm was observed, due to a quantum-size effect. The decreased activity in catalyst smaller than 7 nm was ascribed to a combination of structural and electronic properties (Maira *et al.*, 2000).

The particle size was observed also to affect the activity and the selectivity of products in the photocatalytic oxidation of toluene. TiO_2 with 6 nm crystals were found more active than 20 nm crystals, probably due to higher surface area. Smaller crystals were found to favour the complete mineralisation of toluene, while in larger crystal partial oxidation to benzaldehyde and consequent catalyst deactivation was observed (Maira *et al.*, 2001).

2.1.4.3 Crystallinity

The degree and quality of crystallisation of the semiconductor is generally related to the synthesis procedure and they are considered of crucial importance in photocatalytic studies. In relating the structural and electronic properties of titania samples with their photocatalytic activity, Kolen'ko and co-workers considered the crystalline quality as the main factor governing the 'photo-part' of the photocatalytic process. The 'photo part' includes all phenomena that occur as result of the interaction of matter with light, from the photon absorption to the surface trapping of the charge carriers. In contrast, the surface area is considered to rule the 'catalysis part' that encompasses the surface reactivity of the material.

The photocatalytic activity of amorphous TiO_2 is considered negligible. The inactivity of amorphous TiO_2 has been ascribed to the high recombination rate of photoexcited electron-hole pairs (Ohtani *et al.*, 1997). Amorphous TiO_2 contains many imperfections in the bulk structure, like impurities or microvoids, which are responsible for the presence in the band gap of electronic states that may behave as centers for charge carrier recombination On the other hand, well-developed titania crystals are usually associated with

fewer flaws in the crystal structure, thus fewer recombination centres (Ohtani *et al.*, 1997).

2.1.4.4 Degussa P-25

One of the most widely studied forms of titanium dioxide is the commercial material Degussa P25, which is obtained on industrial scale by high temperature (greater than 1200 °C) flame hydrolysis of $TiCl_4$ in the presence of hydrogen and oxygen, which yields a 99.5% pure product. Degussa P-25 is a mixture of 70% anatase and 30% rutile. It can be classified as non-porous, or with a very low porosity material, with a BET surface area of 55±15 m^2g^{-1} and average crystal size of 30 nm. 90% of the particles fall in the size range 9-38 nm (Mills and Hunte, 1997). TiO_2 crystals do not exist as individual particles forming aggregates of homogeneous appearance, as shown in Fig. 2.7.

Degussa P25 has set the standard for photoreactivity in environmental applications, but recently research is moving towards studies on nanoparticles obtained mainly by sol-gel and hydrothermal methods.

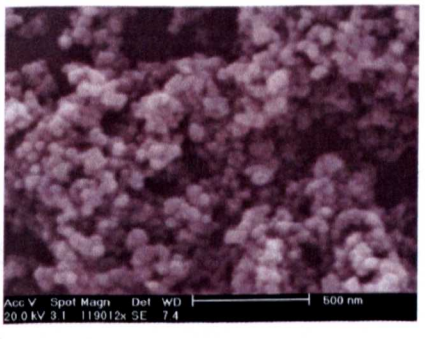

Fig. 2.7. SEM micrograph of Degussa P-25 coated on glass fibre support.

2.2 TiO_2 synthesis: Sol-gel method

2.2.1 Introduction

Sol-gel is known since mid 1800's when Ebelman and Graham during their studies on silica gels observed that the hydrolysis of $Si(OC_2H_5)_4$ under acidic conditions, yielded SiO_2 in the form of a "glass like material" (Hench and West, 1990). However, the potential of the sol-gel method in the preparation of inorganic materials was recognized and developed only during the last decade. Sol-gel process is nowadays a powerful and versatile process for making glasses and ceramic oxides due to its the advantages compared with more conventional synthetic procedures, such as higher purity and homogeneity of the products and milder process temperatures.

Sol-gel process can be defined as a method to convert a colloidal "solution" (sol), to a gelatinous substance (gel) through the growth of inorganic polymers in a solvent. A sol is a colloidal dispersion of particles in the dimension range between 1 nm and 1 micron and a gel is a solid consisting of at least two phases, namely the solvent and the polymeric matrix. The evaporation of the solvent from the gel leaves a material called xerogel.

Sol-gel processing has gained scientific interest and technological importance mainly due to the relative simplicity of the procedure and the almost unlimited possibilities for the formation of materials by tuning the experimental conditions.

The chemistry of sol-gel is based on hydrolysis-condensation reactions. Two approaches of sol-gel process are used differing in the nature of initial precursor (Livage, 1998). The aqueous route is based on the hydrolysis and

condensation of metal salts dissolved in water. In aqueous solution metal ions M^{n+} are coordinated by water molecule (solvatation). The interaction between the metal ion and coordinated solvent increases the acidity of the OH bond in coordinated water. Thus at high pH formation of hydroxyls and oxoanion is possible. At low concentrations ($<10^{-4}$ M) these species exist as monomers, while at higher concentration condensation occurs via nucleophilic attack of OH^- ions onto metal cation. The pH of the solution is a crucial parameter for the condensation process and the determination of final size of aggregate obtained. This process is used for production of silica and alumino-silicate compounds.

The second type of sol-gel route is the so-called alkoxidic route, where a metal-organic precursors i.e. an alkoxide is used as precursor in alcoholic media. Most of the metallic alkoxides can react with water through a series of hydrolysis steps and condensation giving rise to an amorphous solid (Hench and West, 1990). Gelling in this case occurs as a result of polymerization and leads to interconnected 3-D network. The rest of this section will focus only on the alkoxide route since it is the method employed during this study for TiO_2 sol-gel preparation.

2.2.2 Chemistry of sol-gel process

The sol-gel chemistry of silica is one of the most widely studied topics in this area (C.J. Brinker, G.W. Scherer, 1990) and the starting point for application of sol-gel chemistry to other elements such as transition metals like titanium. The sol-gel chemistry of transition metals is more complex than that

of silica because transition metals can exhibit various coordination numbers and show generally higher reactivity due to their lower electronegativity (Livage *et al.*, 1988).

Sol-gel process is based on inorganic polymerisation reactions. It involves the hydrolysis and condensation reactions of metal alkoxide precursors dissolved in organic solvent, usually an alcoholic solution. Common precursors in the case of titania are titanium n-butoxide $Ti(O\text{-}nBu)_4$ and titanium isopropoxide $Ti(O\text{-}iPr)_4$.

The hydrolysis of the precursor leads to formation of monomers with reactive hydroxo groups. The monomers then condense forming bunched oligomers characterized by the presence of hydroxy terminal groups. Further condensation of these polymers leads to a 3D macromolecular network (Hench and West, 1990, B.B. Lakshimi *et al.* 1997; Mansor A.H. and Ismail A.R, 2003;). Eq. 2.10 and 2.11 describe the hydrolysis and condensation steps respectively:

$$Ti(OR)_4 + 4\,H_2O \underset{}{\overset{k_H}{\rightleftharpoons}} Ti(OH)_4 + 4\,ROH \qquad \text{Hydrolysis} \quad (\text{Eq. } 2.10)$$

$$2\,Ti(OH)_4 \overset{k_C}{\rightleftharpoons} {}_3(HO)\text{-}Ti\text{-}O\text{-}Ti\text{-}(OH)_3 + H_2O \qquad \text{Condensation} \quad (\text{Eq. } 2.11)$$

In metal alkoxide precursors the Ti-OR bond is polarized and Ti acts as electrophile in the molecule. The hydrolysis reaction is a bimolecular nucleophilic substitution (Sn2), where an oxygen lone pair attacks the Ti atom bonding to it and causing the elimination of an alkoxyl group. Studies on the reaction mechanism (Park *et al.*, 2003) show that the hydrolysis reaction of titanium alkoxides occurs through an associative substitution reaction pathway,

with the formation of a pentavalent intermediate that in the case of titanium isopropoxide (TIP) as precursor, can be isolated.

The condensation reaction is a nucleophilic substitution that leads to the formation of Ti-O-Ti bridges with the elimination of a water molecule.

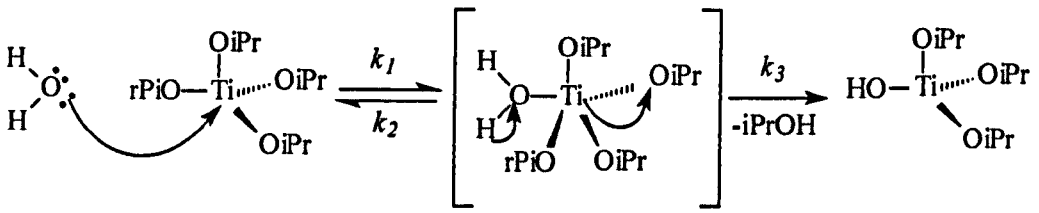

Fig. 2.8. Proposed associative mechanism for hydrolysis reaction. iPr=isopropyl group. (Adapted from Park *et al*, 2003).

However, in normal conditions the hydrolysis and condensation reactions cannot be considered separately. In fact, the condensation process starts before the complete hydrolysis of the precursor: as soon as the formation of hydroxyl groups occurs, the formation of hydroxo bridges between monomers takes place, with formation of olated polymers (Kallala *et al.*, 1993). This is due to the fact that the oxidation state of Ti is lower than its preferred coordination number i.e.: 6.

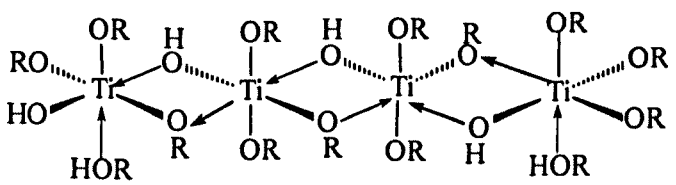

Fig. 2. 9. Formation of olated olygomers.

Therefore the metal tends to increase is coordination number by using its vacant d orbital accepting lone pairs from any nucleophile ligand. The formation of hydroxo bridges allows Ti to fully satisfy its coordination sphere, and this is the driven force of the whole process. The process proceeds through further hydrolysis that substitute residual OR groups with OH groups and through condensation reaction between two hydroxylated Ti centres (Eq. 2.11). Further hydrolysis and polycondensation leads to the formation of a 3D structure.

2.2.3 Synthesis Parameters in Sol-gel

In the classic sol-gel, when the polymers reach macroscopic size a gel is formed. In reality a gel is not the only possible outcome for such hydrolysis-polymerization reaction. Other final product can be obtained depending on reaction conditions. Formation of stable colloidal suspension at microscopic scale can be obtained; or formation of precipitates can be achieved where the reactions produces a very dense structure. Sol and precipitates represent the extreme possibilities; all products in between these two products can be obtained by fine-tuning the synthetic parameters (Kallala *et al.*, 1993).

What determines the nature of the final reaction product is the ratio between the hydrolysis and the condensation reaction rates k_H and k_C (Livage *et al.*, 1988). A good amount of research has been done with the purpose of understanding the kinetics of hydrolysis and condensation reactions and their constants ratio k_H/k_C. Table 2.3 illustrates the commonly accepted rules used to predict the final product of sol-gel system (Livage *et al.*, 1988).

Table 2.3. Expected product of the sol-gel process depending on the hydrolysis and condensation rates.

Hydrolysis rate	Condensation	Result
Slow	Slow	Colloids/sols
Fast	Slow	Polymeric sols/gels
Fast	Fast	Colloidal gel or precipitate
Slow	Fast	Controlled precipitation

In general a colloidal suspension of particles can be obtained if the reaction rate of the condensation step of the process is kept low. Obviously in case of fast condensation reaction the growth of the polymers leads to precipitation or gel formation. The control of hydrolysis and condensation rates might be performed through control of several process parameters, which will be discussed in the following sections.

2.2.3.1 Nature of the Precursor

Three important properties of the metal alkoxide used as precursor have to be taken into account:

(a) The reactivity towards hydrolysis-condensation reactions

(b) The steric hindrance around the metal centre

(c) The molecular structure of metal alkoxydes in the pure liquid state.

It is well known that the reactivity of metal alkoxides decreases with increasing the length of the alkyl group. For example the following order is observed: ethoxide>propoxide>butoxide (Sanchez *et al.*, 1988). This is a consequence of the alkyl inductive effect of the alkylic chains on the metal, which reduces the electrophylicity of the metal. The second property to be considered is the steric hindrance. It affects the hydrolysis rate by modifying

the facility of nucleophilic attack to the metal centre. Reaction rates increase with the following order: primary >secondary> tertiary (Hawes and Trippett, 1968). Finally, the molecular structure of the alkoxide is another important parameter. In fact, due to the coordination expansion tendency of Ti, some Ti alkoxides are oligomers rather than monomers in the pure liquid state. Formation of alkoxy bridging between the monomers or with the coordination of another donor ligand from the solution occurs. Of course, the molecular structure is correlated with steric effect of the alkyl group. As a general rule Ti alkoxides with primary alkoxyl groups easily allows the coordination expansion, forming trimers where the metal centre is surrounded by five ligands. In case of secondary or tertiary alkoxyl groups the monomeric form with Ti in its fourfold coordination is favourite (Livage *et al.*, 1988). Manzini *et al.* shown that $Ti(Oi\text{-}Pr)_4$ is a tetracoordinated monomer in pure liquid state, while $Ti(OBu)_4$ and $Ti(OEt)_4$ form a pentacoordinated oligomer with Ti-Ti distance of 11.09 and 13.09 Å. respectively (Manzini *et al.*, 1995, Kallala *et al.*, 1993).

2.2.3.2 Concentration of water

The molar ratio of water to titanium precursor $r_w=[H_2O]/[Ti]$ has a significant effect on the size and morphology of the obtained sol because it influences the equilibrium of both hydrolysis and condensation reactions (See Eq. 2.10 and 2.11). The complete hydrolysis of Ti alkoxide requires four molecules of water (Eq. 2.10) and the condensation reaction produces one molecule of water for every bridge Ti-O-Ti formed (Eq. 2.11). However, the condensation rate in absence of catalysts or inhibitors depends on the

hydrolysis reaction, which can be considered the drawing force of all the process. When the molar rate is lower or equal to the stoechiometric, i.e.: $r_w \leq 4$, colloidal particles are usually obtained, due to the slow hydrolysis reaction. In excess of water, i.e.: $r_w > 4$, the formation of precipitates is expected because, as a general trend, the hydrolysis rate increases and with it the condensation rate (Hamid and Rahman, 2003).

In a recent study (Maira *et al.*, 2000) is reported how the concentration of water affects the dimension of amorphous TiO_2 aggregates. The concentration of water was varied from 0.25 and 2.5 M, keeping the ratio $[H_2O]/[Ti]$ at fixed value of 4. SEM images show clearly that increasing the concentration of water from 0.25 to 0.5 the particle size decrease rapidly from 900 nm to 100 nm. For concentrations of water higher than 0.5 M a constant value was reached and particle size smaller than 80 nm couldn't be obtained.

2.2.4 pH of solution

The hydrolysis reaction rate increases if carried out under either acid or basic conditions. Under acidic conditions the oxygen atom of the alkoxil group attracts the H^+ ion. Due to this interaction, the Ti electrophilic property increases favoring the nucleophilic attack from a water molecule. Conversely under basic conditions, the OH^- ion, which is a stronger nucleophile than water, attacks the metal centre initiating the hydrolysis reaction.

The H^+ ions act also as inhibitor for the condensation reaction. In fact, depending on the pH, the Ti-OH groups formed through the hydrolysis can be protonated or deprotonated. If the TiOH attacking another Ti is protonated

during its approach to the metal centre the condensation reaction does not occur (Kallala *et al.*, 1993). H^+ prevents the particle growth and agglomeration through electrostatic repulsion. Since the isoelectric point (IEP) of TiO_2 lies at pH 6-6.5 at pH<IEP the surface of the particles is positively charged, thus an acidic environment promotes the dispersed state of the particles. Some organic acids such as acetic acid can act as ligands, coordinating the metal center, hence modifying the reaction equilibrium also through steric indrance.

Conversely, at basic pH the condensation rate is improved through deprotonation of TiOH and consequent formation of TiO^- groups, which are strong nucleophiles. Hence, referring to conditions reported in Table 2.3, the addition of acid to the reaction mixture leads to production of stable sols as final products through a decrease in the condensation reaction rate. On the other hand a reaction carried out in basic conditions produces precipitates due to fast condensation reaction rate.

2.2.5 Advantages and applications of sol-gel

The sol-gel method is widely used in a variety of applications: monolith ceramics, porous membranes, powders, nanoparticles and thin coatings. Monolith ceramics are obtained through formation of stable and crack free bulk gel that can be casted and consolidated at the desired shape.

The principal advantages of the sol-gel technique are:

- Low cost of equipment necessary
- Low temperatures required for reactions
- High homogeneity and purity of products

- Versatility of method
- Ideal starting point for preparation of coatings and thin films

The possibility of depositing thin films on a variety of porous and non porous supports (metals, glasses, plastics, wood, and ceramics) contributes to the application of coated metal oxides in several fields: from environmental applications with photocatalysis for water and air remediation, to the development of energy storage devices (solar cells, fuel cells and supercapacitors), to self-cleaning surfaces. The coatings can be obtained by spin or dip coating technique and electrodeposition.

However, nanoparticles obtained by the hydrolysis-condensation reaction are mainly amorphous, thus powders or deposited thin films must be treated thermally, usually by calcination at high temperature (higher than 300 °C) to achieve crystallization to active polymorph. During thermal treatments but also during normal solvent evaporation, the formation of cracks on the thin film surface occurs which compromises its mechanical properties and successful application in a variety of applications. It has been reported that the sol-gel process carried out in presence of PEG as surfactant leads to crack-free dip-coated films with different degree of porosity depending on molecular weight of PEG used (Guo *et al.*, 2005). A non-acidic sol-gel system containing titanium isoproxide and acetylacetone in 1-butanol, and Tween 20, a nonionic surfactant, has been recently developed for deposition of crack-free coatings on borosilicate glass (Chen *et al.*, 2008).

2.2.6 Hydrothermal process

2.2.6.1 Introduction

The hydrothermal process identifies a preparation method carried out in a sealed heated solution above ambient temperature and pressure. The term 'hydrothermal' is borrowed from geology and earth science where it refers to high temperatures and water pressures processes that occur during the natural formation of mineral ores. Hydrothermal reactions are crystal growth processes that can be carried out in a wide temperature (100°-1000° C) and pressure (1-1000 atm) ranges. Most of the hydrothermal reactions are conducted below the supercritical temperature of water (374°C) and do not exceed pressure of few atmospheres (Shigeyuki and Rustum, 2000).

The term 'solvothermal' is generically used when water or any other solvent (i.e. organic solvents such as alcohols) are used, while 'hydrothermal' refers specifically to those processes conducted in water as reaction media. At laboratory scale, the reactions are carried out in specific autoclaves or digestion bombs. The whole apparatus is composed of an inner vessel, made of inert and corrosion resistant material like Teflon that contains the reaction mixture. The inner container is placed inside a sealable stainless steel cylinder capable of holding the high internal pressures reached during the reaction.

The hydrothermal method is traditionally used for the preparation of synthetic quartz or precious gems in single crystal form. Hydrothermal reactions have been also successfully employed for the preparation of a variety of metal oxides such as ZnO crystals and nanopowders (Cai *et al.*, 2008), CdS nanoparticles (Zhang *et al.*, 2007, Han *et al.*, 2007), WO_3 (Balázsi and Pfeifer,

2002, Kominami *et al.*, 2003) and TiO_2 nanostructures (Hidalgo *et al.*, 2007, Kolen'ko *et al.*, 2003, Kolen'ko *et al.*, 2004, Kominami *et al.*, 2003, Shigeyuki and Rustum, 2000, Yanagisawa and Ovenstone, 1999, Yu *et al.*, 2005, Yu *et al.*, 2007).

2.2.6.2 Effect of Precursor

One of the most used precursors in the hydrothermal synthesis of TiO_2 nanoparticles is amorphous TiO_2 in the form of sol, gel or powders (Ito *et al.*, 2000, Wang and Ying, 1999, Maira *et al.*, 2000, Yanagisawa and Ovenstone, 1999, Yu *et al.*, 2007). The role of the preparation route for the amorphous precursor has been studied.

Hidalgo *et al* (2007) reported the hydrothermal treatment of TiO_2 gels obtained by precipitation of Ti^{4+} from TIP in different acidic solutions (nitric, hydrochloric and acetic acids) as well as using triethylamine (TEA) at different pH. Surface and morphological qualities significantly differ depending on the sol-gel synthetic route. In a similar way, Yanagisawa and Ovenstone used precursors obtained by precipitation of $TiCl_4$ in water, acidic and basic conditions, as well as hydrolysis of $Ti(OC_2H_5)_4$ in dry ethanol (Yanagisawa and Ovenstone, 1999).

Yu and colleagues used colloidal solution obtained from tetrabutylorthotitanate precursor ($TiO(C_4H_9)_4$, TBOT) in water. Hydrothermal treatment at $100<T<200$ °C produced catalysts characterized by an interesting bimodal porosity distribution in the meso and macroporous region, and highly active towards photoxidation of acetone in the liquid phase. The best sample

showed an apparent rate constant that exceed that of P-25 by a factor of over 3 times (Yu *et al.*, 2007).

Also commercial Degussa P-25 has been treated hydrothermically in water suspension. Hydrothermal treatment of P-25 at 150 °C for different length of time (1-72 hours) promoted a significant increase in the porosity and surface hydroxylation of the powders, yielding to TiO_2 catalyst with improved activity for mineralisation of acetone in the liquid phase (Yu *et al.*, 2006).

$TiOSO_4$ is another common Ti precursor used in hydrothermal synthesis. (Kolen'ko *et al.*, 2004, Hidalgo *et al.*, 2007, Kolen'ko *et al.*, 2003, Ran *et al.*, 2007). When $TiOSO_4$ was reacted with urea, only formation of anatase was observed (Ran *et al.*, 2007). $TiOSO_4$ aqueous solution acidified with H_2SO_4 yielded to anatase-rutile mixtures with 15% rutile (Kolen'ko *et al.*, 2003). Kolen'ko also compared the use of $TiOSO_4$ and H_2SO_4, $H_2TiO(C_2O_4)_2$ and $TiO(NO_3)_2$ solutions as precursors on either structural and photocatalytic properties of obtained TiO_2 emphasizing the correlation between salt precursor and phase composition and structural properties.

2.2.6.3 Effect of Temperature and holding time

Increasing both reaction temperature and holding time result in the increase of crystallinity and crystal size of TiO_2 samples. Conversely a decrease in the surface area was observed, most probably as a direct consequence of crystal growth (Ran *et al.*, 2007). Both tendencies have been observed until a maximum temperature, after which the crystal size and the surface area reach a constant value. This trend suggests that the mechanisms of crystal formation and crystal growth may be temperature dependant. Yanagisawa and Ovenstone

proposed a model for the hydrothermal crystallisation of TiO_2 from amorphous precursor where the crystallisation proceeds through a solid-state epitaxial growth at low temperatures and changes to dissolution-precipitation at temperatures higher than 250 °C (Yanagisawa and Ovenstone, 1999).

2.2.6.4 Effect of reaction media

Reaction media properties such as viscosity and dielectric constant can heavily influence the mobility, reactivity and solubility of species in solution. Thus, the composition of the solution media influences the product nature and characteristics.

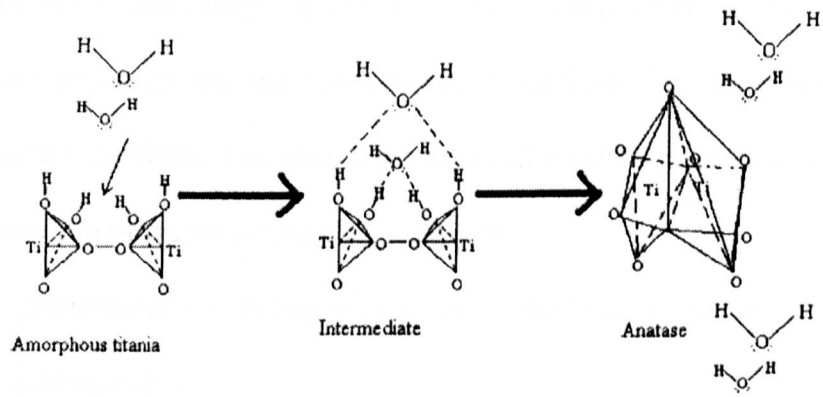

Fig. 2.10. Proposed model for hydrothermal conversion of amorphous titania to anatase. (From Yanagisawa and Ovenstone, 1999).

Water has proven to have a positive effect on the anatase crystallization from amorphous sols and powders, by coordinating the amorphous titania surface and catalyzing the rearrangement of TiO_6 octahedra and the nucleation step in the phase transition (Yanagisawa and Ovenstone, 1999).

By using mixture of water and alcohols it is possible to control the degree of crystallization of obtained powders. It has also been observed that increasing

the ratio alcohol-water, the expected decrease in particle size is accompanied by an increase in surface area and porosity that occur systematically at different combinations of reaction temperatures and holding times (Wang and Ying, 1999).

2.2.6.5 Advantages of hydrothermal method

The TiO_2 nanomaterials obtained by hydrothermal treatment are characterized by high surface area compared with similar materials prepared by other methods such as sol-gel followed by calcination. In addition, the hydrothermal process has proven to be very versatile as it is possible to tune and control the size, shape and type of titania polymorph by using different precursors and changing the hydrothermal conditions. For these reasons, the hydrothermal synthesis has been used as an alternative process to sol-gel for the preparation of highly active photocatalysts.

The preparation of nanoparticles by hydrothermal process offers the following advantages:

- Mild temperature conditions – crystallisation of TiO_2 requires temperatures much lower than those required by calcination treatment.
- High purity of the product
- High reproducibility
- It is a green technique: being carried out in a closed environment the pollution and waste are minimised.

However, some limitations for the application of hydrothermal methods on a large scale arise from the safety issues related to the utilisation of high pressures.

2.2.7 Modified TiO_2 photocatalysts

2.2.7.1 Introduction

The widespread use of titania as photocatalyst in industrial remediation technologies and commercial systems is prevented by its low efficiency under natural illumination. Indeed, the main flaw of TiO_2 as photocatalyst is its wide bandgap energy, 3.0 and 3.2 eV for rutile and anatase respectively, which require absorption of UV radiation at wavelength <386-400 nm for photoexcitation. This means that only 5-10% of solar spectra can be utilised limiting its applicability under solar or visible light illumination.

Moreover, as already stated, the recombination is a predominant process on TiO_2, and by the time the photocatalytic reaction can take place, only around 10% of the photogenerated charge carriers are available at the catalyst surface.

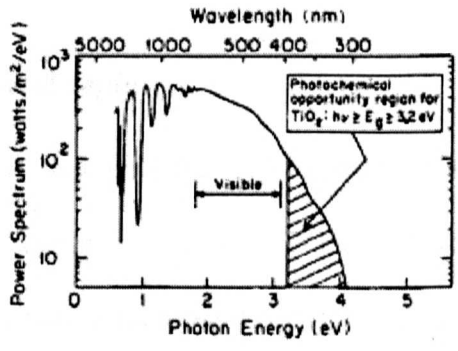

Fig. 2.11 Fraction of the solar spectra utilisable for the photoexcitation of TiO_2. (From Linsebigler *et al.* 1995).

The scientific community's efforts towards the optimisation of the performance of TiO_2 have focused in two directions: (a) the alteration of TiO_2 electronic and surface properties to allow a shift of the absorption onset towards visible wavelength; (b) the maximisation of the utilisation of

photogenerated charge carriers through the reduction of the charge carrier recombination rate.

The utilisation of various dopant species has been widely investigated, as well as the introduction of surface modifications such as metal deposition and development of composite semiconductors. According to Asahi *et al*, an ideal dopant should satisfy three general conditions (Asahi *et al.*, 2001):

(a) It should produce states in the TiO_2 bandgap that absorb radiations in the visible range of the spectra ($\lambda \geq 400$ nm);

(b) The conduction band minimum (CBM) of the doped TiO_2 should be higher than the redox couple involved in the photoreductive process

(c) The dopant states should overlap adequately with the band states of TiO_2, in order to allow transfer of the photoexcited carriers to the reactive sites at the catalyst surface within their lifetime.

2.2.7.2 Metal doping

The first doping attempts that can be found in the literature used transition and noble metals as dopant agents, on Degussa P-25 first, and on TiO_2 obtained by sol-gel or alternative methods later (Chatterjee and Dasgupta, 2005, Anpo and Takeuchi, 2003). Metal ions from the transition series such as V, Cr, Mn, Fe, Cu, Ag, Au, Pd as well as rare earth metals (Parida and Sahu, 2008) were inserted in the crystal lattice of titania, substituting the Ti ions. Referring to the aforementioned Asahi's conditions, metals may contribute with their d orbitals and corresponding energy states, to shifting the absorption edge towards the visible range. However, the d states can also act as recombination charge centres and have a detrimental effect on the photocatalytic efficiency under

UV-visible light. For this reason, to date contrasting results have been reported, depending on the nature of metal ion and the preparation method.

The metal-ion doping can be achieved by physical or chemical methods. In the physical ion implantation, bare titania is bombarded with high-energy metal ion beam (Yamashita *et al.*, 2002, Anpo and Takeuchi, 2003). It was discovered that metal-ion implantation with V, Cr, Mn, Fe, and Ni caused a consistent shift toward the visible light region with the following order: V > Cr > Mn > Fe > Ni. This shift allows the utilization of approximately 20–30% of solar spectra of the titanium oxide catalysts and its extent was found to be function of the dopant concentration (Anpo and Takeuchi, 2003).

Yamashita reported the mineralization of 2-propanol in water under visible light by V^+ doped TiO_2 obtained by physical ion implantation as result of light absorption improvement (Yamashita *et al.*, 2002). It was also found that the activity under UV irradiation of the doped catalyst was comparable with that of the pristine catalyst, suggesting that the implanted metal ions do not act as recombination centre (Yamashita *et al.*, 2002).

Among chemical doping methods, the sol-gel and the chemical implantation are often used (Araña *et al.*, 2004, Anpo and Takeuchi, 2003). In the sol-gel approach the doping occurs during the hydrolysis-condensation step when a suitable metal precursor (usually a salt) is added to the reactant solution. On the other hand, the implantation is carried out by mixing the amorphous or crystalline titania with a metal salt solution followed by evaporation of the solvent. The degree of doping achievable with chemical methods is obviously lower than with physical implantation. As a consequence, the absorption shift obtained by chemical methods is much less efficient than with implantation

method (Anpo and Takeuchi, 2003). Metal doping has some drawbacks such as thermal instability that limit the possibility of real application of these catalysts ({Dhananjay, 2002}.

2.2.7.3 Anion doping

The use of non-metal doping (predominantly N, C, and S) has been used to shift the photoresponse of TiO_2, giving rise to the so-called "second generation" titania catalysts.

Asahi and co-workers (2001) were the first researchers to report a visible light active anion-doped TiO_2 photocatalyst (Asahi *et al.*, 2001). A high temperature nitridation process under reductive conditions was used to prepare $TiO_{2-x}N_x$ catalyst where N was substituting O in the crystal lattice. This $TiO_{2-x}N_x$ catalyst shows a red-shift of the adsorption edge. The shift was justified in terms of TiO_2 band-gap narrowing due to the mixing of N_{2p} and O_{2p} states. N-doped TiO_2 showed an increased photo-activity for the decomposition of methylene blue and acetaldehyde under visible light.

Several alternative ways to the high temperature nitridation synthesis used by Asashi have been proposed. These syntheses are mainly based on the sol-gel process and have recently been reviewed (Qiu and Burda, 2007). Burda *et al* (2003) developed a synthesis based on the sol-gel method, which leads to a doping concentration up to 8% molar. In this method $TiO_{2-x}N_x$ samples were prepared via direct nitridation by tetraethylamine (TEA) of TiO_2 nanoparticles colloid obtained after the hydrolysis at controlled pH of titanium isopropoxide (TIP) in water. Visible light activation of the catalyst and photocatalytic degradation of methylene blue in the liquid phase was proved.

A hydrothermal synthesis for the preparation of N-doped TiO_2 was recently proposed by Rhee *et al* (2005). In this method titanium oxysulfate ($TiOSO_4$) and ammonia solution react hydrothermically at 120 °C for 3 days. For the reaction a constant reagents ratio of $TiOSO_4/H_2O/NH_4OH$=1/15/50 was used. The product of the hydrothermal process was identified as the compound $(NH_4)_2Ti_3O_{7-x}N_x$ and then converted to $TiO_{2-x}N_x$ by calcination. $TiO_{2-x}N_x$ showed improved activity compared with non-doped nanoparticles for visible light photodegradation of 2-propanol (Rhee *et al.*, 2005). Visible light activation has been claimed also for C and S-doped systems and mixed anionic doping (Zhou and Yu, 2008, Yu *et al.*, Ren *et al.*, 2007).

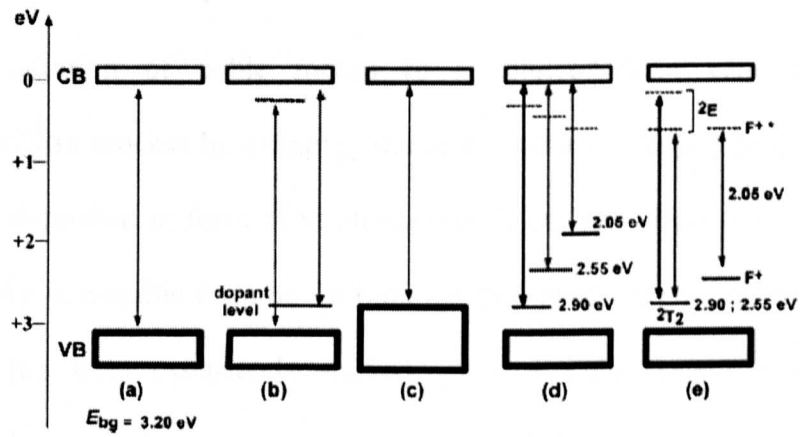

Fig. 2. 12. Diagram of possible doping effects on red-shift adsorption proposed by Serpone (Serpone, 2006): (a) Band gap of bare TiO_2; (b) doped TiO_2 with localized dopant levels near the VB and the CB; (c) band gap narrowing resulting from broadening of the VB; (d) localized dopant levels and electronic transitions to the CB; and (e) electronic transitions from localized levels near the VB to their corresponding excited states for Ti^{3+} and F^+ centers.

The actual reason for the red-shift in anion-doped TiO_2 is still a matter of debate. Some studies have proposed a narrowing of the bandgap due to the

formation of a N_{2p} and O_{2p} mixing state, while other authors proposed the existence in the bandgap of localised energy states deriving from dopant presence. In this respect, in 2006 Serpone summarised and discussed the various options, claiming that the bandgap narrowing in semiconductor requires a heavy doping level that would compromise the nature of the semiconductor. It was proposed that the absorption in the visible range is related with the formation of defects due to formation of oxygen vacancies resulting from anion (or other) lattice doping. These defects give rise to colour centres responsible for the absorption band at lower energies (longer wavelength) (Serpone, 2006).

2.2.7.4 Metal deposition

The addition of noble metals to a semiconductor can change the photocatalytic process by changing the semiconductor surface properties. The metal is deposited in form of small nanoparticles. The effect of deposition of Pt, Au, Ag in metallic form on TiO_2 on reaction products and selectivity of the process has been extensively studied. The Pt/TiO_2 system is the metal-semiconductor system most commonly studied. For some reactions such as evolution of H_2 from ethanol reduction and water splitting, the metal is important also because of its own catalytic activity. In the case of photocatalytic oxidations, the effect of the platinisation is highly dependant on the substrate to be degraded and on the loading of deposited Pt. To date, the role of Pt is not fully understood, and the effect of platinisation on TiO_2 photocatalysis is still the object of intense research. However, In general, it is accepted that in Pt/TiO_2 systems a better separation of charge carriers occurs.

2.2.7.5 Coupled semiconductors

Another interesting approach to modify the surface properties of TiO_2 consists in coupling TiO_2 with a narrower band-gap semiconductor (e.g. CdS or WO_3). For example, CdS is capable of receiving excitation in the visible region of the solar spectrum (Eg=2.4 eV), but it cannot be used efficiently as photocatalyst due to its instability. By coupling narrow band-gap semiconductors (i.e.: CdS or WO_3) with TiO_2 the photoexcitation process can be modifyied as shown in Fig 2.13 where SC is a narrow band gap semiconductor.

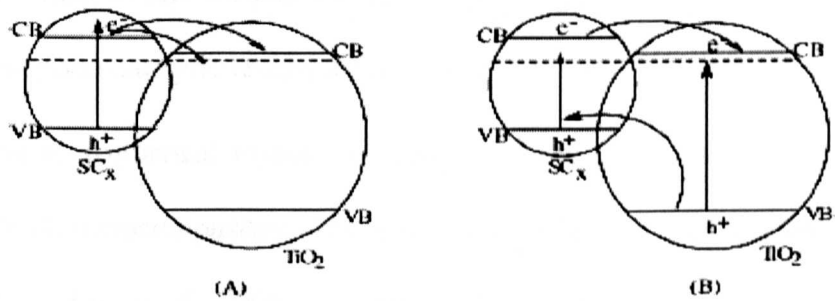

Fig. 2.13. Doping mechanism scheme in heterojunction between semiconductors (Chatterjee and Dasgupta, 2005).

Photoexcitation occurs on SC, for absorption of visible range wavelengths. If SC's conduction band overlaps efficiently with that of TiO_2, excited electrons can be transferred from SC to TiO_2 (Fig. 2.13A). Fig 2.13B shows the transfer of electrons as well as holes between the two semiconductors.

This visible light induced interparticle electron transfer (IPET) was discovered and demonstrated the improvement of decomposition of H_2S into hydrogen and sulfur by coupling TiO_2 and CdS. The coupling of two different

types of semiconductors has been reported to be beneficial also in the photo-oxidation processes. The IPET pathway can take place from narrow band-gap semiconductor to TiO_2 enhancing the charge separation in the coupled system (Serpone *et al.*, 1995).

Because the two semiconductors' energy state must overlap to allow the charge transfer and the consequent charge separation, the nature and quality of the heterojunction between the two semiconductors surfaces is very important.

2.2.7.6 TiO_2/WO_3 nanocomposites

During this research work some TiO_2/WO_3 systems have been prepared and studied, thus in this section the most common preparation methods and some relevant photocatalytic results are reviewed.

Several synthetical routes are reported in literature for the preparation of TiO_2/WO_3 nanocomposites, which are based either on impregnation (Keller *et al.*, 2003, Zuo *et al.*, 2006), sol-precipitation (Yang *et al.*, 2002, Yang *et al.*, 2005) or sol-gel (Yang *et al.*, 2005).

In the impregnation methods, an aqueous solution of WO_3 precursor is left reacting under stirring in a TiO_2 suspension. Ammonium paratungstate $(NH_4)_{10}H_2(W_2O_7)_6$ is often used as WO_3 precursor. After evaporation of the solvent until dryness, the resulting powder is calcined in air. The initial addition of different amount of tungsten precursor, leads to nanocomposites that differ in WO_3 content.

In a sol-precipitation method proposed by Yang in 2002 ammonia hydroxide is dropped in a solution of $TiCl_4$ and WO_6, precursor of TiO_2 and WO_3 respectively, and using PEG as surfactant. The powders were then

calcined between 400 and 900 °C for 2 h leading to samples with different morphologies and textural properties. In the sol-gel method proposed by Yang in 2005, $TiOBu_4$ is used as Ti precursor while ammonium tungstate as W precursor. The reaction is simply a hydrolysis-condensation carried out in ethanol at pH=10. The obtained sol was aged for 12 h, and the powders were calcined at 400 °C.

A simple physical mixing by ball milling (Shifu *et al.*, 2005) and a microemulsion approach (Fuerte *et al.*, 2002) were also employed. Recently a surfactant-assisted hydrothermal synthesis, followed by calcination, has been developed using $Ti(SO_4)_2$ and Na_2WO_4 as oxides precursors respectively and CTAB (cetyltrimethylammonium bromide) as surfactant (Ke *et al.*, 2008).

The effect of WO_3 on the photocatalytic properties of TiO_2 was reported for the first time by Do in 1993 for the photo-oxidation of 1,4-dichlorobenzene (DCB) in the liquid phase. DCB decomposition was improved using TiO_2/WO_3 system and an optimum WO_3 loading of 3% molar was found. Photoexcited electron-trapping by WO_3 with formation of W(V) was proposed to explain the improved activity (Do *et al.*, 1993).

In the vapor phase, the addition of WO_3 to TiO_2 yield enhanced reaction rates also in the photooxidation of butyl acetate (Keller *et al.*, 2003), benzene and 2-propanol (Kwon *et al.*, 2000) and toluene (Fuerte *et al.*, 2002). Nanocomposites from 1 to 10% wt WO_3 showed higher activity towards butyl acetate oxidation in vapour phase, compared with TiO_2 alone. The optimum WO_3 content was established to be 4% wt (Keller *et al.*, 2003). These studies focused also in the determination of the WO_3 loading effect on photocatalytic behavior of composite systems. A loading of around 3% mol, which is

approximately equivalent to the formation of a WO_3 monolayer, has been found as optimum value.

The IPET pathway that produces an efficient charge separation within the coupled semiconductor system is one of the phenomena that contribute to the improved photocatalytic behaviour of TiO_2/WO_3 composites. However, WO_3 exhibits a higher acidity than TiO_2 and its presence in the nanocomposite can modify the affinity of substrates for the catalyst surface, and consequently, the adsorption equilibrium and photo-oxidation activity of the catalyst. Evidences of higher adsorption affinity of WO_3/TiO_2 composites due to the higher Lewis acidity of the mixed systems have been reported (Kwon *et al.*, 2000). Song *et al* also reported an increase in the Lewis surface acidity of Degussa P-25 when WO_3 was deposited on its surface. The acidity increased with increasing WO_3 content up to 3% molar (Song *et al.*, 2001).

2.2.8 Photocatalytic reactors for studies in the gas phase

An efficient and cost effective photocatalytic reactor for indoor air remediation should achieve good conversion rates and be capable of work with high air feeding. Thus, high volume and low- pressure drop designs that guarantee an effective contact between photons, solid catalyst and gaseous reactants in the system are required (Zhao and Yang, 2003). Several reactor configurations have been designed and modeled to study the kinetic of photocatalytic oxidations as function of operative parameters such as humidity, pollutant concentration, flow rate and light intensity. Photocatalytic reactors can be classified on the basis of their geometry i.e. tubular, flat plate or catalyst disposition i.e. fixed bed, fluidized bed or slurries.

In fluidised bed reactors the inlet flows directly through the catalyst and satisfies the above criteria. TCE photodegradation was first studied using a flat-plate fluidised bed photoreactor reported in Fig 2.14 (Dibble and Raupp, 1992, Dibble and Raupp, 1990). Due to poor fluidising properties of pure titania, TiO_2 was supported on silica. This configuration provided the achievement of high TCE conversions for low pollutant loadings (<10 ppm) for long period of time. The degradation rates in the gas phase were higher than those reported for TCE photodegradation in the liquid phase obtained in a similar photocatalytic reactor (Dibble and Raupp, 1992).

Lim and Kin (2004) used a fluidised bed reactor with annular geometry where the UV lamp is located at the centre of the reactor, to evaluate the TCE photodegradation, obtaining similar results with Dipple and Raupp (Lim and Kim, 2004). Anderson and colleagues designed a pack bed reactor containing TiO_2 pellets 0,3-1,6 mm in diameter obtaining a 99,3% conversion efficiency for single pass experiments.

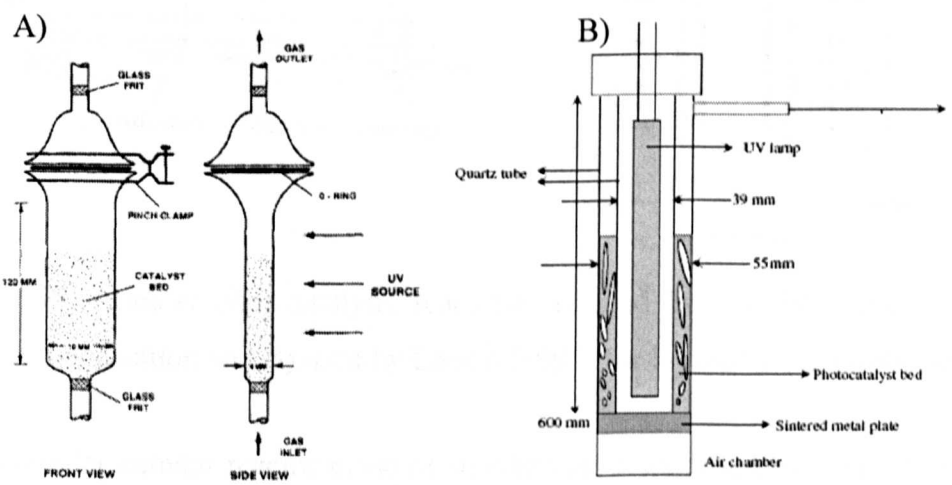

Fig. 2. 14. Fluidised-bed photoreactors: A) Front and side views of flat-plate photoreactor (Dibble and Raupp, 1992) and B) Annulus fluidised photoreactor (Lim and Kim, 2004), used for TCE photooxidation in the gas phase.

In fixed bed reactors, the catalyst is immobilised as thin or thick film on the surface of the reactor. Fix-bed reactors are usually considered easier to operate than slurry, fluidised and packed bed reactors. Larson *et al* (Larson *et al.*, 1995) studied the photocatalytic degradation of 2-propanol at ambient temperature using a thin film annular reactor reported in Fig 2.15B. The catalyst (Degussa P-25) was immobilised on the wall of the cylindrical region and six UV lamps evenly positioned around the reactor provided the illumination.

An annular geometry with a different configuration was recently studied and optimised for formaldehyde degradation in the gas phase (Shiraishi *et al.*, 2005). In this case the illumination is provided by one UV lamp positioned coaxial with the reactor and the catalyst was sol-gel obtained anatase immobilised on the internal glass tube wall forming a transparent thin film.

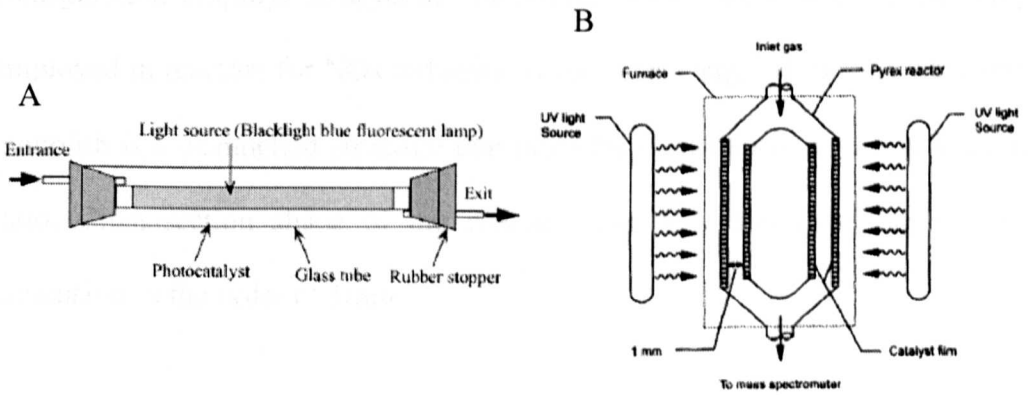

Fig. 2.15. Annular photocatalytic reactors: A) used by Shiraishi (2005) for TCE mineralisation and B) used by Larson (1995) for 2-propanol degradation.

A similar annular reactor made of stainless steel was used by Bouzaza and colleagues in the mineralisation of TCE, toluene, iso-propanol and butane by using Degussa P-25 as catalyst (Bouzaza *et al.*, 2006).

Among fix-bed reactors, the flat-plate configuration is another very common geometry (Keshmiri *et al.*, 2006, Maira *et al.*, 2000, Maira *et al.*, 2001, Demeestere *et al.*, 2004). This configuration has been extensively used for kinetic studies, as differential conditions can be easily achieved and the system shows good stability and reproducibility. All the photocatalyst prepared and studied in the frame of the present research have been evaluated in a flat-plate photocatalytic reactor similar with that reported in Fig. 2.16.

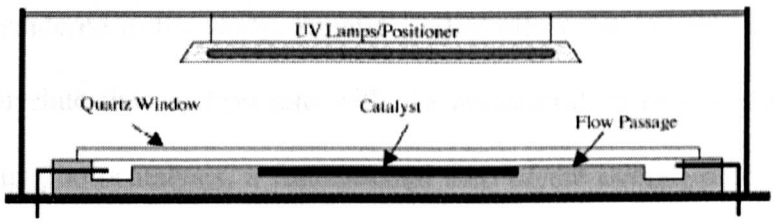

Fig. 2.16. Flat-plate reactor scheme. (From Keshmiri *et al*, 2006).

In the frame of scaling up and design of commercial systems a successful configuration employs honeycomb monoliths, which have been successfully employed in reactors for NOx reduction (Zhao and Yang, 2003). A honeycomb monolith is a channelled structure that provides a high surface area to volume ratio. Cross-section shape of the channels can vary and have the internal dimension in the order of 1mm.

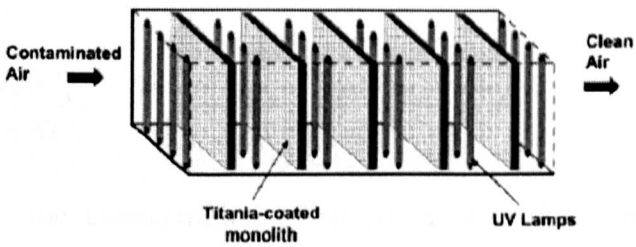

Fig. 2.17. Honeycomb monolith photocatalytic reactor for indoor air purification (Raupp *et al.*, 2001).

In photocatalytic applications honeycomb monoliths are coated with TiO_2 and UV lamps are positioned between the coated monolith as in Fig 2.17. (Sauer and Ollis, 1994), studied the photocatalytic oxidation of acetone using a ceramic honeycomb monolith reactor.

2.2.9 Reaction rate and Kinetic studies

In research the study of photocatalytic reaction takes place through the determination of the reaction rate i.e. the rate of disappearance of the model pollutant considered in the study. Kinetic studies allow the formulation of rate laws that correlate the reaction rate with the concentration of the reactant. In heterogeneous photocatalysis, a fundamental step of the overall process is the adsorption of reactants on the catalyst surface, thus the rate law must take into account also the sorption isotherms. On the basis of experimental results, kinetic models are developed in order to predict the reaction rates and optimize the experimental conditions. The optimisation of experimental parameters is of crucial importance in the scale-up stage of photocatalytic facilities for practical applications.

The Langmuir-Hinshelwood (L-H) model has been widely used in the rate law formulation. For photooxidation of a generic specie A the L-H equation has the form:

$$-r_A = \frac{kKC_A}{1+KC_A} \qquad \text{(Eq. 2.13)}$$

Where C_A is the concentration of specie A, k is the apparent reaction rate constant relative to reaction of A on the catalyst surface and K is the adsorption-desorption equilibrium constant of the specie A on the catalyst surface. The apparent reaction rate constant k includes the true reaction rate

plus the contribution from the optical properties of the film, the relative humidity and the intermediates (Salvado-Estivill *et al.*, 2007b). The L–H equation is often applied to describe the initial rate of degradation at time equals zero as a function of the initial substrate concentration. The extrapolation of the rate to time equals to zero simplifies the interpretation of data, as it avoids all the possible interference from by-products. Less often the L–H rate equation has been combined with the material and radiation balance equations of the reactor to yield the dynamic or steady-state behaviour of the system (Salvado-Estivill *et al.*, 2007a).

The adsorption constant K can be obtained from the dark adsorption isotherms of the catalyst. However, in many cases the so obtained values of K differ from those obtained from kinetic data in the photocatalytic system (Minero, 1999). The actual interpretation of kinetic constants values has been a matter of debate. Thus, even if the two-parameters L-H model described in Eq. 2.13 offers a good fitting of experimental data, the values of the kinetic constant are to be taken sceptically and not considered of physical significance (Minero, 1999).

2.2.10 Factors affecting the reaction rate

In photocatalytic reaction, the reaction rate depends on several experimental parameters such as reactant concentration, light intensity, relative humidity, and temperature.

2.2.10.1 Light intensity

The relation between light intensity and reaction rate is expressed by the following power law (Terzian and Serpone, 1995):

$$r = k \times I^{\alpha} \quad \text{(Eq. 2.14)}$$

In the linearised equation

$$\text{Log}\, r = \alpha \log I \quad \text{(Eq. 2.15)}$$

The value of α can be estimated by the linear regression of the data. It has been reported that the reaction rate is proportional to light intensity (α=1) at low intensity regime, while it is proportional to square root of light intensity (α=0,5) at high intensity regime. At low light intensity the photon harvesting is efficient and the electron-hole pairs formed are consumed by chemical process, while at high light intensity the recombination of electron hole pairs is considered the dominant process on catalyst surface (Zhao and Yang, 2003).

Obee and Brown studied the correlation between light intensity and reaction rate for photodegradation of formaldehyde, toluene and 1,3-butadiene, finding half order correlation at light intensities above 10-20 W/m^2. In the case of TCE photooxidatition in the gas phase, a first order correlation has been observed up to 17 W/m^2 (Jacoby *et al.*, 1995) and recently up to 28.1 W/m^2 (Salvado-Estivill *et al.*, 2007b).

2.2.10.2 Water vapour concentration

As reported in Fig 2.5, water is involved in the oxidation reaction at the catalyst surface, forming the hydroxyl radicals, thus a certain level of relative humidity in the gas reaction media is considered favourable. In absence of water vapour, the photo-degradation of some substrates such as formaldehyde and toluene is retarded and complete mineralisation is not achieved (Zhao and Yang, 2003). However, high relative humidity leads to an inhibition of the photo-oxidation rate. Water is easily adsorbed on TiO_2 surface, and it

competes with the substrate for the occupation of the catalyst active sites. The adsorption competition depends on the affinity of substrate towards surface adsorption, which increases with increasing its polarity.

In the photodegradation of TCE, different authors reported a decrease of reaction rate with increasing of water content in the reaction mixture (Ou and Lo, 2007); while more recently an optimum water concentration value of 0.4 mol/m^3 was found (Kim *et al*, 2003). Relative humidity of 8% has been reported the optimum value for TCE photo-oxidation in a flat plate single pass photoreactor (Salvado-Estivill *et al.*, 2007b).

2.2.10.3 Temperature

The effect of temperature on photocatalytic reaction in the gas phase has been studied for several substrates. Blake and Griffin, studied the effect of temperature on photoxidation of 1-butanol. It was found that the maximum reaction rate occurred at 107 °C, to fall to lower values at higher temperatures (Blake and Griffin, 1988). Anderson and co-workers (1995) tried to elucidate the role of reaction temperature in the gas phase photocatalytic reactions using ethylene as probe organic compound. The study was carried out at 32 °C and 108 °C showing an increase of ethylene conversion, at steady state conditions, from 40.6% to 70.7%. The significant activity improvement has been related with the water desorption that occurs at the catalyst surface with increasing reaction temperature (Fu *et al.*, 1996).

2.2.10.4 Flow rate

When operating at low flow-rate regimes, the reaction limiting step is the mass transfer of reactants from the bulk phase to the catalyst surface. In

condition of mass transfer control the reaction rate increases with the flow rate. At sufficiently high flow rates the reaction rate is independent from the reactant mass transfer and it is controlled by the surface reaction (kinetic control). In order to minimise the mass transfer influence in the determination of reaction rates and comparison of photocatalytic activities, a photocatalytic reactor should be operated in the kinetic control flow rate regime. The determination of the transition value from mass to kinetic control depends on experimental conditions and reactor geometry. The kinetic regime for photodegradation of TCE, was established at flowrates equal or higher than 300 ml/min for a tubular packed bed reactor (Kuo-Hua Wang *et al.*, 1998). In the flat-plate photoreactor used in this study, the kinetic control was observed at flow-rates higher than 1.72 L/min (Salvado-Estivill *et al.*, 2007b).

2.2.11 Mechanism of TCE degradation

The first studies on TCE photodegradation on TiO_2 in the gas phase showed high rates of reactions with formation of CO_2 and HCl as photo-oxidation products, but no byproducts or intermediates were identified in the reaction effluent. However, by using 'direct sampling' techniques such as molecular beam mass spectrometry and gas-phase Fourier transform infrared (FTIR) several reaction intermediates such as dichloroacetaldehyde (DCAAD), phosgene ($COCl_2$) carbon dioxide (CO_2), carbon monoxide (CO) and molecular chlorine (Cl_2) were identified (Jacoby *et al.*, 1994, Nimlos *et al.*, 1993, Alberici *et al.*, 1998).

It is generally accepted that photocatalytic degradation of TCE over TiO_2 produces DCAC as major by-products, which undergoes further oxidation to

yield $COCl_2$, CO, CO_2 and Cl_2 as final products. Jacoby *et al* estimated that 85% of TCE degrades through DCAC formation and 15% through direct oxidation (Jacoby *et al.*, 1994).

On TiO_2 surface, OH radicals are formed under UV illumination. However, in TCE photo-oxidation, a chlorine propagated radical chain reaction has been confirmed by several studies. In addition, the presence of molecular chlorine in the final reaction products as result of termination step of radical chain, confirms the presence of chlorine radicals during the reaction. The formation of chlorine radical is compatible with the reaction mechanism reported in Fig 2.18.

Hydroxyl radicals (OH·) attacks the TCE molecules to form an alkyl radical (1) which reacts with O_2 to form a peroxyl radical (2). Two peroxyl radicals react with elimination of a O_2 molecula and formation of alkoxy radical (3). The alkoxy radical loses a Cl·.

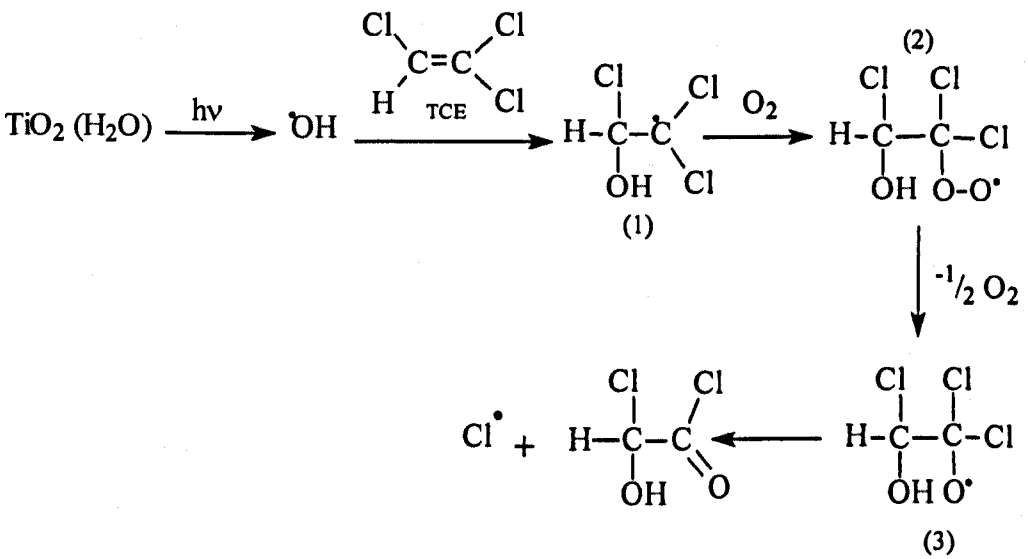

Fig. 2.18. Generation of Chlorine radicals.

Following a similar chain reaction pattern, the Cl· radical attacks a TCE molecule, until formation of the alkoxyl radical. The alkoxyl radical can undergo Cl elimination through the equilibrium pathway (a) or undergo C-C bond cleavage (pathway b) yielding phosgene and ClCH·.The branching ratio for the two competing processes (a) and (b), depends upon the relative strengths of the C–C and the C–Cl bonds of the alkoxy carbon. The DCAC by-product eventually forms phosgene by Cl· (or OH) attack via the reverse reaction (a). TCE degradation is completed by phosgene decomposition to CO, CO_2, Cl_2, and HCl.

The involvement of chlorine radicals in photo-oxidation of chlorinated hydrocarbons is also confirmed by the evidence that isooctane and toluene are degraded much more efficiently in the presence of TCE as source of chlorine atoms (Sauer M.L. *et al.*, 1995).

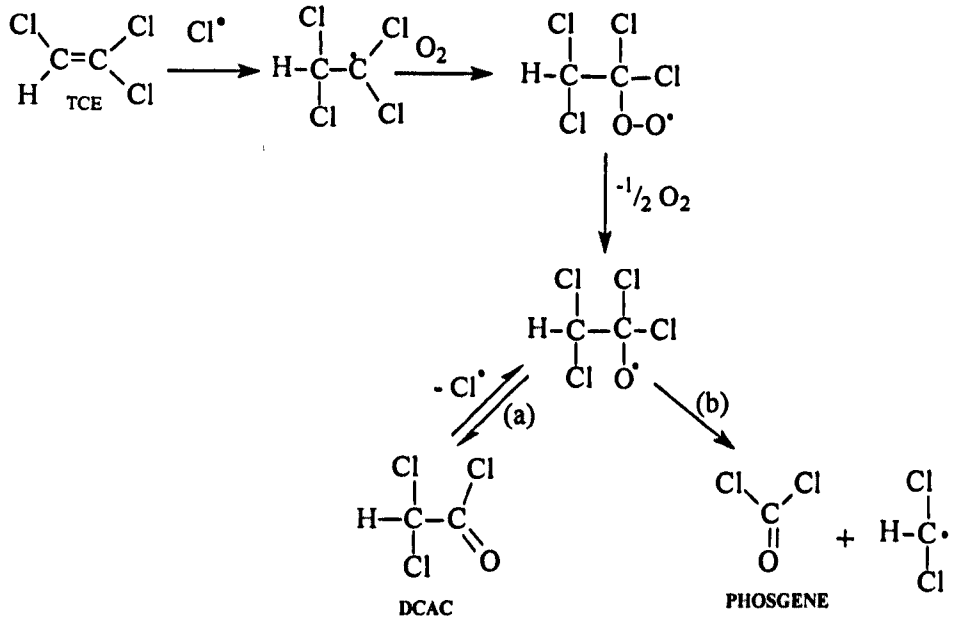

Fig. 2.19. Mechanism of DCAC and Phosgene formation through Chlorine attack on TCE.

Chapter 3

Analytical techniques

3.1 Introduction

The physical and chemical properties of titania such as crystalline phase, crystal and particle size, porosity and surface composition strongly influence its effectiveness as photocatalyst (Section 2.1.4). Therefore, the accurate characterisation of material's properties is of crucial importance for the evaluation of titania preparation methods and interpretation of photoactivity results.

In this chapter, the basic principles and concepts concerning the analytical techniques used in this work for the characterisation of TiO_2 photocatalysts are briefly reported.

3.2 X-Ray Diffraction (XRD)

Titania exists in three main crystalline phases: anatase, rutile and brookite; which show different photocatalytic properties (Section 2.1.4.1). X-ray diffraction is a quick and reliable technique for the determination of titania crystallographic properties.

X-ray diffraction (XRD) is a powerful and non-destructive technique for the characterisation of solid materials. XRD technique takes advantage on the coherent scattering of X-rays by crystalline and polycrystalline solids to obtain a diffraction pattern, which is unique and can be considered as a fingerprint of the material itself. This technique reveals a wide set of analytical and structural information such as crystal phase composition, preferred orientation and average crystallite size (Nefedov, 1988).

About 95% of all solids can be described as crystalline or polycrystalline. In crystalline materials the atoms are organised in planes that form a three-dimensional structure i.e. the crystal lattice. Most crystals can have many sets of planes, each of them with a specific interplanar distance (Fig. 3.1). By interaction of the atom planes with a focused X-ray beam, absorption, transmission, refraction and diffraction phenomena occur. The pattern obtained as result of the interference of diffracted waves reflects the crystallographic properties of the material.

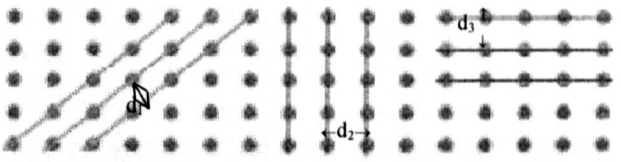

Fig. 3.1. Different planes and correspondent interplanar distances d_1, d_2 and d_3 existing within a crystal.

X-rays are electromagnetic radiation characterised by high quantum energy and very short wavelength. For diffraction application only hard X-rays in the range of 1 keV-120 keV, which correspond wavelength from few angstrom to 0.1 Å, are used. X-rays are produced by bombarding a solid target, usually copper or molybdenum, with a focused electron beam accelerated across a high voltage field. The wavelength of the X-rays obtained is characteristic of the nature of the target used, for example Cu emits 8 keV X-rays with corresponding wavelength of 1.54 Å, while Mo emits 14 keV X-rays with correspond wavelength of 0.8 Å. The wavelength in this range, are comparable with the distance separating ions or atoms in a crystal, and causes a crystal to diffract an X-ray beam passing through it (Warren, 1990).

In a laboratory instrument, the X-rays are produced in a sealed tube under vacuum, collimated and directed on the sample surface. A detector detects the diffracted X-ray waves and the signal is then processed and converted to a count rate.

3.2.1 The Bragg's law

The Bragg's Equation (Eq. 3.1) solves the relationship between wavelength, atomic spacing (d) and angle θ in X-ray diffraction. It was derived by the English physicists Sir W.H. Bragg and his son Sir W.L. Bragg in 1913.

$$n\lambda = 2d \sin\theta \qquad \text{(Eq. 3.1)}$$

The variable d is the distance between atomic plans in a crystal, λ is the wavelength of the incident X-ray beam; θ is the diffraction angle and n is an integer (Atkins, 1998).

Bragg's Law can be derived from geometrical analysis of the conditions necessary to make the phases of the beams coincide, when the incident angle equals the reflecting angle. Consider two planes separated by a distance d and an X-ray beam incident on the planes as shown in Fig. 3.2. The two parallel incident rays 1 and 2 make an angle θ with these planes.

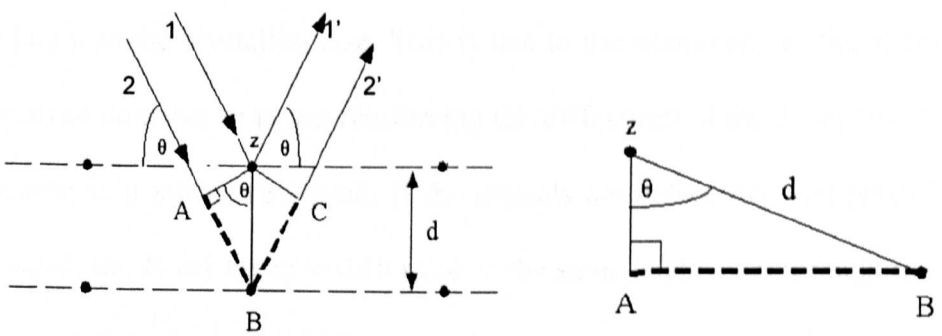

Fig. 3.2. Geometrical derivation of the Braggs' Law.

A reflected beam of maximum intensity will result if the waves represented by 1' and 2' are in phase. The difference in path length between 1 to 1' and 2 to 2' (AB+BC) must then be an integral number of wavelengths, λ.

$$n\lambda = AB + BC \qquad \text{(Eq. 3.2)}$$

Recognizing d as the hypotenuse of the right triangle ABz, trigonometry can be used to relate d and θ to the distance (AB + BC).

$$AB = d \sin\theta \qquad \text{(Eq. 3.3)}$$

Because AB = BC eq. (3.3) becomes:

$$n\lambda = 2AB \qquad \text{(Eq 3. 4)}$$

Finally, the Bragg's law equation is obtained by substituting Eq. 3.3 in Eq. 3.4

$$n\lambda = 2\, d \sin\theta$$

3.2.2 Scherrer's Equation

The use of Scherrer's equation is the simplest method to calculate the crystallite size from the XRD pattern. It is performed by measuring the broadening of a particular peak associated with a particular planar reflection from within the crystal unit cell. Crystalline size is inversely related to the full width at half maximum (FWHM) of an individual peak. The narrower the peak, the larger is the crystallite size. This is due to the periodicity of the individual crystallite domains in phase reinforcing the diffraction of the X-ray beam, thus resulting in a tall narrow peak. If the crystals are defect free and periodically arranged, the X-ray beam is diffracted to the same angle even through multiple layers of the specimen. If the crystals are randomly arranged or have low degrees of periodicity, and the result is a broader peak.

Scherrer's equation can be derived from Bragg's law by multiplying both sides of Eq. 3.1 by an integer m such that md=t, the thickness of the crystal:

$$m\lambda = 2\ md\ \sin\theta = 2t\ \sin\theta \qquad \text{(Eq. 3.5)}$$

Differentiating both sides of Eq. 3.5:

$$2\ \Delta t\ \sin\theta + 2t\ \cos\theta\Delta\theta = 0 \qquad \text{(Eq. 3.6)}$$

The thickness of the crystal t is:

$$t = \frac{\Delta t \sin\theta}{\cos\theta\Delta\theta} \qquad \text{(Eq 3.7)}$$

Since the smallest increment in t is d, using $\Delta t = d$

$$t = \frac{d \sin\theta}{\cos\theta\Delta\theta} \qquad \text{(Eq. 3.8)}$$

Substituting $2\Delta\theta$ with the angular width B and $d\sin\theta$ with $\lambda/2$ (from Bragg's law) we obtain the Scherrer's equations:

$$t = \frac{\lambda}{B\cos\theta} \qquad \text{(Eq. 3.9)}$$

A more sophisticated analysis of the problem adds a prefactor of 0.89 to the right hand side of Eq. 3.9 and leads to the correct Scherrer's equation (Eq. 3.10) (Atkins, 1998).

$$t = 0.89\frac{\lambda}{B\cos\theta} \qquad \text{(Eq. 3.10)}$$

3.3 N_2 adsorption-desorption studies

3.3.1 Introduction

In heterogeneous photocatalysis process, the adsorption of reactants on the

catalyst surface is a key step. Therefore, the characteristics of the catalyst surface that influence the adsorption process are of fundamental importance. Porosity and surface area determine the contact between active sites and reactants at the catalyst surface. Materials with porous structure are believed to facilitate the transportation of reactants to the catalyst surface (Yamazaki-Nishida *et al*, 1996). In materials with large surface area, the adsorption rate of reactants and the number of active sites at the catalyst's surface increase (Section 2.1.4.2). The study of the gas adsorption properties allows the determination of surface area, pore size distribution and quality of pores.

According with the pores mean diameter d, a solid can be classified in microporous ($d<2$ nm), mesoporous ($2<d<50$ nm) and macroporous ($d>50$ nm). Adsorption is a process that occurs when a molecule (the adsorbate) bonds to the surface of a solid (the adsorbent). Depending on the type of bonding forces involved, the adsorption can be classified in two broad categories: physisorption and chemisorption (Ruthven, 1984). Physisorption is a general process that occurs at every gas-solid interface and the interactions between adsorbate and adsorbant involve long-distance, weak 'Van der Waalls' forces. These interactions lead to multilayer surface coverage characterized by enthalpy comparable to condensation enthalpy of the adsorbate (Attard, 1998). Physisorption is of associative type and it is usually reversible (desorption process). On the other hand, chemisorption occurs through the creation of a chemical bond (ionic or covalent) between adsorbate molecule and specific surface sites on the adsorbant. Hence, chemisorption is characterized by chemical specificity and high enthalpy. The saturation point is the monolayer formation. If the adsorbant is a molecule, a dissociative process with molecule

fragmentation can take place, thus upon desorption the original specie cannot be recovered.

3.3.2 Adsorption-desorption isotherms

The quantity of gas adsorbed in a gas-solid system depends on the nature of the gas and the solid. It is proportional to the mass of the adsorbant and depends on the temperature and pressure of the system. For a fixed gas-solid system at constant temperature, the relationship between the amount of gas adsorbed and its pressure is described through the adsorption isotherms.

$$n = f(P)_T \qquad \text{(Eq. 3.11)}$$

The IUPAC classification of isotherms for vapor-solid equilibria is reported in Fig. 3.3.A. Type I Isotherm is typical of microporous adsorbents as the majority of micropore filling occurs at relative pressures below 0.1. The adsorption of nitrogen at 77 K on activated carbons show this kind of isotherm.

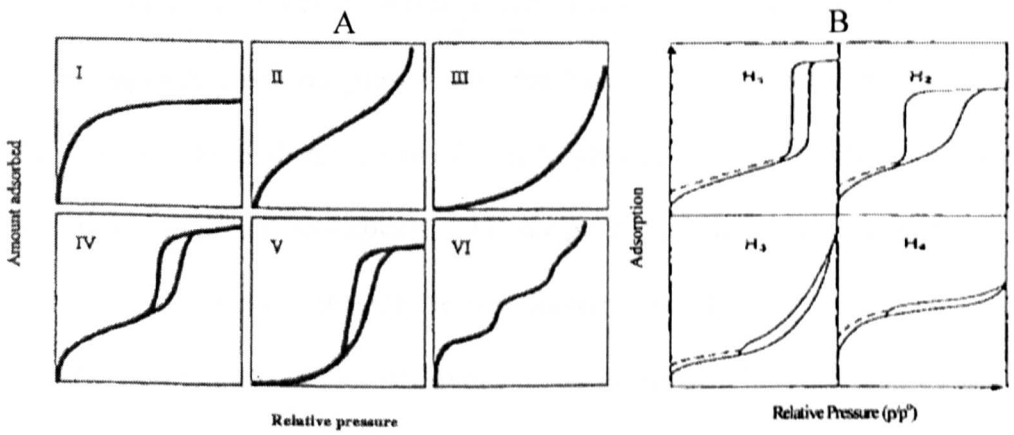

Fig. 3.3. IUPAC isotherms classification of gas adsorption-desorption isotherms (A) and hysteresis loops (B) (Sangwichien et al., 2002).

Type II and type III Isotherms identifies the physical adsorption of gases by non-porous solids with strong and weak adsorbate-adsorbent interactions,

respectively. Type IV and V isotherms present a hysteresis loop, which is associated with the presence of mesopores. Type V correspond to weak adsorbate-adsorbent interactions and is quite rare. The filling of mesopores occurs through a capillary condensation mechanism (Sing, 2001).Since the capillary condensation occurs at higher pressures than the capillary evaporation, the hysteresis loop is observed.

The hysteresis loops may exhibit different shapes as shown in Fig. 3.3.B (Sangwichien et al., 2002). In type H1, the hysteresis loop is narrow, with the adsorption and desorption branches almost vertical and nearly parallel, indicating a narrow pore-size distribution. Type H1 has been associated with porous materials made from agglomerates of spherical shape uniform in size dimension. The type H2 loop is broad with a desorption branch much steeper than the adsorption branch. Type H2 can be found in systems with a broad distribution of pore sizes and pore shapes within the material. It is believed that this kind of loop results from pores with narrow necks and wide bodies (ink-bottle shape) or when the porous material has an interconnected pore network. The type H3 loop does not exhibit any plateau at high relative pressures, indicating significant adsorption. This shape is associated with aggregates of plate-like particles that give rise to slit-shaped pores. Finally, the type H4 loop is nearly horizontal and parallel over a wide range of relative pressures and is associated with narrow slit-like pores (Sangwichien et al., 2002). In conclusion, Type VI Isotherm occurs rarely and presents steps due to the formation of monomolecular layers.

3.3.3 Surface area calculation: Langmuir and BET methods

Adsorption has been widely studied in the past two centuries and several mathematical models have been developed to fit adsorption isotherms. Langmuir published a isotherm model based on an adsorption kinetic mechanism which is based on the following assumptions:

1) The surface of the solid is uniform and all surface adsorption sites are equivalent.
2) The interaction between adsorbed molecules is negligible.
3) The adsorption takes place through the same mechanism.
4) The maximum adsorption corresponds to the formation of a monolayer on the solid surface.

The Langmuir equation is:

$$\frac{V}{Vm} = \frac{bP}{1+bP} \qquad \text{(Eq. 3.12)}$$

Where V is the amount of adsorbate adsorbed, V*m* is the monolayer capacity of the adsorbent, P is the pressure of the system and b is the Langmuir constant (Langmuir, 1918). From Eq. 3.12 is possible to calculate the Langmuir surface area of the adsorbent (A) using the formula:

$$A = V_m L a_m \qquad \text{(Eq. 3.13)}$$

Where L is the Avogadro's constant and a_m is the average area occupied by one molecule of adsorbate. In case of N_2 at 77K $a_m = 0.162$ nm^2 (Sing, 2001).

The major restriction for the use of the Langmuir adsorption is the assumption of a monolayer formation, which limits its applicability to

physisorption systems. The Langmuir isotherm is generally considered valid for chemisorption processes where the monolayer coverage approximation is realistic.

Brauner, Emmett and Teller in 1938 modified the Langmuir model introducing the concept of multilayer adsorption (Brunauer *et al.*, 1938). The assumptions made in the BET model are (Sing, 2001):

1) The molecule in the first coverage layer act as sites for molecule in the second layer and so on for molecule in higher layers.
2) No lateral interaction between adsorbate molecule are allowed.
3) At equilibrium, the rates of condensation and evaporation are equal for each individual layer.
4) An infinite number of layer can be obtained.

The resulting BET equation is:

$$\frac{P}{V(Po-P)} = \frac{1}{VmC} + \frac{(C+1)}{VmC} \times \frac{P}{Po} \qquad \text{(Eq. 3.14)}$$

Where V is the volume adsorbed, Vm is the volume adsorbed correspondent to the monolayer formation, P is the pressure of the system, Po is the saturation pressure of the gas at the temperature of analysis and C is a constant related to the enthalpy of adsorption of the first monolayer.

Practically, the measurement occurs by using a discontinuous method, where the quantity of gas adsorbed (N_2 at 77K) and the corresponding sample relative pressure P/P_0 are measured point by point and used to fit Eq. 3.14.

The BET surface area can be calculated from Vm value, by applying Eq. 3.13.

Due to the assumptions in the BET theory, the linearity of BET equation is limited to a small portion of the N_2 adsorption isotherm, usuall for partial pressures $P/P_0<0.3$.

3.3.4 Pore volume and pore size distribution: BJH model

Classical mesopores size distribution calculations are based on the analysis of the desorption branch of a type IV isotherm. The most common methods utilises the BJH theory (Barrett, Joyner and Helanda, 1951). It assumes a mono-multilayer formation in the mesopores and subsequent capillary condensation. This mechanism is illustrated below in Figure 3.5.

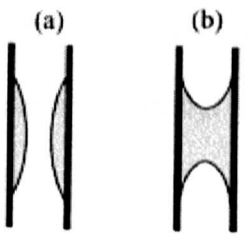

Fig. 3. 4. Mechanism of capillary condensation (a) low P/P_0; (b) high P/P_0.

Kelvin equation (3.15) predicts the partial pressure at which the gas condenses (or evaporates) in a cylindrical pore of a given size r. In this equation γ is the surface tension of adsorbed gas. Eq. 3.15 is used to obtain a relationship between P/P_0 and r, which in case of N_2 is equal to Eq. 3.16.

$$\ln\frac{P}{Po} = \frac{2\gamma Vm}{rRT} \qquad \text{(Eq. 3.15)}$$

$$\ln\frac{P}{Po} = \frac{-4.14}{r} \qquad \text{(Eq. 3.16)}$$

The BJH approach calculation of adsorbed volume, utilises the desorption branch, thus starts at $P/P_0=1$, assuming that all pores are filled. The desorption

process is assumed to occur through capillary evaporation from the interior of the pore, progressively decreasing the radius r. When P/P_{01} (to which correspond r_1) is lowered to P/P_{02}, (to which correspond r_2), a volume V will desorb from the surface. The pore volume of the largest pore is given by:

$$Vp = V\left(\frac{r1}{r2+\frac{\Delta t}{2}}\right)^2 \qquad \text{(Eq. 3.17)}$$

3.4 Electron Microscopy

TiO_2 nanoparticles were prepared and studied in this work. Electron microscopy techniques are widely used in nanotechnology and nanoscience research to yield information about the topography, morphology, composition and crystallographic characteristics of nanoparticles and nanostructured materials (Flegler *et al.*, 1993).

Electron microscopes were developed to address the resolution limitations of optical microscopy.

The Rayleigh criterion defines the resolution of light microscope as:

$$\delta = \frac{0{,}61\lambda}{\mu \sin\beta} \qquad \text{(Eq. 3.18)}$$

Where: λ is the wavelength of the radiation, μ is the refractive index of the view medium and β is the semi-angle of collection of the magnifying lens (Flegler *et al.* 1993). The resolution is mainly decided by the wavelength of the radiation source, and for optical microscopy it corresponds to 0.2 μm.

An electron microscope operates on the same basic principles as the optical microscope but uses beam of highly energetic accelerated electrons instead of

visible radiations, in order to achieve a very high resolution. The De Broglie relationship (Eq. 3.18) where h is Planck's constant, m, v and λ are the mass, velocity and wavelength of the particle respectively, indicates that the faster the electron the shorter is the wavelength, thus the higher is the resolution. In addition, electrons can be refracted easily, using magnetic fields, in order to form an image (Fleger et al. 1993).

$$\lambda = \frac{h}{mv} \qquad \text{(Eq 3.18)}$$

In electron microscopies, the electron beam is provided by an electron gun. A commonly used electron gun in modern instruments is the thermoionic gun. In the thermoionic electron gun a compound with high melting point and low work function (e.g. tungsten, LaB_6 or CeB_6) is heated to provide the electrons enough thermal energy to overcome the work function of the source and be emitted. The emitted electrons are then given velocity and directed towards the specimen by an electrical field. To avoid interactions between the electrons and air all the system works under ultra high vacuum conditions (10^{-7}-10^{-9} torr).

3.4.1 Scanning Electron Microscopy (SEM)

Scanning electron microscopy is a surface analysis technique that provides images of samples on a microscopic scale. It was used for the investigation of morphology of catalysts surface and the evaluation of particle size shape and dimension.

In SEM the electron beam focuses on the surface of the sample over a very small area, and it is scanned over the entire specimen. The interaction between the electron beam and the specimen causes different effect like secondary electrons emission, electron backscattering, catholuminescence or X-rays

emission. All these effects can be used to produce an image using a suitable detector that produces an electrical signal. This signal is finally processed and amplified to generate a point of brightness on the screen. The image is built up scanning the electron beam on the sample in synchrony with the scan on the screen.

A schematic drawing of a scanning electron microscopy is given in Fig 3.5.

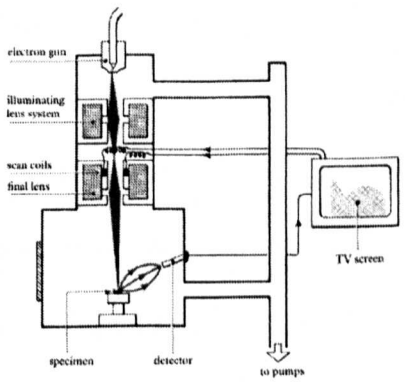

Fig. 3.5. Schematic drawing of a scanning electron microscope with secondary electrons forming the images on the TV screen (Perkes, 2008).

In SEM the magnification of the image is obtained controlling the ratio of the area scanned of the specimen to the area of the screen. Increasing of magnification is achieved quite simply by scanning the electron beam over smaller area of specimen. Conductivity and vacuum compatibility are the only special requirements for the sample. Insulating or semiconductive samples must be coated either with carbon or gold thin films.

3.4.2 Transmission Electron Microscopy (TEM)

In the frame of this work, TEM technique was used to determine the crystallite size of titania and confirm the data obtained by the application of Scherrer's equation on the XRD patterns. The transmission electron microscope was first

developed in the 1930's and nowadays is one of the most powerful surface techniques. Different kinds of information can be achieved by TEM analysis: the morphology of the sample, the crystallite size, shape and arrangement of the particles. Moreover, crystallographic information and the detection of atomic-scale defects is possible. Finally, if so equipped also the composition of the specimen can be studied. The electrons emitted from the electron gun are accelerated by high voltage (50 and 150 kV). The accelerated ray of electrons is focused on the specimen by a serie of electronic coils generating an electromagnetic field. It then passes through the object, where it is partially transmitted. As the electron beam passes through the specimen, some electrons are scattered whilst the remainder are focused by the objective lens either onto a phosphorescent screen or photographic film to form an image.

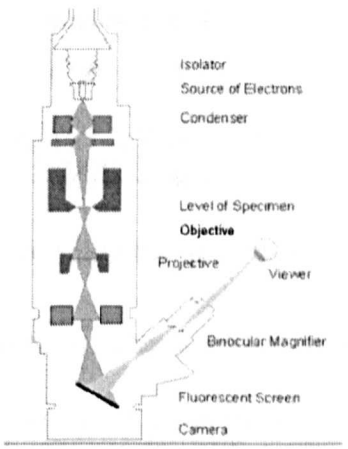

Fig. 3.6. TEM's instrument scheme.

The higher resolution achievable with a modern TEM microscope is 0,5-0,1 nm. However, the power of resolution of electron microscopy is usually controlled by the quality of the lens-systems. Materials for TEM must be specially prepared to thicknesses, which allow electrons to transmit through the sample (Flegler *et al.*, 1993).

3.5 X-Ray Photoelectron Spectroscopy (XPS)

X-ray Photoelectron Spectroscopy is a quantitative spectroscopic technique that measures the elemental composition and chemical state of the elements within a solid surface. The technique is based on the photoelectric effect, described by Einstein in 1905, where valence or inner shell electrons are ejected from a surface due to absorption of photons of appropriate energy (Watts, 2003).

In XPS the sample is illuminated with soft X-rays in ultrahigh vacuum conditions. AlKα (1486.6eV) or MgKα (1253.6eV) are often used as monochromatic sources of photons. By interaction with the photons, core electrons are emitted from the specimen (photoelectrons).

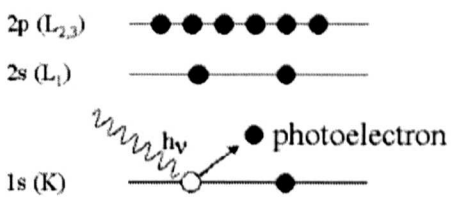

Fig. 3.7. Diagram describing the photoelectric effect.

The ejected photoelectrons are characterized by kinetic energy that depends on its provenance shell. Thus, for a given element, electrons with a variety of kinetic energies are ejected because of the different energies associated with each shell. The kinetic energy of the photoelectrons is measured and converted to the binding energy BE with Eq. 3.19 and it is equal to the energy of the exciting radiation (hν) minus the binding energy (BE) of the electron minus the work function ϕ of the material.

$$E_k = h\nu - BE - \phi \qquad \text{(Eq. 3.19)}$$

The XPS spectra is a plot of the intensity (counts of electrons) versus the BE. The binding energies of the core electron of an element have a unique value, which allows the identification of the chemical composition.

Furthermore, the binding energy of core electron is very sensitive to the chemical environment of the element. In fact, if the same atom is bonded to the different chemical species, the binding energy of its core electron is different. The variation of binding energy results in the shift of the corresponding XPS peak, ranging from 0.1eV to 10eV. This effect known as "chemical shift" is used to identify the chemical status of elements in the surface (Watts).

Chapter 4

Methodology

4.1 Catalyst preparation

4.1.1 Materials and chemicals

All chemicals and solvents used in the syntheses were supplied by Fluka and were used without any further purification. Ultrapure water was obtained by Nanopure Diamond ultrapure water system (water conductivity: 18.2 MΩ-cm). Commercial TiO_2 P-25 was supplied by Degussa.

4.1.2 Pristine TiO_2 catalysts

4.1.2.1 Amorphous TiO_2: synthesis route 1

A solution of 30 ml of Titanium isopropoxide, TIP (Fluka, purity 99,9%) in 20 ml of isopropanol was slowly dropped to mixture of 49 ml of isopropanol and 11 ml of water. The addition was conducted in air, under continuous magnetic stirring, dropping the precursor very slowly using an addition funnel equipped with pressure equalizer that guarantees the drop's homogeneity during the addition time. The white suspension obtained was kept under stirring for one hour, to allow the hydrolysis-condensation reaction to occur. The solid was filtered under vacuum through a sintered funnel of porosity 4, washed thoroughly with ethanol and dried in the oven at 80° C overnight. The solid obtained were grounded for further treatment. The reaction yield was about 80-85%. Amorphous powders obtained by synthesis route 1 gave rise to sample TT01-TT04 and HY01-HY04.

4.1.2.2 Amorphous TiO_2: synthesis route 2

A solution of 5 ml of Titanium isopropoxide, TIP (Fluka, purity 99,9%) in 25 ml of ethanol was slowly added dropwise to a mixture of 25 ml of ethanol, 0.5 ml H_2O and 0.5 ml HCl 0.1 M. Same as in Route 1.

Amorphous powders obtained by synthesis route 2 gave rise to samples TTA03 and TTA04.

4.1.2.3 Amorphous TiO_2: synthesis route 3

A solution of 30 ml of Titanium isopropoxide, TIP (Fluka, purity 99.9%) in 20 ml of isopropanol was slowly dropped to mixture of 270 ml of ethanol, 5 ml of water and 0.7 ml of glacial acetic acid. Same as in Route 1.

Amorphous powders obtained by synthesis route 3 gave rise to samples TTA01 and TTA02.

4.1.2.4 Thermal treatment

Thermal treatments on amorphous powders were carried out using a multistep programmable furnace (Carbolite CWF 1100). 3g of amorphous powder were placed in a ceramic crucible and calcined at temperatures between 400 and 600 °C. Target temperature was reached using a ramp rate of 5 °C/min, and kept for a period between 3 and 5 hours depending on the sample. The furnace was then allowed to cool down naturally to room temperature. After calcination, samples were ground and stored in a dessiccator for characterisation.

4.1.2.5 Hydrothermal treatment

A small amount of amorphous powder (0.6-0.8 g) was added to a mixture of water and isopropanol in different proportions. The quantity of water in the mixture expressed in molar fraction was varied between 0.59 and 0.88. The suspension was sonicated in water bath for 10 minutes, until homogeneity was reached, then it was transferred in a 150 ml Teflon lined autoclave vessel, sealed (PTFE-4748, Parr Scientific) and heated in oven at 150 °C for 8 hours. After treatment in the oven, the system was allowed to cool at room temperature and the solid obtained was filtered under vacuum through a glass sintered of porosity 4, washed twice with water, ethanol and acetone respectively. The solid was dried at 50 °C for 2 hours, ground and stored in dessiccator for characterisation.

4.1.3 N-doped TiO_2

4.1.3.1 Method 1: N insertion during sol-gel

A solution of 15 ml of Titanium isopropoxide, TIP (Fluka, purity 99,9%) in 20 ml of isopropanol was slowly dropped to mixture of 24 ml of isopropanol, 5 ml of water and 5 ml of NH_3 26%. The suspension obtained was kept under stirring for one hour, to allow the hydrolysis-condensation reaction to occur. The solid was filtered under vacuum through a sintered funnel of porosity 4, washed thoroughly with water until neutral pH of water phase, then rinsed with ethanol and dried in the oven at 80° C overnight.

4.1.3.2 Method 2: N insertion on amorphous TiO_2

Amorphous TiO_2 was prepared by following the synthesis route 1. 3 g of amorphous TiO_2 powder were suspended in a solution of 5 ml of NH_3 26% in isopropanol or 5 ml triethylamine (NEt_3) in isopropanol and left under vigorous stirring at room temperature overnight. The powder was recovered by vacuum filtration on a sintered funnel of porosity 4, washed thoroughly with water until neutral pH of water phase and dried in the oven at 110° C for 3 hours.

4.1.3.3 Method 3: hydrothermal synthesis

1.5 g of Titanium oxisulfate ($TiOSO_4$) were mixed with a solution of 2.5 ml of NH_3 26% in 100 ml of water:isopropanol 1:3 (pH=12). The mixture was placed in the 150 ml Teflon line autoclave vessel (PTFE-4748, Parr Scientific) and heated in the oven at 120 °C for 12 hours. The powder obtained was filtered under vacuum, on a sintered funnel of porosity 4, washed thoroughly with water until neutral pH of water phase and dried in air overnight. Powders were treated by thermal process following procedure reported in section 4.1.2.4.

4.1.4 TiO_2/WO_3 composites

A novel synthetic route was developed and optimised for these materials. Titanium oxysulfate ($TiOSO_4$) and ammonium metatungstate hydrate ($(NH_4)_6(W_{12}O_{41})\cdot xH_2O$) were used as precursors for TiO_2 and WO_3 respectively. Appropriate amount of precursors were mixed with 100 ml of H_2O, ethanol or a mixture of the two solvents in different proportions. The suspension was transferred in a 150 ml Teflon lined autoclave vessel (PTFE-

4748, Parr Scientific) and reacted solvothermically in oven. After reaction the solid obtained was recovered by filtration using a sintered funnel of porosity 3, washed thoroughly with copious amount of water, followed by acetone. The solid was dried in the oven at 50 °C for 1 h, and left cooling in a desiccator. The powder was grounded, and stored in dessiccator for characterisation. To optimise the synthetic process, three reaction variables were considered: solvent composition, reaction temperature and reaction time. Each sample was prepared twice to assure consistency in the preparation method.

4.1.4.1 Synthesis optimisation

To study the effect of solvent composition, the hydrothermal reaction was carried out in pure water, pure ethanol and in mixtures of H_2O/Ethanol varying the water content from 30 to 70%. The reaction was carried out at 150 °C for 24 hours.

The effect of reaction temperature was studied keeping solvent composition at constant water-ethanol ratio 1:1 and varying reaction holding time between 4 and 24 hours at 150 °C.

The effect of WO_3 loading was studied in the range 0-40% wt, carrying out the reaction for 12h at 150 °C with water ethanol ratio 1:1.

4.2 Characterisation

4.2.1 X-ray diffraction

X-ray diffraction (XRD) was performed using a HILTONBROOKS X-ray powder diffraction instrument, using (Cu radiation at 1.5406 Å) graphite monochromator, a scan speed of 2 degrees 2θ per minute, scan ranging from 5-

80 degrees 2θ. Diffraction peaks were identified according with the Joint Committee on Powder Diffraction Standards (JCPDS).

The mean particle size of the samples was calculated using Scherrer's equation from broadening of (101) anatase peak.

When necessary, the content of rutile was calculated by using the following equation:

$$f_R = \frac{1.26 I_R}{I_A + 1.26 I_R} \qquad \text{(Eq. 4.1)}$$

where: I_R and I_A are the (110) rutile peak and the (101) anatase peak intensities respectively.

4.2.2 Absorption analysis

N_2 adsorption-desorption isotherms at –196 °C were recorded using a Micrometrics ASAP 2010 or a Micrometrics ASAP 2020. All samples were degassed overnight at 110 °C prior analysis. The surface areas were calculated using a multipoint BET method using the absorption data in the partial pressure (P/P_0) range between 0.05 and 0.35. BJH method was used to determine the porosity of the samples in the range 2-300 nm.

4.2.3 Microscopy studies

Scanning Electron Microscopy (SEM) images were collected from a FEI XL30 scanning electron microscope fitted with a LaB_6 electron gun utilising a beam with accelerating voltage of 20kV. Samples for SEM analysis were gold coated to assure good conduction using a Poalron-500 sputter coater.

Transmission electron Microscopy (TEM) studies were carried out using a JEOL 2100f equipped with a field emission electron gun (FEG) operating at 200kV.

4.2.4 UV-visible Optical absorption properties

Diffuse reflectance spectra were collected using a PerkinElmer Lambda 35 UV/VIS Spectrometer equipped with a Labsphere RSA-PE-19 reflectance spectroscopy accessory, using barium sulphate as reference material.

4.2.5 XPS

X-ray photoelectron spectroscopy (XPS) was performed using a Kratos AXIS ULTRA with a mono-chromated Al Kα X-ray source (1486.6 eV) operated at 15 mA emission current and 10 kV anode potential. The analysis chamber vacuum was typically better than 10^{-9} Torr. Data were processed using CASAXPS software.

4.3 Photocatalytic reactor

A flat-plate single-pass gas phase photoreactor was used for evaluation of photocatalytic activity of catalysts. In this section a detailed description of the photocatalytic plate and reactor rig are reported. The reactor rig used in this work for the evaluation of catalysts activity was designed and built by Dr. Ignasi Salvado-Estevill (former PhD student, Schee).

However, the original design of the rig has been slightly modified during the course of the work in order to overcome some technical problems and improve the overall operative procedure. The modification made are reported and discussed in the following sections.

4.3.1 Description of flat-plate photocatalytic reactor.

The photocatalytic plate consists of a flat plate of stainless steel (dimension: 7.5 cm wide, 76 cm long) with a 2 mm deep engraved surface. The coated support is placed in a grove (7.5 cm wide, 10 cm long) located 27 cm from the inlet and 17 cm from the outlet. The inlet and the outlet were designed to minimize any backflow dispersion and are made entirely with stainless steel. The reactor is covered with borosilicate glass plate and sealed, forming with the engraved surface a narrow flow channel of 2 mm deep and 75 mm wide over the whole reactor.

The plate with the immobilised catalyst is positioned at the same level of the bottom surface of the stainless steel case in order to avoid turbulences in the air flow. A system of tubular lamps were placed on top of the reactor and used as irradiation source. A view of the photocatalytic plate and lamp holder system is shown in Fig. 4.1.

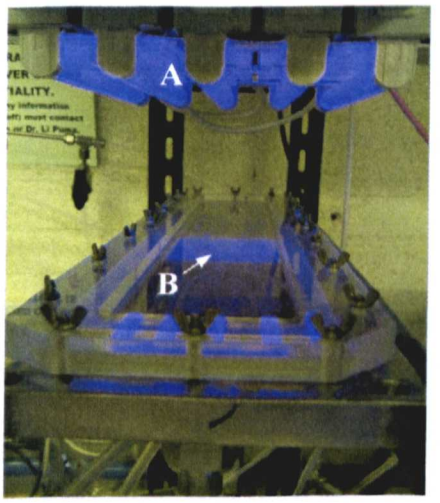

Fig. 4.1. Detail of the photocatalytic plate A) UVA lamps; B) coated photocatalytic plate.

UV-A irradiation was achieved by using blacklight blue fluorescent lamps (Philips TL 8W/08 F8 T5/BLB). The lamps emit between 343 and 400 nm with a maximum irradiance peak at 365 nm.

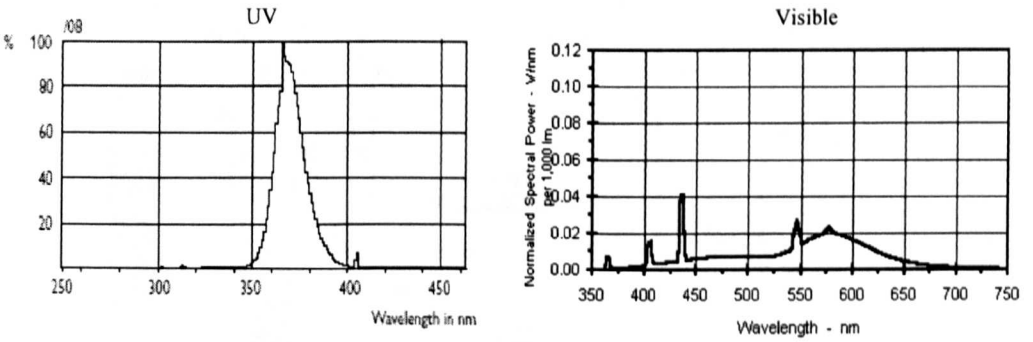

Fig. 4.2. Emitting spectrum of UV light source (blacklight blue fluorescent lamps Philips TL 8W/08 F8 T5/BLB) and visible light source (Sylvania halophosphor fluorescent lamps F8W/154 Daylight)

4.3.2 Reactor rig set-up

4.3.2.1 Original set up

A diagram of the original experimental set up is reported on Fig. 4.3. A three way valve V_1 allowed to select between N_2, which was used to flow the system before and at the end of experiment for cleaning purposes; and the synthetic air (BOC 20% O_2, 80% N_2), used as carrier gas. The gas-feeding stream was divided in three lines: two of them formed the dry stream passing through two identical flowmeters F_{D1} and F_{D2} (0-1.222 L/min, Cole-Parmer), while the third line was used to create a wet stream bubbling carrier gas in a water saturator kept at constant temperature (30 °C) in a water bath. Flowmeter F_W (0-0.264 L/min, Cole-Parmer) was used to control the inlet flow to water saturator. The gas streams rejoined before the pollutant injection point. The

thermohygrometer probe located downstream the conjuction point was used to monitor the relative humidity (RH) of the gaseous mixture.

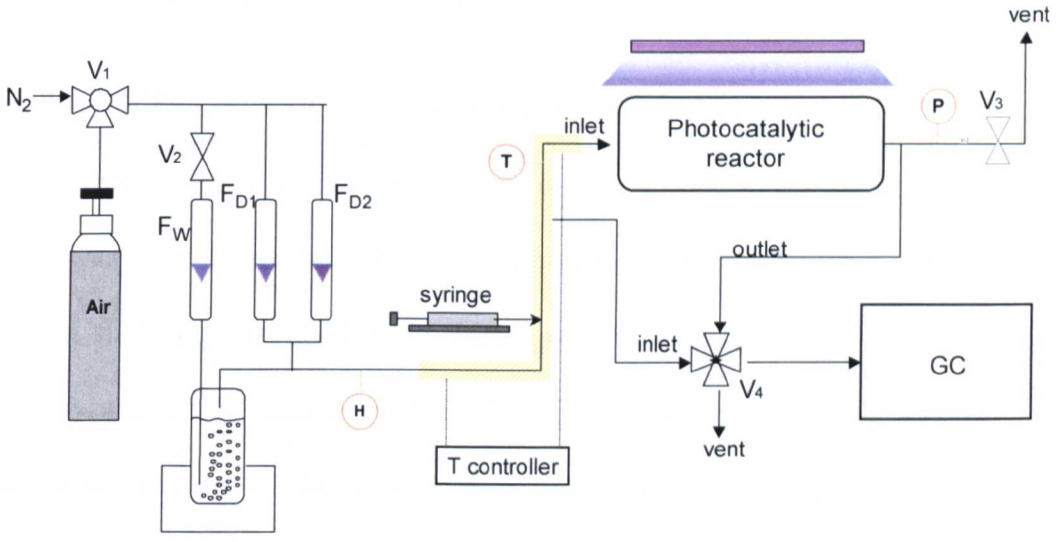

Fig. 4. 3. Original Experimental set-up of photocatalytic reactor rig.

An infusion syringe pump (Cole-Parmer) was used to inject continuously the pollutant in to the system. To allow the evaporation of the pollutant, the temperature of the upstream pipeline (indicated with yellow color in Fig. 4.3) was kept slightly higher than the pollutant evaporation point (i.e. 87.3 C in case of TCE), kept constant and monitored using a temperature controller (Cole-Parmer).

All tubing upstream the pollutant injection point were Teflon PTFE, while after the injection point stainless steel pipes were used to avoid absorption and corrosion problems and to facilitate cleaning process.

A pressure probe was located downstream the outlet. The pressure in the reactor could be controlled through valve V_4. Pressure in the reactor during experiments never exceeds 0.3 bar.

Irradiation sources were located on the top of the photocatalytic plate. The number of lamps used and their distance from the catalyst surface was adjustable, to allow the regulation of light intensity.

4.3.2.2 Photocatalytic experiment protocol

In a typical experiment, the coated support was placed in the grove and the reactor was carefully sealed. The system was flushed with N_2 for 5 minutes, and then slightly pressurized up to 1 bar (partially closing valve V_4) and the reactor was carefully checked for leaks by a liquid leak detector. Leak test was also carried out on all flowmeters connections. Fresh ultrapure water was placed in the water saturator. Valve V_1 was used to select the carrier gas and carrier gas flow was started. Temperature at the injection point was set, and water bath was switched on. All flowmeters were set to desired values depending on total flow wanted and relative humidity condition wanted. The syringe was filled with pollutant and the pump was set at the suitable injection rate. The GC method and sequence were set up. Valve V_4 was partially closed and pressure monitored until stabilization. When the temperature at the injection point, carrier gas flows and humidity were stabilized injection in the GC was started.

After starting injection, the concentration of pollutant in the inlet and outlet of reactor were monitored by mean of its FID chromatographic peak area (see Section 4.3.3). The system was considered at steady state when the concentrations in the inlet and outlet were the same with an error of 1%. After steady state was reached and kept for 30 minutes, the lamps were switched on and any change in pollutant concentration was evaluated by changes in outlet

concentration from FID chromatographic peak (see section 4.3.3). The conversion is considered at steady state when the same value (±5%) is recorded for more than 5 consecutive analyses. At this point the lamps were usually switch off to ensure that the actual conversion could be ascribed to photocatalytic process and not to leaks in the system or artifacts in the analyses procedure. The system is allowed to reach again the steady state condition before applying irradiation on the catalyst surface (Fig. 4.4).

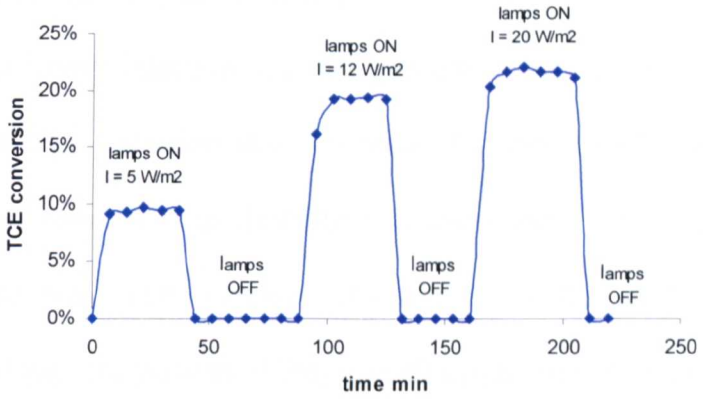

Fig. 4.4. TCE conversions vs. time diagram for a typical photocatalytic experiment.

After every experiment, the system was flushed with N_2 for 5 min, to eliminate any trace of contaminant from the rig and from the catalyst surface.

4.3.2.3 Problems encountered

During the first experiments on the photocatalysts evaluation, some drawbacks of the experimental set up became evident. The main disadvantages of the rig in its original configuration were related to the difficulty in obtaining a steady state of the pollutant inlet concentration, before and during the photocatalytic experiment. Moreover, the syringe pump revealed to be not the ideal system for the introduction of the pollutant in the system. The main

limitation experienced in operating the photocatalytic reactor are reported as follows:

The achievement of a stable TCE initial concentration at fixed injection rate.

1. Limitation in the initial concentration of TCE achievable by using the syringe pump as injection system. The injection rate of the syringe pump could be set in the range: 0-1.5 ml/h. However, preliminary experiments carried out in order to evaluate the reliability of the injection rate, showed that the lowest injection rate that guaranteed the achievement of a steady state of TCE injection was 0.5 ml/h. At rates lower than 0.5 ml/h the injection resulted very unstable and consequently the TCE peak areas obtained were very variable, indicating that the amount of pollutant injected was not constant during the injection time. It was observed that at low injection rates, the movement of the screw in the pump was not continuous and smooth, but it proceeded "by steps" causing the non-continuous injection. The inlet concentration of TCE was evaluated from the GC peak area at different injection rates. Figure 4.5 reports the concentration in μM and ppmv obtained at different injection rates, starting from 0.5 ml/h for the reasons reported above, considering two different air flow-rates. It can be seen that the lowest initial concentration of TCE achievable is 39 μM, equivalent to 950 ppm. Considering that in real air the VOCs concentration is in the ppm or ppb range, a lower initial concentration of pollutant than the one allowed by the syringe pump injection system is highly desirable.

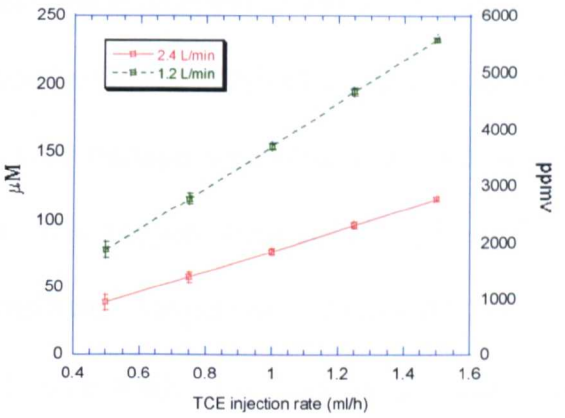

Fig. 4.5. Initial TCE concentration (at steady state) expressed in µM and ppmv as function of injection rate at total air flow rate of 2.4 L/min and 1.2 L/min.

2. Difficulties in obtaining a steady state of the initial concentration at fixed injection rate. Even at injection rates higher than or equal to 5 ml/min, a stabilization period between 2 and 6 hours was necessary before starting the photocatalytic experiment. Moreover, the injection through the syringe pump was very sensible to any vibration at the rig base e.g. caused by lamp adjustment.
3. Condensation problems: despite that the pipelines were kept at temperature higher than TCE's boiling point (87.3 °C), some condensation of TCE just before the inlet point of the reactor was experienced. The presence of condensation drops on the pipes and their spontaneous evaporation, caused instability in the pollutant initial concentration.

4.3.2.4 Improvements made and actual set up description

To overcome the issues described in the previous section, the following changes were made at the system configuration:

1. Injection system: the syringe pump was substituted by a Dreschel bottle containing a small amount (≈5 ml) of liquid TCE in equilibrium with the vapours. The flow through the bottle was controlled by a flowmeter (Cole-Parmer). The vapour pressure of TCE in the Dreshel bottle depends on temperature varying from 20 torr at 0 °C, 75 torr at 25 to 200 torr at 50 °C. The bottle was kept in a water bath at controlled temperature, or in an ice bath. The TCE concentration can be controlled by changing the gas flow inside the bottle, or by changing the temperature of the water bath. If the flow and the temperature are kept constant, the concentration of TCE in the inlet is constant.
2. The flowmeters were substituted with two precision mass and volumetric flow controllers (Cole-Parmer). The range covered by the flow-mass controllers is from 0 to 5 L/min. Final configuration of the reactor rig is reported in Fig. 4.7, where MCD and MCW indicates the mass flow controller used for the dry flow and for the humid flow respectively.

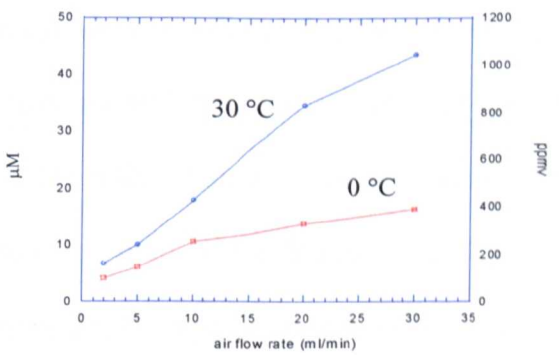

Fig. 4. 6. Initial TCE concentration (at steady state) expressed in µM and ppmv as function of air flow rate through Dreshel bottle saturated with TCE vapors in ice bath and at 30°C. Total flow rate: 2.4 L/min.

These modifications allow a better control of TCE initial concentration, to achieve a quicker stabilization of inlet TCE content. Moreover as shown in Fig. 4.6, it was possible to achieve lower TCE initial concentration than those achievable by using the syringe pump as injection system (See Fig. 4.5).

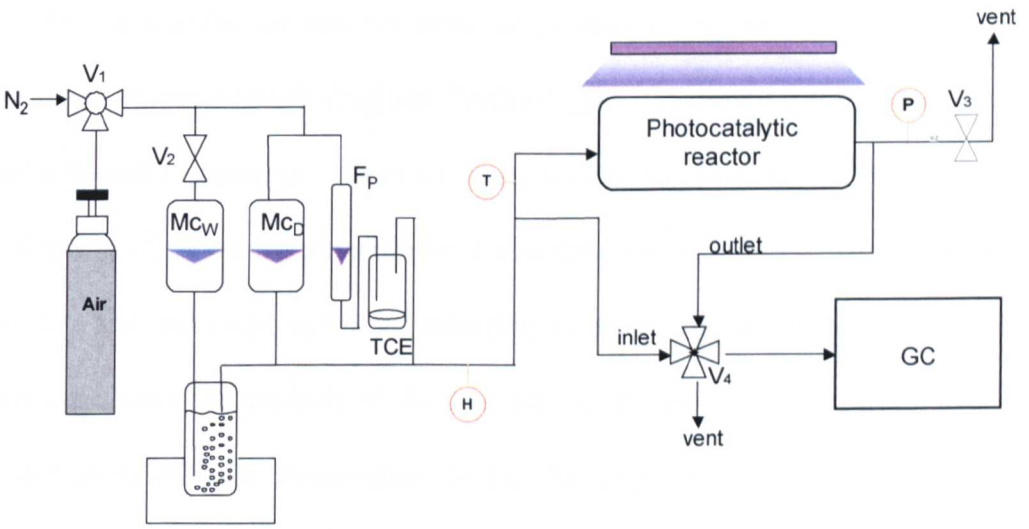

Fig. 4.7. Current configuration of experimental rig for evaluation of photocataytic oxidation of TCE in the gas phase, after modification of pollutant injection system.

4.3.2.5 Rig Cleaning protocol

Before each experiments the flat plate glass cover was cleaned carefully with ethanol and acetone and dried before to seal the reactor. In fact the presence of dust or dirt from fingerprint could interfere with light irradiation. For the same reason, the bulb of the lamps were cleaned periodically with acetone and left dry in air. On a periodic base the stainless steel part of the rig was dismounted and cleaned. This process was carefully carried out for reactor inlet and outlet pipeline and for pipeline that connect the inlet and outlet with the GC. The component parts were dismounted and washed with a 5% HCl solution for 30 min. Small part were sonicated in the acidic solution for 30 min,

while long tubes were rinsed several times with the solution. After being rinse with ultrapure water and acetone, all parts were dried with N_2 flow. The parts were mounted back and a leak test was carried out.

4.3.3 GC analysis

Inlet and outlet air streams from the photocatalytic reactor were connected to a gas chromatograph (Agilent Technologies, GC-6890N) through a system of automatic sampling valves (V_3). In reality V_3 consists of two valves: a sampling valve was responsible for the selection of sampling origin, i.e. inlet or outlet, and sampling valve for injection of gases into a sampling loop. This system allows the analysis of the inlet and outlet samples composition and the calculation of TCE conversion during the experiment. The volume of the sampling loop determines the injection volume in the GC column. In all our experiments a 1 ml sampling loop was used. The GC was equipped with a GS-GASPRO capillary column (30 m, 0.32 mm) for separation of analytes and Flame Ionization Detector (FID) for detection of organic and halogenated compounds and Thermal Conductivity Detector (TCD) for analysis of inorganic gases such as CO_2 detectors.

An isotherm method was used for the detection of TCE. Specification of the method are reported in Table 4.1.

4.3.3.1 Calibration

Calibration curves for the determination of TCE concentration from the FID peak areas were produced before every set of experiments. Standard solutions of TCE in cyclohexane were prepared, with TCE in the experiments concentration range. 1 μL injections were carried out at least in triplicate and

the peak area of obtained TCE peaks were manually integrated. The average values with correspondent standard deviations were used to construct the calibration curve. Good reproducible linear correlation between peak area and concentration were found.

Table 4. 1 GC method ISOTEMP1

INLET	FID
Mode: Split	Temperature: 250 °C
Gas: He	H_2 flow: 30 ml/min
Temperature: 200 °C	Air flow: 400 ml/min
Pressure: 0.733 bar	He flow: 25 ml/min
Flow: 178 ml/min	**TCD**
COLUMN	Temperature: 250 °C
Type: GC-Gaspro	Reference flow: 20 ml/min
Flow: 1.4 ml/min	He flow: 6 ml/min
OVEN	**AUXILIAR**
Temperature: 250 °C	Valve Box heater: ON
Hold: 4 min	Setpoint: 100 °C

4.3.4 Evaluation of incident photon flux on catalyst surface

The UVA lamps used in this work emit in the range 343-380 nm. UV radiation intensity at the catalyst surface was calculated measuring the incident flux using a radiometer (Cole-Parmer, Model Nr 97503-00) equipped with a 365 nm sensor. The intensity readings were carried out before every set of experiments, by placing the sensor, covered by the photoreactor glass cover, in correspondence of the centre of the photocatalytic plate. The distance between the sensor's surface and the tubular lamp axis was the same as the distance between the lamps and the catalyst surface during the photocatalytic experiments.

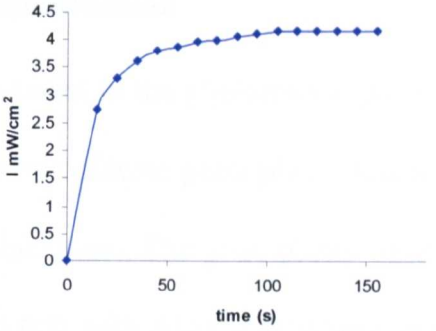

Fig. 4.8. Radiometer reading as function of time after switching on 5 lamps at 10 cm distance from 365 nm UVA sensor.

After switching on the lamps, the radiometer reading took about 1 minute to reach a constant value, as reported in Fig. 4.7.

The radiometer reading value was multiplied by a factor of 1.72 in order to obtain the average intensity along the useful spectrum of the irradiation source. This correction factor takes into account the intensity of the other wavelength not detected by the sensor and has been determined in a previous work (Salvado-Estevill, 2007).

4.3.5 Calculation of reaction rates

Photocatalyst activity was evaluated and compared in terms of average reaction rate r_{TCE}, calculated from the following equation:

$$r_{TCE} = \frac{F \times [TCE]_0 \times X}{A} \qquad \text{(Eq. 4.2)}$$

Where: F is the volumetric flow rate (L/s), $[TCE]_0$ is the initial concentration of TCE (μmol); X is the conversion of TCE at steady state; A is the area (m^2) of the illuminated coated support.

4.3.6 Catalyst immobilisation

The photocatalyst evaluated in the photoreactor were immobilised as thick non-transparent films on borosilicate glass plate (dimension: 10 cm length × 7.5 cm width × 0.5 cm thickness). The glass plates were cleaned in ultrasonic bath with ethanol, rinsed first with ethanol then with acetone, and allowed to dry at room temperature.

0.045 g of TiO_2 were ultrasonically dispersed in 5 ml of ethanol for 10 min, then pipetted uniformly on the glass plate surface achieving a TiO_2 loading of 0.6 mg/cm^2. The solvent was allowed to evaporate and the coated plates were heated at 120 °C in the oven for 2 hours.

Chapter 5

Pristine TiO_2

5.1 Introduction

Among the various methods available for the preparation of TiO_2 nanoparticles, sol-gel based syntheses offer several advantages (Section 2.2.5). Sol-gel preparation offers the possibility of preparing materials with different structural and morphological characteristics by tuning processing parameters with cost effectiveness and high reproducibility (Section 2.2.1). It is well known that changes in the TiO_2 materials properties reflect on TiO_2 photocatalytic activity. In this chapter the preparation, characterisation and photocatalytic evaluation of TiO_2 nanoparticles obtained reproducing and modifying a sol-gel based procedure (Maira *et al*, 2000) is presented and discussed. TiO_2 photocatalysts have been synthesised under different experimental conditions, with the aim of investigating:

1. The impact of acid addition during the hydrolysis-condensation reaction on material's properties and photocatalytic activity.
2. The effect of calcinations temperature in thermal treatment and the effect of solvent composition in the hydrothermal process on material's properties and photocatalytic activity

The first part of the chapter reports the crystallographic, structural and morphological characterisations of titania photocatalysts, investigating the eventual correlations between processing parameters and materials properties.

The second part of the chapter reports the results and the discussion of the photocatalytic test for TCE photoxidation in the gas phase, scrutinizing the correlation between activity and materials properties.

5.2 Synthesis of Titania samples

5.2.1 General synthesis scheme

The preparation method of all TiO_2 nanoparticles reported in this chapter is based on the modified two-steps sol-gel procedure, resumed in Scheme 4.1. In the first step, indicated as "sol-gel", a hydrolysis-condensation reaction is carried out at controlled parameters, leading to the formation of amorphous TiO_2. In this study the hydrolysis-condensation reaction was carried without acid addition (synthesis route 1-Section 4.1.2.1) and by adding HCl (synthesis route 2-Section 4.1.2.2) or glacial acetic acid (synthesis route 3-Section 4.1.2.3).

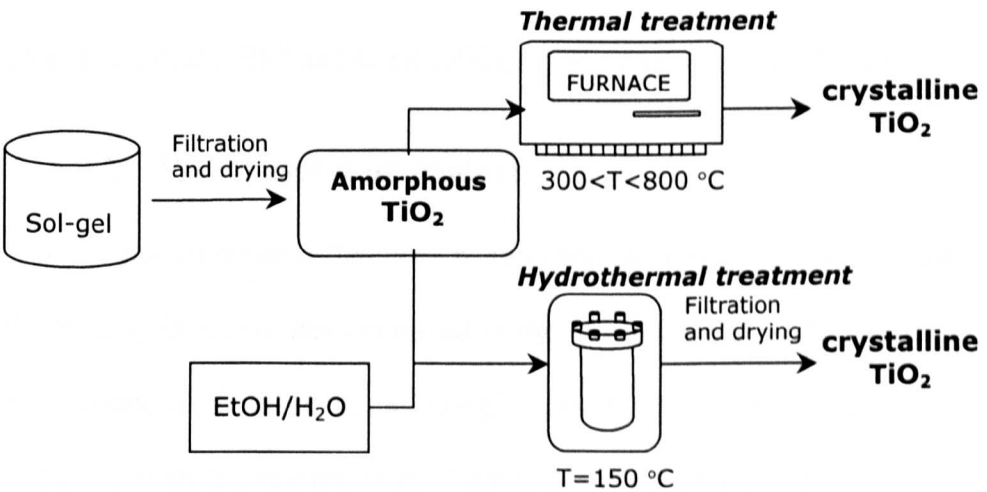

Fig. 5.1. Synthesis scheme employed for preparation of TiO_2 photocatalysts.

The second step of the preparation process consists of the conversion of amorphous TiO_2 to crystalline and photocatalytically active form of titania. Such crystallisation is achieved by either a thermal treatment i.e. calcination at high temperatures, or by a hydrothermal treatment in water/alcoholic solutions

at different solvent ratios, carried out at constant temperature and holding time, i.e. 150 °C/ 8h.

5.2.2 Samples prepared

Four different series of TiO_2 nanoparticles were obtained by changing the combination of hydrolysis and crystallisation conditions employed during the materials preparation.

Amorphous TiO_2 obtained under uncatalysed condition (synthesis route 1) were crystallised by thermal and hydrothermal methods, yielding to sample series TT and HY, respectively. Sample series TTA and HYA were prepared by thermal and hydrothermal crystallisation of amorphous powder obtained by hydrolysis-condensation conducted under acidic conditions. Two acids were used as catalysts: HCl and CH_3COOH, (synthesis route 2 and 3) (Table 5.1).

5.2.3 Visual aspect of products.

Some macroscopic differences were observed in the reaction products from the three synthetic routes employed in the preparation of TiO_2. Hydrolysis and crystallisation conditions for all samples reported in this chapter are resumed in Table 5.1 with the macroscopic observation of the product characteristics after each preparation step.

The hydrolysis–condensation carried out without acid (Route 1) yield a milky white solution as soon as the addition of the precursor was started (TIP). After one hour aging, a white powder decantates spontaneously from the reaction mixture. The formation of a milky solution was observed also when the hydrolysis-condensation reaction was carried out in the presence of HCl (Route 2). However, in this case, at the end of the aging time (1h) no

precipitation occurred and a thick colloidal suspension was obtained. Filtration or centrifugation was needed to isolate the titania powder. The suspension was found to be stable for a period of time of several days, after which a solid started to precipitate.

Table 5.1. Synthesis conditions and macroscopic appearance of hydrolysis-condensation and crystallisation products.

			Synthesis conditions			
Sample		Sol-gel			Crystallisation	
Series	Name	Route	Catalyst	Product	Thermal	Powder
TT	TT01	1	-	ppt	400 °C 4h	white
	TT02	1	-	ppt	450 °C 3h	white
	TT03	1	-	ppt	550 °C 5h	white
	TT04	1	-	ppt	600 °C 3h	white
TTA	TTA01	3	acac	sol	550 °C 5h	white
	TTA02	3	acac	sol	400 °C 4h	white
	TTA03	2	HCl 0.1 M	colloid	550 °C 5h	grey
	TTA04	2	HCl 0.1 M	colloid	400 °C 4h	grey
	Name		Catalyst	Product	Hydrothermal (150 °C 8h)	Powder
HY	HY01	1	-	ppt	X_{H_2O}=0.59;	yellowish
	HY02	1	-	ppt	X_{H_2O}=0.74;	yellowish
	HY03	1	-	ppt	X_{H_2O}=0.85;	yellowish
	HY04	1	-	ppt	X_{H_2O}=0.88;	white
HYA	HYA01	2	HCl 0.1 M	colloid	X_{H_2O}=0.59;	white
	HYA02	3	acac	sol	X_{H_2O}=0.59;	white

Finally, by using acetic acid during the sol-gel process (Route 3), a non-transparent and stable sol was obtained at the end of the reaction and aging time. The sol was found to be stable few weeks.

By using acetic acid the reaction environment is at pH 2.5-3. Following a method reported in the literature (Hamid and Rahman, 2003) the reactions were conducted using TIP:ethanol:CH_3COOH in ratio 1:45:0.3. In the reference considered, the addition of water to the reacting mixture is not mentioned,

however following this method no formation of TiO_2 was observed in the first 24 hours of reaction, thus a small amount (1 ml) of water was added to achieve reasonable reaction times.

The hydrolysis-condensation step can be driven towards the formation of different products, from transparent sols to powder precipitation, depending on the ratio between the hydrolysis and the condensation reaction rate, which depends on synthesis conditions (Table 2.3). The difference in products resulting from different hydrolysis condensation conditions i.e.: precipitate or sols with different stability can be attributed to the effect of the acid on hydrolysis and condensation reaction rates. When no acid is used (synthesis route 1) both hydrolysis reaction rate and condensation rate are fast and precipitate is the favoured product (Table 2.3). When an acid is added to the reaction environment, the presence of H^+ increases the Ti electrophilic property of the $Ti(OiPr)_4$ precursor, therefore favouring the nucleophilic attack from a water molecule. As a result, the equilibrium of the hydrolysis reaction of $Ti(OiPr)_4$ is shifted towards the formation of the hydrolysed product $Ti(OH)_4$. On the other hand, the addition of H^+ in the reaction environment has an inhibitory effect on the condensation reaction (Section 2.2.4). Generally, when condensation is slow, the formation of a sol is favoured. When acetic acid was used, the sol obtained was stable for longer period of time that the sol obtained with HCl. Acetic acid can also act as a ligand during the hydrolysis and condensation reaction, coordinating the Ti centre. Moreover, the hydrolysis condensation with acetic acid occurs in conditions of high dilution if compared with HCl reaction: the final total volume for route 3 was six times larger than for route 1 and 2.

Some visual differences in terms of colour and textures were noticed also in the crystallised powders. TiO_2 nanoparticles crystallised by the thermal treatment gave rise to white fine powders with the exception of amorphous TiO_2 obtained in presence of HCl that present grey colour after thermal treatment. TiO_2 nanoparticles obtained by hydrothermal treatment were powders with a coarse aspect, either white or yellowish. Each sample reported in Table 5.1 was prepared at least in duplicate and the differences in appearance were observed to be fairly reproducible.

5.3 Photocatalysts characterisation

The characterisation of the photocatalysts' structural and morphological properties by mean of X-ray diffraction studies, adsorption studies and microscopy studies (SEM and TEM) is reported in this section. The material properties are discussed in relation with the photocatalysts preparation conditions. Sample series obtained under uncatalysed conditions and those obtained in acidic conditions are considered separately, and a summary of the correlation between material properties and relevant experimental parameters is reported at the end of each section. The morphological and crystallographic properties of TiO_2 obtained under acidic conditions are also compared with the TiO_2 obtained without acid and crystallised in similar conditions.

5.3.1 Calcined samples (Series TT)

5.3.1.1 X-ray studies

X-Ray diffraction patterns reported in Fig. 5.2 provide informations about

the crystal phase composition and the crystal particle size of TiO_2 nanoparticles.

No diffraction peaks were found for powders obtained after hydrolysis-condensation reaction, confirming their amorphous nature. Samples calcined at temperature between 400 and 550 °C show characteristic anatase diffraction pattern according with JCPDS 21-1272, while TiO_2 calcined at 600 °C, shows clearly also the (110) rutile peak at $2\theta = 27.5°$. The rutile content in this sample has been estimated equal to 5%.

The peak corresponding to the strongest anatase line, at $2\theta=25.3°$, becomes sharper with increasing the calcination temperature, along the whole samples series, indicating an increase in the mean crystalline size with firing temperature. Crystal size varies from 13 to 64 nm (Table 5.2).

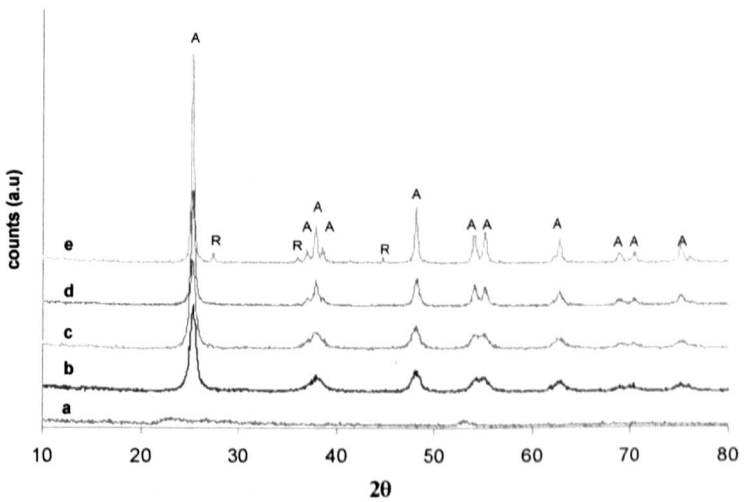

Fig. 5.2. XRD patterns of and calcined samples calcined at different temperatures a) amorphous powder (20 °C); b) TT01 (300 °C); c) TT02 (400 °C); d) TT03 (550 °C); e) TT04 (600 °C).

Table 5. 2. Crystallographic and structural properties of TT series TiO_2.

Sample	Crystallographic Phase [a]	D [b] (nm)	Structural SA [c] (m^2/g)	V_{PORE} [d] (cm^3/g)
TT01	A	13	100	0.480
TT02	A	19	92	0.402
TT03	A	28	53	0.107
TT04	A+R (5%)	64	33	0.172

[a] A=anatase; R=rutile. [b] Diameter calculated from the broadening of the (101) anatase peak using Scherrer's equation. [c] Specific surface area determined using the BET method in the range 0.05<P/P0<0.35. [d] BJH desorption pore volume calculated between 2 and 300 nm.

5.3.1.2 Surface area and Porosity studies

Figure 5.3 shows the N_2 adsorption-desorption isotherms of TiO_2 samples obtained by calcination between 400 and 600 °C. All isotherms are reported on the same volume adsorbed scale for comparison purpose. The correspondent pore size distribution calculated by BJH method from the desorption branch are also reported as insert in each isotherm. All calcined samples present isotherm of Type IV of BDDT classification with two hysteresis loops, indicating a bimodal porosity of the materials in the mesoporous and macroporous regions. Bimodal nature of calcined materials is also confirmed by BJH pore size distribution.

In the isotherm of sample TT01, calcined at 400 °C, two different regions characterised by a condensation step at P/P_0=0.59 and a steeper condensation step at P/P_0=0.84 respectively, can be clearly identified. The isotherm presents two hysteresis loops with different shape. The first hysteresis loop, at $0.6<P/P_0<0.84$, is of type H2 which is usually associated with ink bottle-shaped pores. The second hysteresis, at $0.84<P/P_0<1$, is of type H3 and is associated

with the presence of slit-shaped pores deriving from the aggregation of plate like particles (Section 3.2.2). The isotherm of this sample indicates a very high absorption capacity in correspondence to the macropores regions, which corroborate with sorption data (Table 5.2). The TT01 pore size distribution denotes a narrow distribution in the mesoporous region with a mean pore size of 5.5 nm and wider distribution in the macroporous region with a maximum around 45 nm.

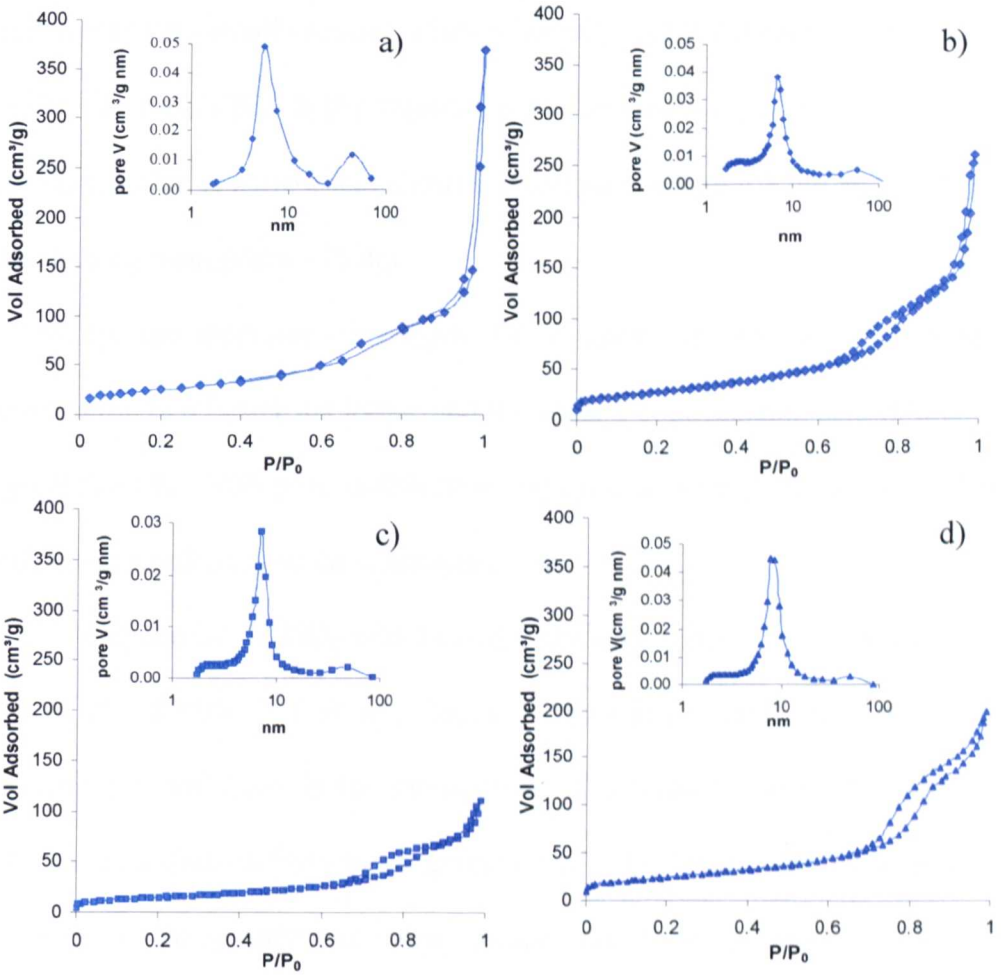

Fig. 5.3. N_2 adsorption-desorption isotherms and pore size distributions of a) TT01; b) TT02; c) TT03; d) TT04. The nm scale in the pore size distribution graphs is logarithmic.

N_2 adsorption-desorption isotherm of TT02 is similar to that of TT01, with the main difference in the maximum volume adsorbed at high partial pressure that denotes a lower absorption capacity for TT02 in the macropore region.

The position of the absorption branches is also slightly shifted towards higher P/P_0 i.e.: 0.65 and 0.87 respectively. The pore size distribution shows a narrow peak at 6.7 nm with a small peak around 56 nm.

Sample TT03, calcined at 550 °C, shows two adsorption steps at P/P0>0.65 and P/P0>0.85, respectively. However the volume adsorbed at high partial pressures is very small showing a low adsorption contribution in the macropore region. In fact, TT03 is the material with the lowest pore volume. The pore size distribution is narrow and shows a mean pore size of 7.2 nm and negligible contribution from pores >10 nm.

Finally, the isotherm of sample TT04, shows a less defined boundary between the two hysteresis loops, and the second condensation step is found at high P/P_0>0,9. TT04 pore distribution indicates a mean pore size of 7.7 nm with also a small peak in the macropores area.

The preparation of TiO_2 with bimodal porosity features have been reported (Yu *et al.*, 2003b, Yu *et al.*, 2007). According with these reports, the adsorption contribution in the mesoporous region arises from intra-aggregate porosity, that derives from the aggregation of TiO_2 crystals with formation of fine pores in the mesoporous range. On the other hand, the contribution in the macroporous region is due to inter-aggregate porosity produced by the aggregation of secondary TiO_2 particles generating interparticle voids of dimensions larger than 50 nm.

5.3.1.3 Morphological studies

The morphology of TiO_2 nanoparticles was analysed by SEM and TEM. TiO_2 calcined at different temperatures show similar particle morphology. SEM micrographs of each TT sample at two different magnifications are reported in Fig. 5.4. Micrographs at higher magnification (on the left) show that the TiO_2 are made up of spherical aggregates quite homogeneous in size and shape. The presence of interparticle voids characterise all samples, with TT03 being the specimen with lower void density.

However, further magnification, shows a more complex organisation of the materials, where the aggregates are formed by the assembly of smaller particles of dimension around 80-100 nm for all samples. Pores between particles are also visible at this level, and the materials appear to become denser with increasing calcinations temperature.

The dimension of the aggregates, also called secondary particle size, has been related to the water concentration used during the hydrolysis process (Maira *et al.*, 2000). For a constant $[H_2O]/[TIP]$ ratio, it was found that in the range $0.25<[H_2O]<0.5$ M the secondary particle size decreased sharply from 900 to 100 nm and kept constant at 80-100 nm for $[H_2O]>0.5$.

The concentration of water for preparation of TiO_2 nanoparticles in this work was kept constant at 6 M with a ratio $[H_2O]/[TIP]=4$. In this condition a secondary particle size of 100 nm was obtained at all calcinations temperatures, confirming Maira's results.

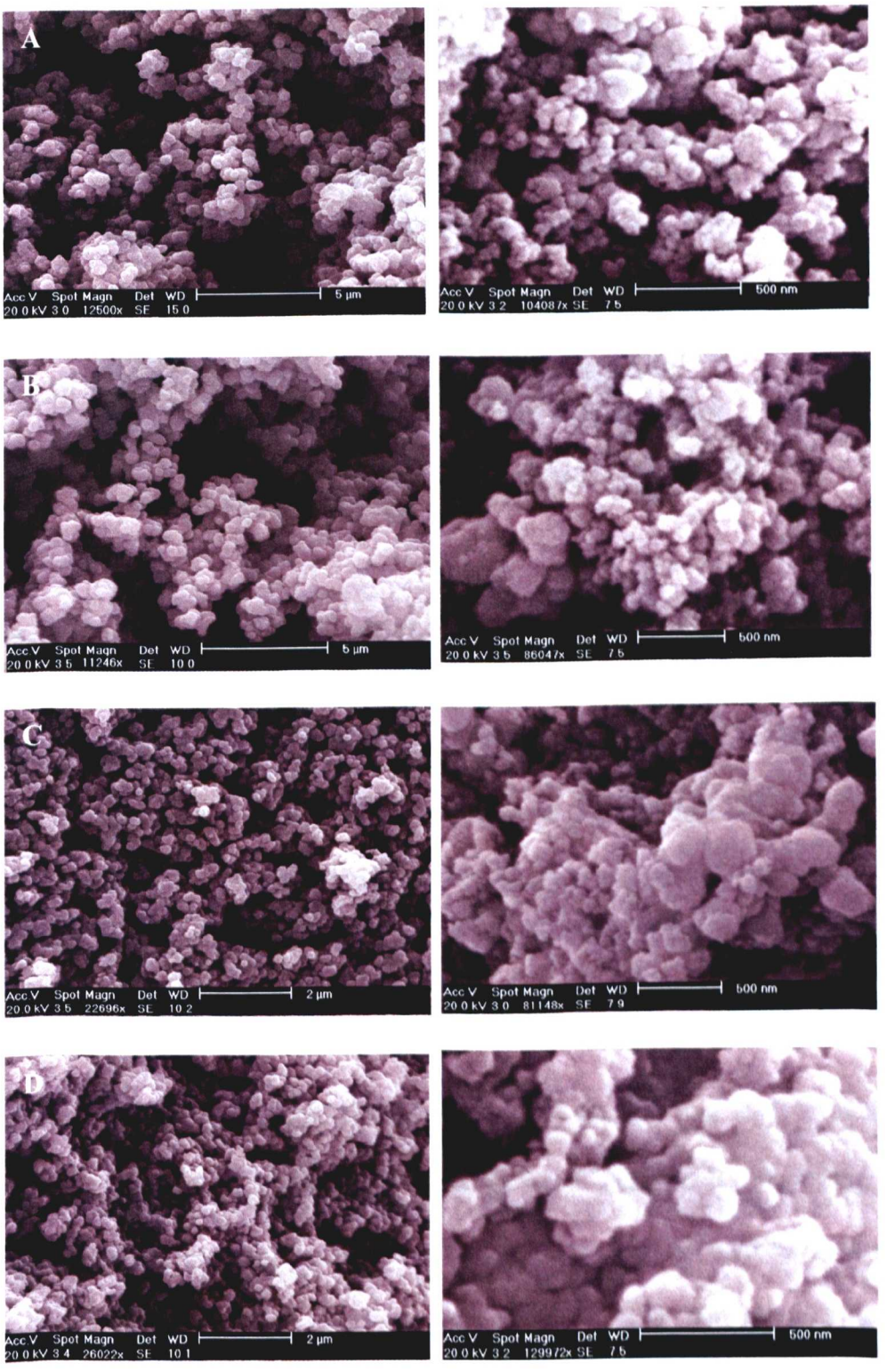

Fig. 5.4. SEM images of TiO_2 nanoparticles at different magnifications: A) TT01 (400 °C); B) TT02 (450 °C); C) TT03 (550 °C); D) TT04 (600°C).

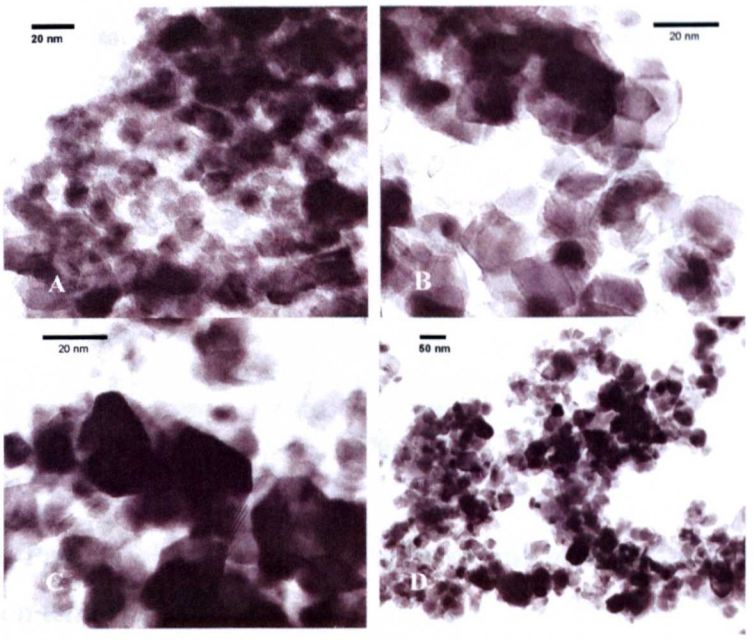

Fig. 5.5. TEM images of TiO_2 nanoparticles: A) TT01 (400 °C); B) TT02 (450 °C); C) TT03 (550 °C); D) TT04 (600°C).

TEM microscopy showing the single crystals are reported in Fig. 5.5. The TiO_2 crystals are well developed and mean crystal size corroborates with that calculated by XRD analysis.

5.3.2 Effect of calcination temperature

The effect of calcination temperature on crystal size and surface area of thermally obtained TiO_2 nanoparticles is shown in Fig. 5.6. By increasing the calcination temperature from 300 to 600 °C, the particle size increases from 13 to 64 nm. The facilitate crystal growth of TiO_2 at high temperatures is the expected behaviour as already reported by other authors (Yu *et al.*, 2003a, Deng *et al.*, 2002, Chen *et al.*, 2008). On the other hand, the surface area of calcined titania considerably decreases with calcination temperature, from 100 to 33 m^2/g.

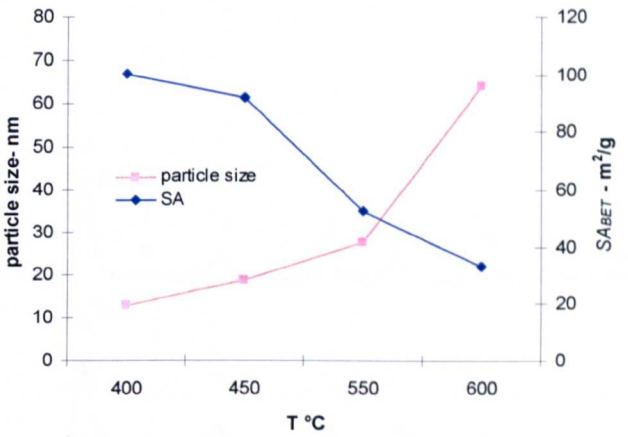

Fig. 5.6. Particle size and surface area of calcined samples as function of calcination temperature.

It is significative to note that catalyst prepared at 600 °C (TT04) shows a surface area almost four times lower than that of the sample calcined at 400 °C (TT01). The calcinations temperature in the range 400-600 °C does not appear to affect the morphology of the crystalline photocatalysts, as shown by SEM micrographs.

5.3.3 Hydrothermal samples (Series HY)

5.3.3.1 X-ray studies

TiO_2 nanoparticles obtained by hydrothermal treatment show the typical anatase diffraction pattern, but also traces of brookite were detectable in all HY samples (Fig. 5.7). In fact, the small peak at $2\theta=30.7°$ corresponds to (121) plane of brookite phase. The presence of brookite also caused a slight shift to higher angle ($2\theta=26°$) of the main anatase peak, due to its overlapping with the (111) brookite peak.

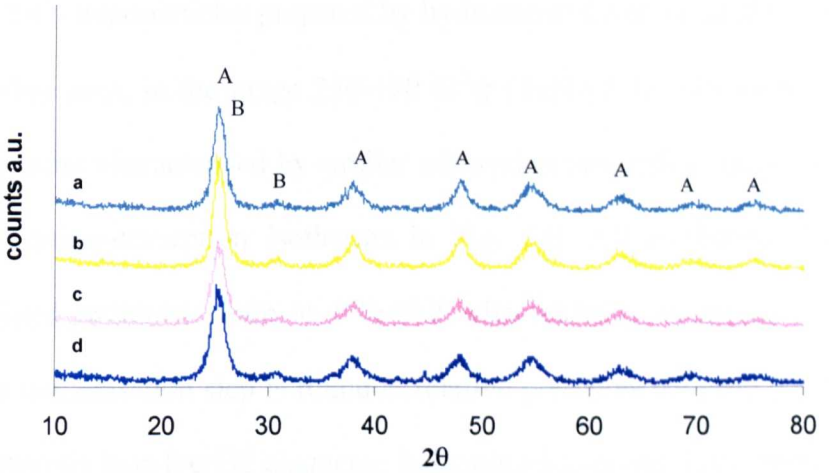

Fig. 5.7. XRD patterns of TiO_2 prepared by hydrothermal method at 150 °C/8h from ethanol/water reaction media with different X_{H_2O} (water molar fractions): a) X_{H_2O}= 0.59; b) X_{H_2O}= 0.74; c) X_{H_2O}= 0.85; d) X_{H_2O}= 0.88.

Table 5.3. Structural and crystallographic properties of hydrothermal samples

Sample	Crystallographic Phase [a]	D [b] (nm)	Structural SA [c] (m^2/g)	V_{PORE} [d] (cm^3/g)
HY01	A+B(t)	5	249.0 ± 1.0	0.375
HY02	A+B(t)	7	213.2 ± 1.2	0.357
HY03	A+B(t)	8	193.6 ± 0.7	0.337
HY04	A+B(t)	11	170.7 ± 0.5	0.316

[a] *A=Anatase; B=Brookite.* [b] *Diameter calculated from the broadening of the (101) anatase peak using Scherrer's equation.* [c] *Specific surface area determined using the BET method in the range 0.05<P/P0<0.35.* [d] *BJH desorption pore volume calculated between 2 and 300 nm.*

Hydrothermal materials show a lower and broader main anatase peak compared with calcined samples, indicating a smaller average crystallite dimension which in fact varies from 5 to 11 nm in the HY series (Table 5.3). Maira and colleagues employed similar hydrothermal treatment of amorphous TiO_2 obtaining particle size between 2.3 and 8.5 nm consisting of pure anatase

5.3.3.2 Surface area and porosity studies

TiO_2 nanoparticles prepared by hydrothermal treatment show high values of surface area, in the range 250-170 m^2/g (Table 5.3). Titania belonging to HY series are characterised by similar adsorption properties, as dispayed by the N_2 adsorption-desorption isotherms in Fig. 5.8. All isotherms display a well-defined hysteresis loop at $P/P_0>0.5$, characteristic of mesoporous materials. The condensation step is found at relative pressures between 0.4 and 0.65. The hysteresis loop has H2 character, indicating ink-bottle shaped pores.

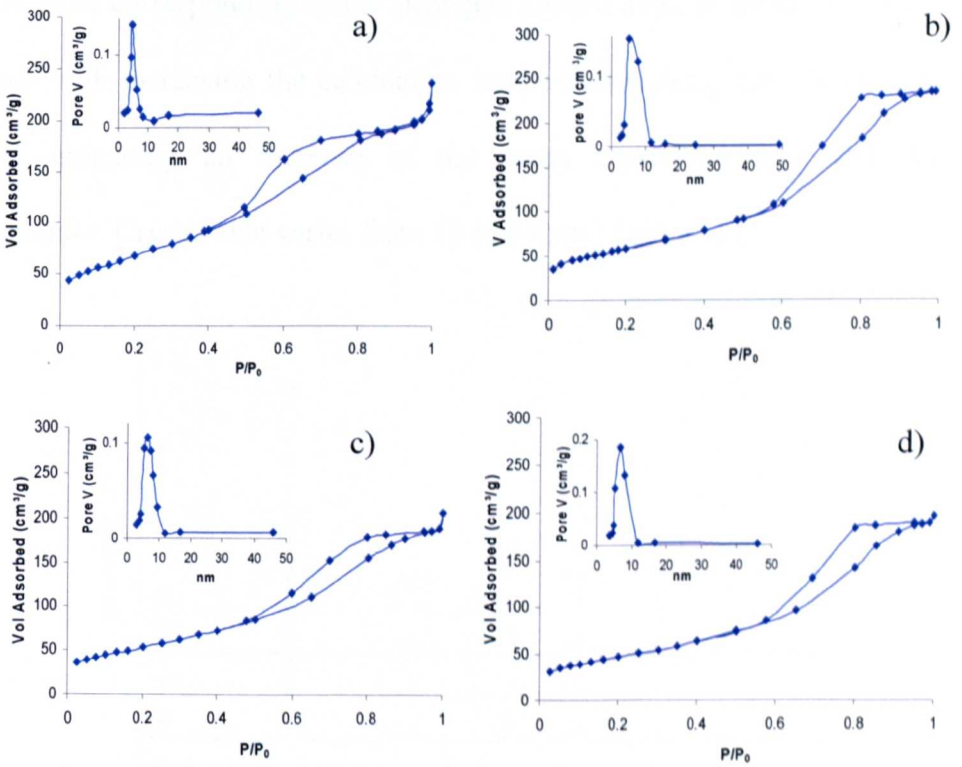

Fig. 5.8. N_2 adsorption desorption isotherms and pore size distributions (insert) of a) HY01 b) HY02 c) HY03 ; d) HY04.

Sample HY01 isotherms presents a bimodal character reporting also a little hysteresis loop of type H2 at high P/P_0 (>0.9). The pore size distribution confirms the HY01 bimodal nature, showing a narrow distribution around a

BRITISH LIBRARY

IMAGING SERVICES NORTH
Boston Spa, Wetherby
West Yorkshire, LS23 7BQ
www.bl.uk

PAGE MISSING IN ORIGINAL

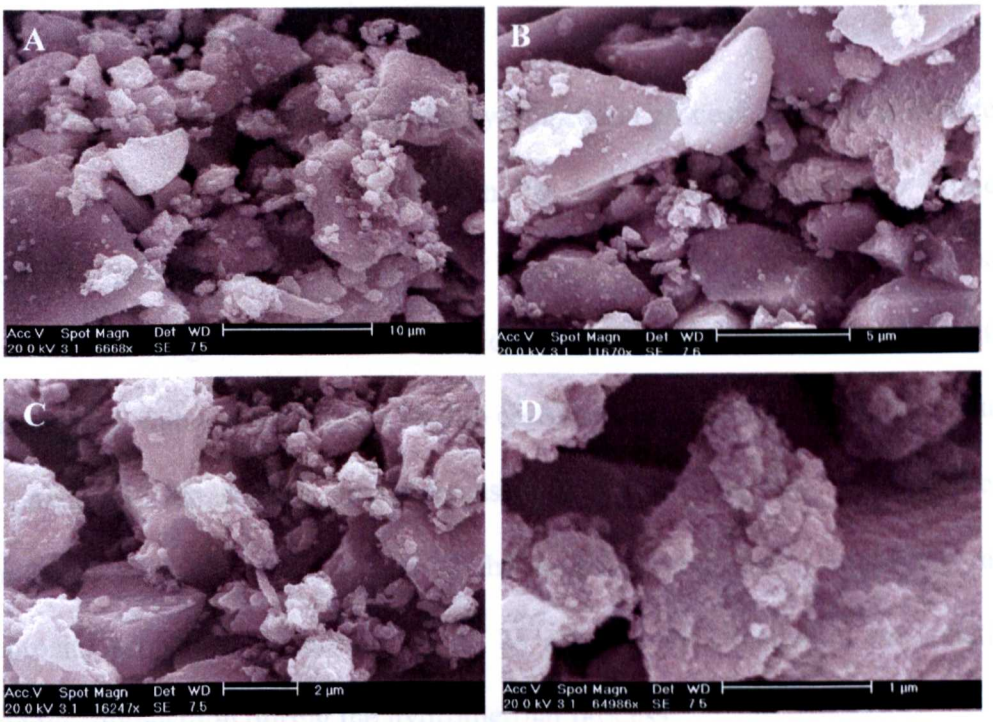

Fig. 5.9. SEM micrographs of HY01. Images correspond to different spot of the sample at different magnifications. Magnification increases from A) to D).

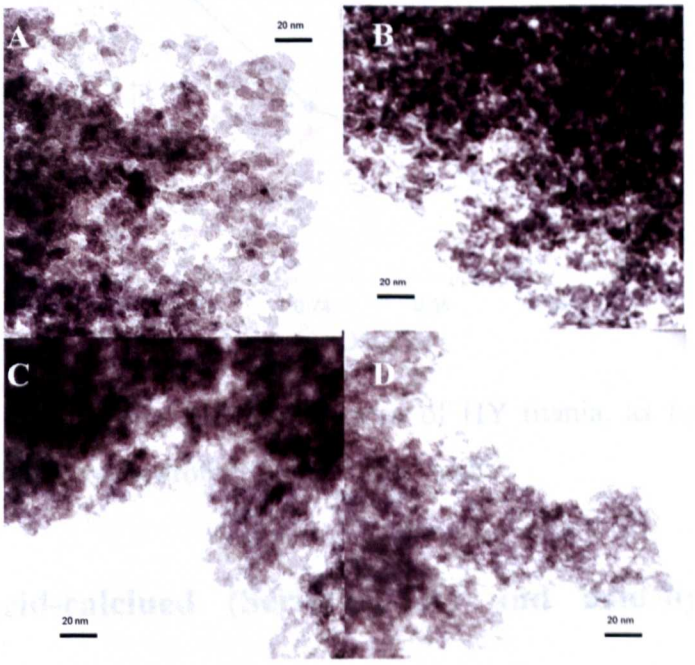

Fig. 5.10. TEM images of TiO_2 nanoparticles prepared by hydrothermal treatment at different water contents, at 150 °C/12 h of amorphous TiO_2 obtained without acidic catalysis A) HY01 X_{H_2O}=0.59 ; B) HY02 X_{H_2O}=0.74; C) HY03 X_{H_2O}=0.85; D) HY04 X_{H_2O}=0.88.

5.3.4 Effect of water content

Different H_2O content during the hydrothermal process give rise to different crystallite sizes. The trend is shown in Fig. 5.11: increasing the water content leads to larger crystals. Tuning water content from X=0.59 to X=0.89 crystal size in the range 5-11 nm has been obtained. It is worth noticing that little increase in water concentration lead to considerable growth of the TiO_2 crystal. Conversely, the surface area decreases with increasing the water content, probably as direct consequence of the larger crystal size. Morphology and porosity properties do not appear to be effected by changes in the reaction media composition during the hydrothermal process.

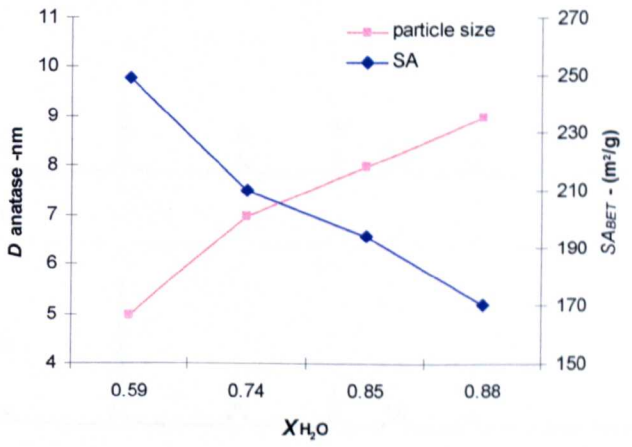

Fig. 5.11. Particle size and surface area of HY titania, as function of H_2O molar fraction in the hydrothermal reaction media.

5.4 Acid-calcined (Series TTA) and acid-hydrothermal samples (Series HYA)

5.4.1 X-Ray studies

TiO_2 samples belonging to series TTA consist of pure anatase as shown in Fig. 5.12, no rutile or brookite diffraction peaks were detected. The type of

acid used during hydrolysis-condensation does not affect the crystalline size as TiO_2 treated at the same temperature have similar crystal size indifferently on the acid used. These crystal sizes are in good agreement with those of samples prepared with no acid (series TT) calcined at the same temperature indicating that the principal parameter in crystal growth is the calcination temperature.

Amorphous material obtained by sol-gel in acidic conditions by HCl and acetic acid respectively, were treated hydrothermally in a mixture water:ethanol 1:1 at 150 °C for 8 hours obtaining sample belonging to series HYA. X-ray diffraction analysis of HYA samples shows the presence of anatase with traces of brookite (Fig. 5.13).

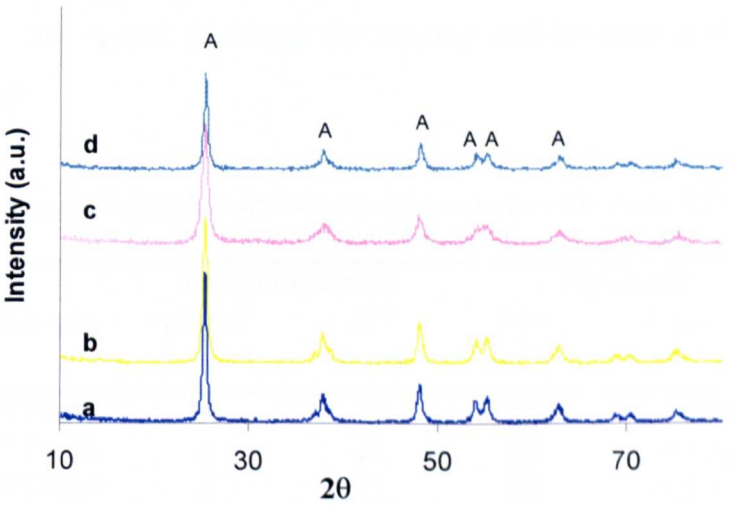

Fig. 5.12. XRD patterns of TiO_2 prepared by sol-gel in acidic condition followed by calcination: a) Ac.ac/550 C; b) HCl/550 C; c) Ac.ac/400 C; d) HCl/400 C. A denotes the anatase diffraction peaks.

The formation of brookite in traces during hydrothermal treatment of amorphous TiO_2 in presence of HCl has been reported in literature (Reyes-Coronado *et al.*, 2008).

The main characterisation parameters of titania obtained under acidic conditions are summarised in Table 5.4.

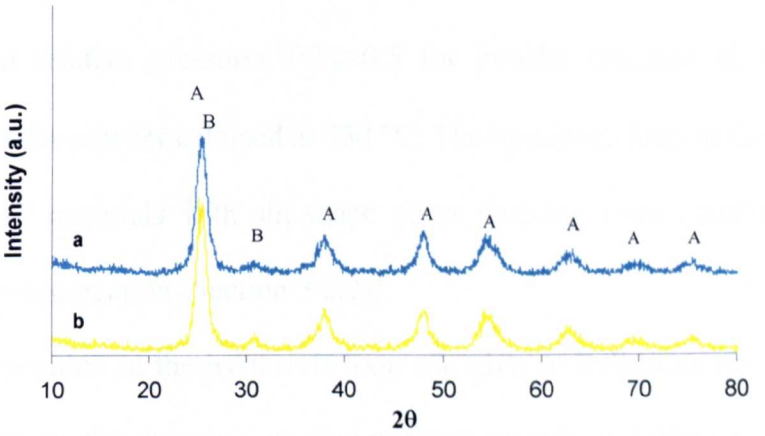

Fig. 5.13. XRD patterns of TiO_2 prepared by sol-gel at acidic conditions by a) Acetic acid and b) HCl and treated hydrothermically in a mixture H_2O/ethanol at 150 °C /8h. A and B denote the anatase and brookite diffraction peaks respectively.

Table 5.4. Crystallographic and structural properties of series TTA and HYA

sample	crystallographic phase [a]	D [b] (nm)	Structural SA [c] (m^2/g)	V_{PORE} [d] (cm^3/g)
TTA01	A	27	32	0.200
TTA02	A	15	88	0.130
TTA03	A	25	22	0.146
TTA04	A	13	30	0.059
HYA01	A+B (t)	6	247	0.384
HYA02	A+B (t)	6	242	0.423

[a] *A=Anatase; B= Brookite;* [b]*Diameter calculated from the broadening of the (101) anatase peak using Scherrer's equation.* [c] *Specific surface area determined using the BET method in the range 0.05<P/P0<0.35.* [d] *BJH desorption pore volume calculated between 2 and 300 nm*

5.4.2 Surface area and Porosity studies

The absorption properties of the TiO_2 sample belonging to TTA and to HYA series are reported in Fig. 5.14A and 5.14B respectively. All calcined

samples prepared under acidic conditions present similar isotherm shape with a narrow hysteresis loop of type H3. The samples hydrolysed by acetic acid present hysteresis at $P/P_0>0.7$ while for samples hydrolysed by HCl the loop is found at relative pressures $P/P_0>0.5$ for powder calcined at 400 °C and $P/P_0>0.8$ for powder calcined at 550 °C. The hysteresis loop of these samples is typical of materials with slit-shape pores deriving from platelike secondary particles aggregation (Section 3.2.2).

The position of the hysteresis loop can give an indication about the size of the pores in the samples, as larger pores absorb at higher values of P/P_0. However, it was not possible to obtain a pore distribution by BJH method for these specimens. Sample TTA04 exhibits sensibly lower adsorption capacity than other samples, which corroborate adsorption data (see Table 5.4)

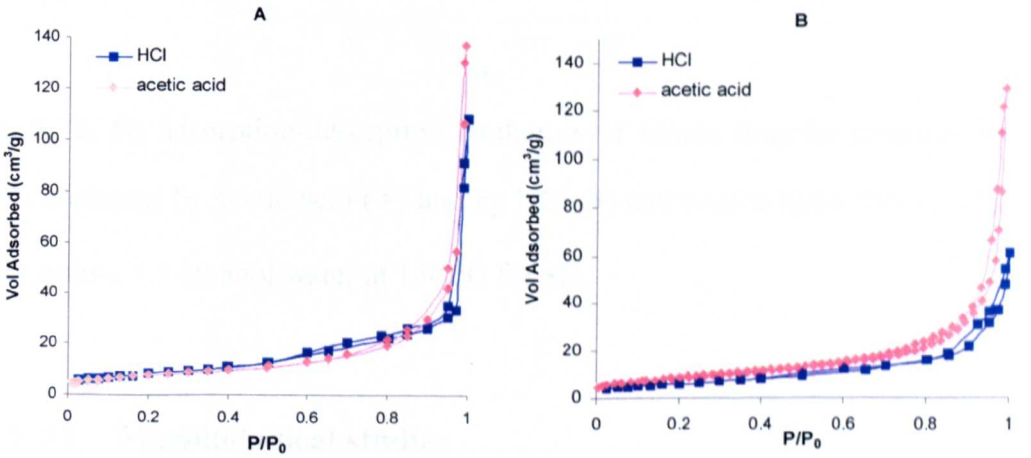

Fig. 5.14. N_2 adsorption-desorption isotherms of TiO_2 samples prepared in acid conditions by acetic acid (♦) and by HCl (■) and calcined at A) 400 °C and B) 550 °C.

N_2 adsorption-desorption isotherms of samples HYA01 and HYA02 are clearly of type IV with H2 hysteresis loop at $P/P_0>0.4$, and a small contribution

in macroporous region at P/P_0 approaching 1. From the shape of the hysteresis loop, an ink-bottle pore type can be predicted. The two hysotherms almost overlap, thus in Fig. 5.15 they are plot at different scales. The hydrothermal treatment at consistent experimental conditions of TiO_2 obtained by hydrolysis-condensation in non-acidic and acidic conditions yields to crystalline materials with similar adsorption features. Also, the type of acid used during the hydrolysis step does not affect the adsorption-desorption properties of the hydrothermal samples.

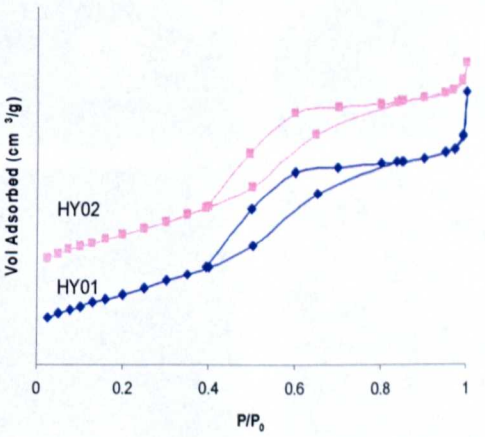

Fig. 5.15. N_2 adsorption-desorption isotherms of titania samples prepared in acid conditions by acetic acid (♦) and by HCl (■) and treated hydrothermically in a mixture 1:1 ethanol/water at 150 °C for 8h.

5.4.3 Morphological studies

SEM micrograph reported in Fig. 5.16 show the differences between titania obtained with HCl and acetic acid as hydrolysis catalysts. In case of utilisation of acetic acid, the catalyst appears made up of big spherical aggregates with dimension in the range 300-500 nm.

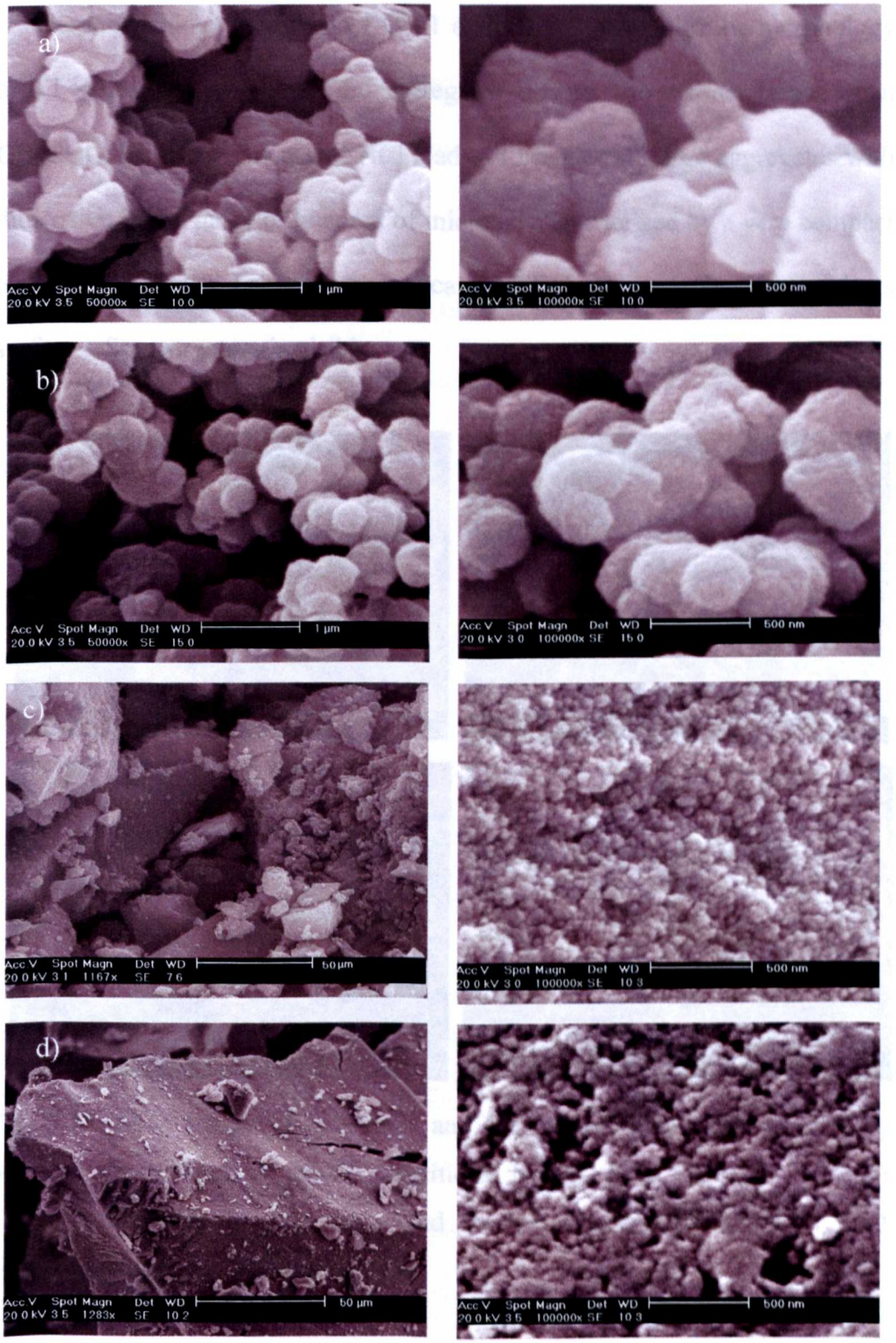

Fig. 5.16. SEM images at low (left) and high (right) magnification of TiO_2 prepared by sol-gel at acidic conditions followed by calcination: a) TTA01 (CH_3COOH-400 °C); b) TTA02 (CH_3COOH-550 °C); c) TTA03 (HCl-400 °C); d) TTA04 (HCl-550°C).

The morphology of catalyst TTA01 and TTA02 resembles the morphology of TT series, but the size of the aggregates is from 3 to 5 times larger when CH_3COOH is used. The use of HCl lead to formation of large aggregates with dimension in the range of hundred of microns, characterised by a very compact texture. As shown by high magnification SEM micrographs, on catalysts surface a finer structure is visible.

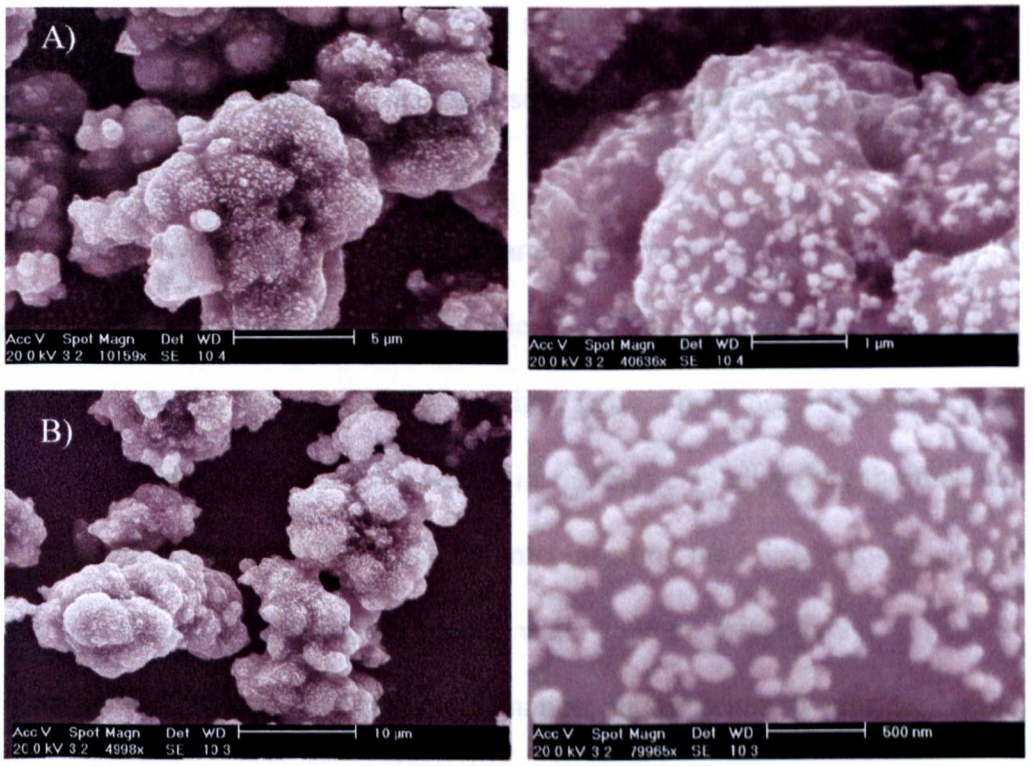

Fig. 5.17. SEM images at low (left) and high (right) magnification of TiO_2 prepared by sol-gel at acidic conditions by A) HCl (HYA01) and B) CH_3COOH (HYA02) and crystallised by hydrothermal treatment in H_2O /ethanol 1:1 at 150 °C/8h.

TTA03 shows a well-defined homogeneous structure made up of small particles, while in case of TTA04 the surface appears less defined and more compacted Titania samples belonging to series HYA show a peculiar morphology (Fig. 5.17). The samples are made up of 5-10 µm aggregates of

irregular shape. The dimension of samples hydrolysed by HCl and by acetic acid show comparable dimension. High magnification micrographs show that the surface of the aggregates appears smooth and covered by small particles of 100-200 nm dimension

5.4.4 Effect of acidic catalysis during sol-gel

The addition of acid during the hydrolysis-condensation step of the TiO_2 preparation yield to TiO_2 materials with significant differences compared with materials prepared under uncatalysed sol-gel step and crystallised at same conditions.

Since the hydrolysis-condensation carried out under acidic catalysis yields to titania with crystal size comparable to titania obtained without acidic catalysts, it can be assumed that the acidic catalysis does not affect the crystal dimension. This evidence was observed in samples crystallised by thermal and hydrothermal treatments, where the parameter setting the crystal growth appear to be the calcination temperature and the water content, respectively.

In the case of TiO_2 crystallised by calcination, the presence of acid during the hydrolysis-condensation step yield to TiO_2 with different surface areas despite the similar crystal size. In general a reduction of the surface area was found for calcined samples prepared in an acidic environment. The surface area reduction was found to be more pronounced when HCl was used as catalyst. In the case of hydrothermally crystallised samples, the use of acid during sol-gel preparation step does not influence the surface area of the obtained TiO_2.

The addition of acid during the sol-gel step appears to have an important impact on the catalyst morphology as demonstrated by the microscopy studies.

Relevant differences in terms of shape and dimension of TiO_2 particles have been experienced depending on the presence and nature of the acid used for samples crystallised by thermal and hydrothermal processes.

The hydrolysis-condensation carried out under acidic catalysis modifies also the quality and distribution of the pores in the crystallised TiO_2. With regard to calcined materials, the defined bimodal distribution characteristic of TiO_2 belonging on series TT is not present in samples prepared by acidic hydrolysis TTA. A comparison of the hysteresis pattern suggests also a different shape of the pores, which in series TTA are predominantly slit-like deriving from secondary particles aggregation. It is interesting to note that by changing the sol-gel conditions at constant crystallisation conditions it was possible to obtain TiO_2 with similar crystal size, modulating the surface area by changing porosity and morphological properties.

5.4.5 Photocatalytic activity

5.4.5.1 Studies on P-25

Commercial photocatalyst P-25 has been widely used to assess the efficiency of photocatalytic reaction for decomposition and mineralization of organics in both water and gaseous phases. For this reason, it was chosen as standard reference for this work, since its effectiveness has been proved by several authors in the photodegradation of TCE (Jacoby *et al.*, 1994, Lim and Kim, 2004, Ou and Lo, 2007, Maira *et al.*, 2000). The first part of the evaluation of the photocatalyst activity focused on the evaluation of P-25 and on the effect that some experimental parameters have on the conversion of TCE in our experimental setup. All experiments were conducted using a total

flow rate of 0.04 L s^{-1} at which the reaction-controlled regime is guaranteed (Salvado-Estivill, 2007).

No TCE conversion was experienced in absence of catalyst or in absence of UVA illumination, thus any conversion during the experiments can be ascribed to the photo-oxidation of TCE on TiO_2 surface.

5.4.5.1.1 Effect of light intensity

The reaction rate of 68.5±1.0 μM TCE inlet with 8% RH was determined at different UVA incident light intensities in the range 3.0-41.3 W/m^2. The TCE reaction rate increases with the light intensity, as shown in Fig. 5.18.

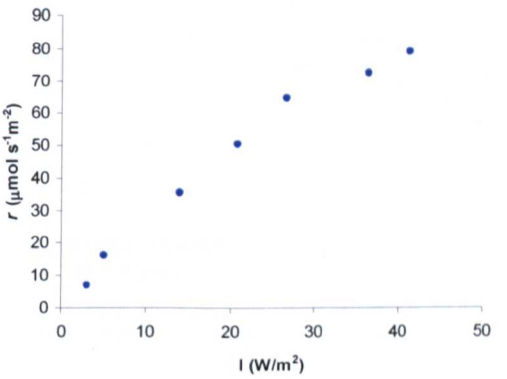

Fig. 5.18. Effect of UVA incident light intensity (343-380 nm with maximum irradiation peak at 365 nm) on the photo-oxidation rate of 68.5±1.0 μM TCE. (8% RH ; flow rate of 0.04 L/s).

The correlation between reaction rate and incident light intensity follows a power law $r = k \cdot I^{\alpha}$ (Section 2.2.10.1). The data linearization through a log-log plot is reported in Fig. 5.19 and allows to identify two distinct intensity regions, where the correlation between the reaction rate and the light intensity is of different order. For light intensities up to about 20 W/m^2 the correlation is of first order (α=0.97), while in the range 20-41 W/m^2 a 0.61 order is found. In

the latter intensity range, the charge carrier recombination dominates the process at the catalyst surface, giving rise to approximately half order dependence. On the base of these results it is possible to set the intensity threshold where the transition from first order to half order occurs at around 20 W/m^2 at our experimental conditions.

By using a packed-bed reactor with P-25 immobilised on glass beads, Wang *et al* found 0.61 order of the light intensity in the range 1-4.5 W/m^2 for the photo-oxidation of TCE under 365 nm UV light (Wang, 1997).

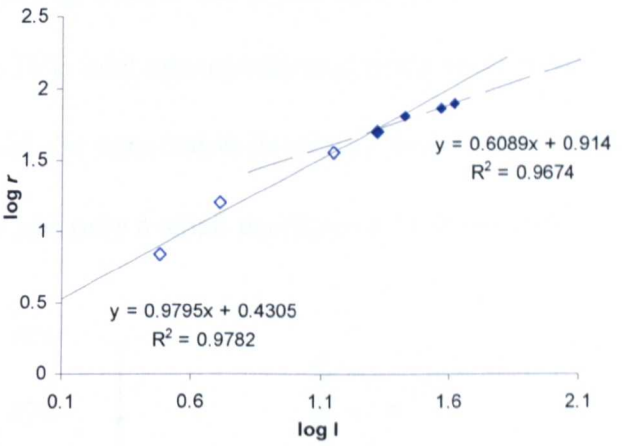

Fig. 5.19. Linearization of reaction rate as function of UVA incident light intensity (343-380 nm with maximum irradiation peak at 365 nm) on the photo-oxidation rate of 68.5±1.0 μM TCE. (8% RH; flow rate of 0.04 L/s). Empty diamonds indicate first order light intensity range and filled diamonds denote 0.6 order intensity region.

Kim and Hong found a first order correlation between TCE reaction rate and light intensity at 352 nm below 15 W/m^2 in a batch photo reactor (Kim and Hong, 2002)

5.4.5.1.2 Effect of TCE initial concentration

The effect of TCE inlet concentration on TCE conversion at fixed experimental conditions was investigated. The TCE initial concentration in the gas feed was varied from 4.4 to 49.9 μM (correspondent to 100 and 1200 ppm). The other experimental condition were: RH=8%, light intensity=10 W/m^2 obtained by irradiating the catalyst surface by using 3 lamps at 10 cm distance from catalysts surface. The photocatalytic plate was a 75 cm^2 glass plate coated with a catalyst loading of 6 mg/cm^2.

As shown in Fig. 5.20 it was found that the TCE conversion decreases with increasing the TCE inlet concentration at fixed experimental parameters. From 4 μM to 29 μM the conversion decreased from 19% to 4%. At concentration higher than 29 μM only a small decrease in TCE conversion was observed.

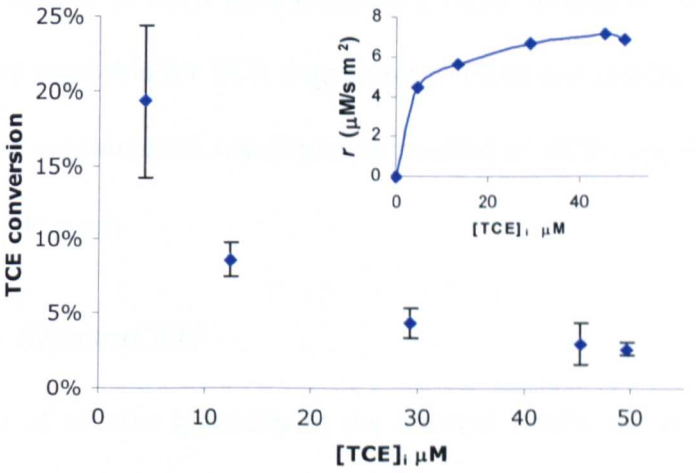

Fig. 5.20. Effect of inlet TCE concentration on TCE conversion and TCE reaction rate (insert). Experiments were carried out at 8% RH, UVA incident light intensity (343-380 nm with maximum irradiation peak at 365 nm) I=10 W/m^2.

The insert in Fig. 5.20, reports a plot of TCE reaction rate vs. TCE inlet concentration. This graph clearly indicates a saturation of the adsorption or "active" adsorption sites on the catalysts surface with increasing TCE concentration and agrees with previous reports from other authors. Lim and Kim (2004) found that the gas phase photodegradation of TCE on Degussa P-25 decreases linearly with increasing the initial TCE concentration in the range 100-500 ppm in an annulus fluidised bed photoreactor. The same trend was also found in a flat plate photoreactor by Demeestere and coworkers (2004). Since the photocatalytic process is a surface process, it is always valid the assumption that only adsorbed pollutant can undergo photodegradation. However, due to the electron-hole recombination process, not all adsorption sites at the surface will be reached by the h^+ that initiate the process. Since the photocatalytic and recombination competition depends on the photon flux at the catalyst surface, at fixed light intensity a fixed number of 'active" sites at the surface are available for TCE degradation. From our results, the saturation of P-25 at our experimental conditions is reached at TCE concentration of 30 μM (around 700 ppm).

5.4.5.1.3 Effect of RH

The effect of relative humidity in the interval 1-65% on TCE conversion was investigated and the obtained results are reported in Fig. 4.20. TCE initial concentration was 34.5±1.0 μM, UVA incident light intensity was I=24.36 W/m^2.

Increasing the relative humidity from 1 to 4% there is an increase in the TCE conversion. Water is easily adsorbed on TiO_2 surface, where it can act as

h^+ trapping site, with generation of OH·radicals and consequent increase of TCE conversion. However, at RH>4% a decrease in the TCE conversion is observed. Water adsorption is in competition with TCE adsorption at the catalyst surface. It is believed that at RH>4%, some catalyst active sites are occupied by water molecule, thus are not available for TCE adsorption and degradation.

This result agree with previous reported studies. Wang *et al* reported a decrease of TCE degradation rate with increasing the humidity in the gasflow from 230 to 30000 ppm using a packed-bed reactor with P-25 coated on glass beads under 365 nm UV light (Wang, 1997).

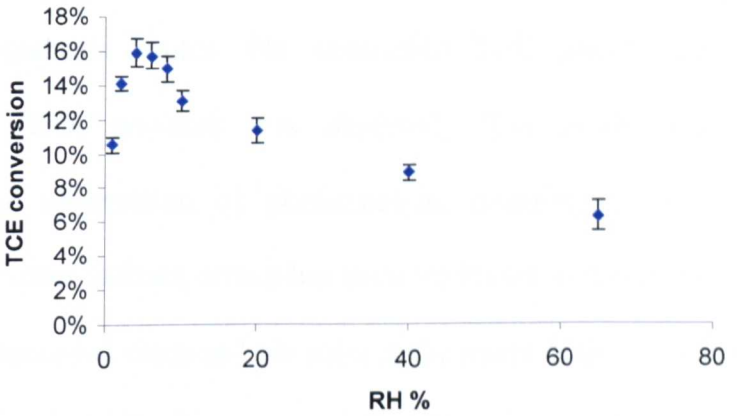

Fig. 5.21. Effect of Relative humidity on 34.5±1.0 μM TCE conversion on P-25. UVA incident light intensity (343-380 nm with maximum irradiation peak at 365 nm) I=24.36 W/m^2.

5.5 Calcined (Series TT) and hydrothermal samples (Series HY)

The photocatalytic activity of TiO_2 nanoparticles belonging to series TT and HY have been evaluated for the photooxidation of TCE in gas phase using the

gas phase reactor in its final configuration (section 3.2.10.4). All experiments were conducted using a total flow rate of 0.04 L s^{-1} at which the reaction-controlled regime is guaranteed (Salvado-Estivill, 2007); TCE inlet concentration was 35±2 μM (870±30 ppmv) and applying three different light intensities (343-380 nm with maximum irradiation peak at 365 nm) at the catalyst surface: 11.2, 28.6, 41.2 W/m^2 respectively.

Preliminary experiments carried out in absence of catalyst or in absence of UV illumination show no variation in the TCE concentration, thus the TCE conversion during the catalyst evaluation can be ascribed to the photocatalytic oxidation of TCE on the TiO_2 surface.

The first samples tested were the amorphous TiO_2 obtained with the three different synthesis routes. No detectable TCE photo-oxidation on the amorphous TiO_2 powders was observed. This result corroborate with experimental observation of photocatalytic inactivity of amorphous TiO_2 reported by other authors, which has been attributed to the high recombination rate of photoexcited electron-hole pairs at the many defects sites present at the surface and in the bulk of amorphous TiO_2 (Ohtani *et al.*, 1997).

Crystallined samples were then tested. Figure 5.22 reports and compares the TCE conversion percentage obtained at the three different light intensities investigated, on TT and HY samples and includes also the behavior of commercial catalyst P-25 evaluated in the same experimental conditions. All crystallined samples show some photocatalytic activity for TCE degradation in the gas-phase, and some of the specimens show considerably higher photoactivity than P-25.

Every sample was tested at light intensity in the range 11.2 to 41.2 W/m^2. In this range, for Degussa P-25, the dependence between reaction rate and light intensity changes from first to 0.6 order at around 20 W/m^2, as reported in section 4.4.5.1.1. For the other TiO_2 samples the correlation between reaction rate and light intensity is of half order, as reported in Table 5.5.

Hydrothermally prepared samples show low TCE reaction rate under the whole light intensity range investigated, despite the very high surface area. The TCE reaction rate increases with increasing crystallite size, from sample HY01 to sample HY04. The most obvious outcome from Fig. 5.22 is that samples belonging to series TT, crystallised by thermal treatment, perform much better than samples belonging to series HY, which were prepared by hydrothermal treatment.

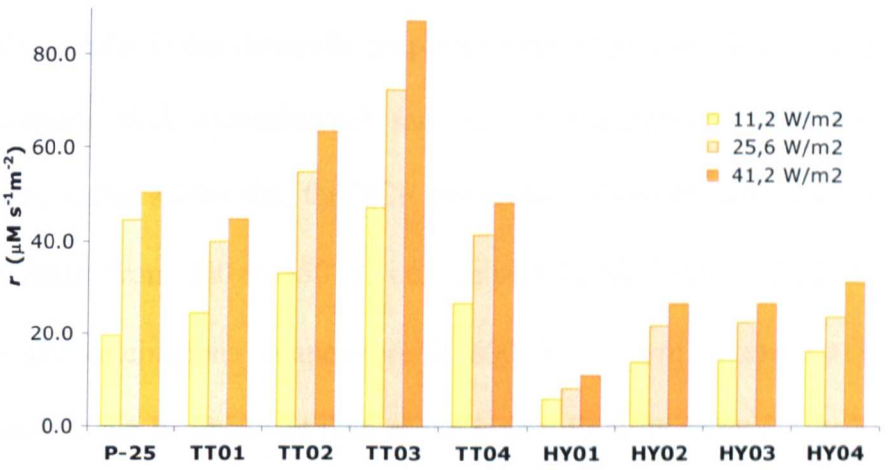

Fig. 5.22. TCE degradation rates of TiO_2 photocatalyst: comparison between P-25 and TiO_2 prepared by sol-gel without acid, followed by calcination (TT samples) or hydrothermal treatment (HY sampes). Initial TCE concentration was 35±2 μM (870±30 ppmv), 8% RH. Reaction rates are per unity surface area of irradiated support.

Table 5.5. Effect of light intensity on TCE reaction rate on TiO_2 nanoparticles belonging to series TT and HY. Values of α and correlation coefficient R.

Sample	α	R	Sample	α	R
TT01	0.52±0.09	0.9945	**HY01**	0.51±0.04	0.9954
TT02	0.52±0.08	0.9974	**HY02**	0.53±0.04	0.9914
TT03	0.50±0.04	0.9890	**HY03**	0.51±0.06	0.9889
TT04	0.49±0.03	0.9973	**HY04**	0.53±0.03	0.9979

This photoactivity improvement can be correlated with the water content during the hydrothermal process: the higher the water content during the hydrothermal process, the higher is the photoactivity of obtained catalyst. Very little difference in the photoactivity of sampes HY02 and HY03 is observed, compatibly with the minor difference in the mean crystallite size which were estimated 7 and 8 nm respectively (from XRD pattern). If compared with the photoactivity of P-25, HY samples performances are much lower in the whole intensity range investigated.

All samples in the thermally prepared series show considerably higher TCE conversions than hydrothermal samples. A comparison made among the calcined series shows that the TCE conversion increases with the calcination temperature from 400 to 550 °C i.e. samples TT01, TT02 and TT03; to drop when the calcinations temperature is 600 °C in case of sample TT04. In addition, it can be observed that, at the lowest light intensity (11.2 W/m^2), all thermal samples show higher activity than P-25. At higher light intensities, 25.6 and 41.2 W/m^2, catalysts TT01 shows lower conversions than P-25, while TT04 shows photoactivity comparable with that performed by P-25. Samples TT02 and TT03 present enhanced photocatalytic activity with respect to P-25 in the entire light intensity range considered in this study. The best performing catalyst is TT03 which shows a TCE conversion 2.5 times higher than P-25 at

the lowest light intensity and almost double conversion at the highest light intensity.

XPS analysis was performed on all samples belonging to the series TT in order to investigate the possible differences in surface composition or the existence of impurities at the catalyst surface that could influence the photocatalytic behaviour. Fig. 5.23A reports the XPS survey spectra of sample TT01 with peak assignation. The other samples present similar features. Photoelectron peaks for Ti and O were recorded at typical TiO_2 binding energy. Also C at 284.8 eV was clearly detectable as surface impurity in all samples, which can derive from the incomplete decomposition of the carbon in the starting material and from air absorbents.

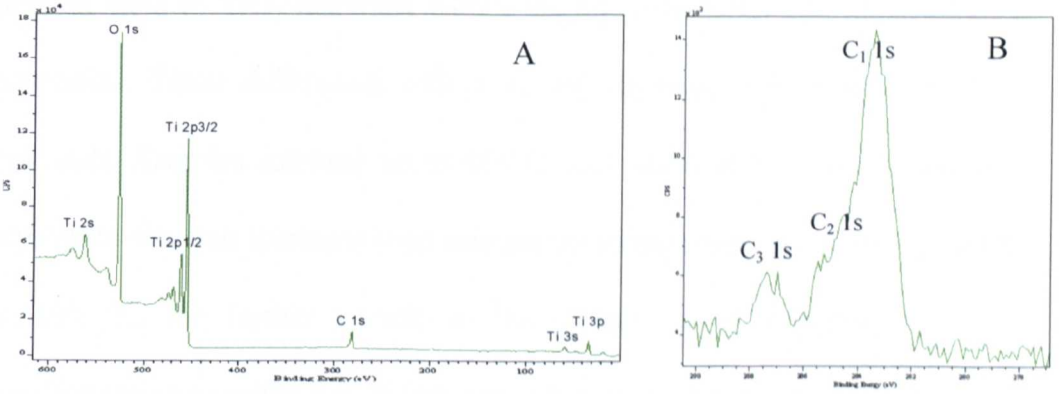

Fig. 5.23. A: representative XPS survey spectra of TiO_2 nanoparticles obtained by calcination. B: detail of C 1s signal.

Table 5. 6. Atomic composition (A) and C peak composition (B) of P-25 and TiO_2 nanoparticles obtained by calcination as obtained by XPS analysis.

A	% atomic composition		
	O 1s	Ti 2p	C 1s
TT01	67.06	26.20	6.74
TT02	66.24	26.45	7.30
TT03	66.61	25.88	4.50
TT04	66.07	26.06	7.87
P-25	66.27	25.68	8.08

B	C 1s component %		
	CHx	COH	C=O
TT01	56.30	27.60	16.10
TT02	62.75	23.47	13.78
TT03	62.52	24.99	12.49
TT04	63.33	20.56	16.12
P-25	63.96	21.33	14.71

High resolution spectra of C 1s (Fig. 5.23B) reveals that the signal is composed by three components: adventitious hydrocarbon species (283.4 eV), hydroxyl groups C–OH visible as shoulder of main peak at 288 eV and a small peak 287.3 eV attributable to carbonyl groups. The composition % of the C 1s signal is reported in Table 5.6. Atomic composition and Carbon presence is low in all samples (<8%) and sample TT03 shows the lowest carbon content. However, the differences in C content at the catalysts surfaces were not found significant in order to explain the considerable difference in photocatalytic activity exhibited by the photocatalysts analyzed.

As discussed in the previous section, the crystallisation methods employed in the preparation of the photocatalysts, i.e. calcinations and hydrothermal process yield to TiO_2 materials with a variety of physical and morphological properties. These differences reflect on the photocatalytic properties of the materials. Samples calcined up to 550 °C are made up of pure anatase with crystallite size that increases with calcination temperature. In samples prepared at 600 °C, the further growth of the crystals is accompanied by phase transformation to rutile. Fig. 5.24A and 5.24B report the trend observed for the TCE photo-oxidation rate as function of anatase particle size and as function of surface area respectively, considering both HY and TT series catalysts. These reaction rates are those obtained by applying a light intensity of 11.2 W/m^2 and matching trends were found for the other irradiation conditions.

The photocatalytic activity can be clearly correlated with the crystal size of the anatase phase in the samples, which increases with the calcination temperature. The reaction rate increases monotonically with increasing crystallite size of TiO_2 until an optimum value of 28 nm that corresponds to

sample TT03, calcined at 550 °C. Considering the reaction rate as function of surface area, it can be seen that by increasing the SA, after an initial increase of activity up to 53 m^2/g (catalyst TT03), a constant decrease in the reaction rate is observed.

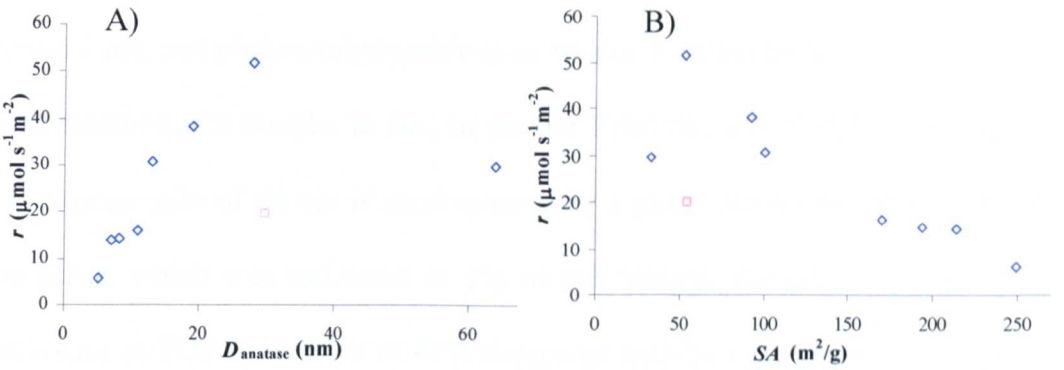

Fig. 5.24. TCE degradation rates of TiO_2 photocatalyst as function of crystal size (A) and surface area (B). Empty diamonds denote TT and HY TiO_2 nanoparticles, and square denotes Degussa P-25. Reaction rates are per unity surface area of irradiated support (RH=8%, light I=11.2 W/m^2).

TiO_2 with large crystal size are characterised by low surface recombination rates (Zhang *et al.*, 1998) and, generally, longer charge-carriers lifetime as the photoexcited e^-/h^+ pairs must migrate longer distances to reach the surface in large crystals than in small crystals (Jung *et al.*, 2002). The e^-/h^+ pairs migration can take place successfully in well-developed and highly crystalline particles with low level of recombination centre i.e. crystal defects. For this reasons the electron density at the catalyst surface is higher in large titania with high crystallinity (Jung *et al.*, 2002). The interfacial charge transfer at the catalyst surface is proportional to the surface charge density. Therefore, titania with high crystallinity show faster interfacial charge transfer rate with

increasing particle size. The trend of photocatalytic activity with crystallite size indicates a high crystallinity of titania calcined samples and an increase the interfacial charge transfer rate from catalyst surface to adsorbed species with increasing crystal size.

However, it is important to notice that the linear relationship between crystal size and photocatalytic activity of titania is observed as long as rutile is not present in the sample. In fact, in sample TT04 the growth of TiO_2 crystal to an average size of 64 nm is accompanied by a phase conversion from anatase to rutile, which was estimated in 5% in this sample. Sample TT04 shows a decrease in TCE conversion of 40% compared with best sample TT03. Despite this reduction its photoactivity is still higher than reference sample P-25. This result suggest that pure anatase titania with high crystallinity lead to higher photoactivity than rutile-anatase mixed phase photocatalysts and corroborates with findings from other authors (Kuo-Hua Wang *et al.*, 1998, Jung *et al.*, 2002, Zhang *et al.*, 1998).

At this point it is interesting to compare our highly active photocatalysts with Degussa P-25. In this respect, it is worth noticing that the best performing catalyst shows a crystal size and surface area that are comparable with those of Degussa P-25. Thus, the difference in activity and the enhanced activity of TT03, and also of the other specimens belonging to TT series compared with Degussa P-25, cannot be explained in terms of a crystal size effect on the charge transfer rate.

The main difference between the thermal samples and the commercial P-25 concern the crystallographic composition being P-25 made of 75% anatase, 25% rutile while thermal samples consist of pure anatase apart of sample TT04

with 5% of rutile content. However, a consistent evaluation of the role of crystalline phase was not possible using these samples as only one specimen contains rutile and in a very small amount. The analysis and comparison of an analogous series of samples with titania richer in rutile is presented in a following section of this chapter.

Another distinctive property of TT samples concerns the porosity, as P-25 is a non-porous material while thermal samples shows significant mesoporosity as well as a macroporous contribution. The porosity features of the calcined sample can play a role in increasing the photocatalytic activity, allowing a higher adsorption and diffusion of reactive species at the catalyst surface compared with the non-porous P-25 material.

5.6 Acid-calcined (Series TTA) and acid-hydrothermal samples (Series HYA)

The photocatalytic properties of TiO_2 samples prepared by hydrolysis-condensation in acidic condition by either acetic acid and HCl and calcined at 400 and 550 °C (series TTA) or treated hydrothermically at 150 °C for 8 hours in a mixture H_2O/Ethanol with X_{H_2O}=0.59 (series HYA) are reported in this section. The experimental conditions for the evaluation of the photocatalytic activity are the same reported in the evaluation of series TT and HY, and a systematic study at three different UVA incident light intensities was carried out.

The results of the photocatalytic test of calcined (series TTA) samples are reported in Fig. 5.25 and compared with the photocatalytic activity of P-25 and

of TiO_2 prepared without acidic catalysis and crystallised at analogous conditions.

It was found that, for a fixed calcinations temperature, the photocatalytic properties of TiO_2 nanoparticles was sensibly different depending on the utilisation and on the nature of the acidic catalyst used during the hydrolysis-condensation reaction. Calcined TiO_2 obtained with acidic catalysis yields a photocatalyst with reduced activity for TCE decomposition in the gas-phase, compared with the analogous TiO_2 obtained under uncatalysed conditions. The photoactivity reduction is more pronounced when HCl is used as catalyst during the hydrolysis-condensation step.

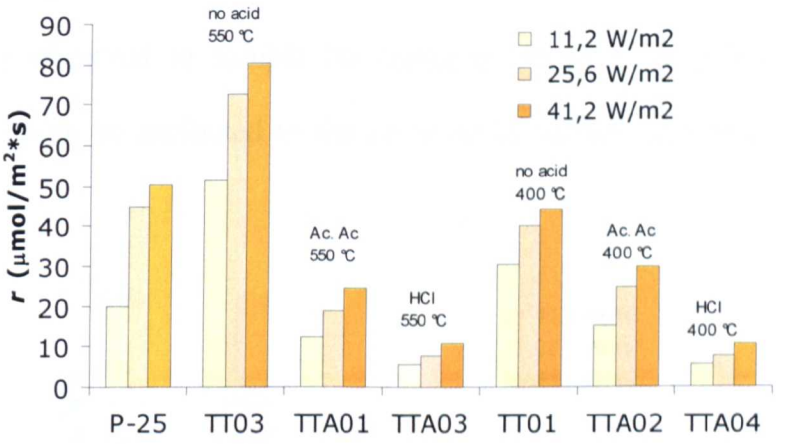

Fig. 5.25. Effect of acidic catalysis during hydrolysis-condensation on the photocatalytic activity of catalysts calcined at 400 °C and 550 °C. Initial TCE concentration was 33±1 μM (810±15 ppmv), 8% RH, flowrate: 0.04 L/s. Reaction rates are per unity surface area of irradiated support.

It was also found that the two TiO_2 samples prepared in presence of acetic acid (TTA01 and TTA02) show comparable photocatalytic activity despite being calcined at different temperatures. The same behaviour was found for catalysts prepared by using HCl and calcined at different temperatures (TTA03

and TTA04). These results show clearly that the utilisation of acidic catalysis during the hydrolysis-condensation reaction does not improve the photocatalytic performances of calcined TiO_2 in the photodegradation of TCE. As discussed in the previous sections, the processing parameter that determines the crystal growth of TiO_2 is the calcination temperature. For this reason, TiO_2 nanoparticles calcined at the same temperature have the same mean anatase crystal size despite being obtained under different sol-gel conditions (Table 5.2 and 5.3). However, the surface area of the samples obtained by acidic hydrolysis is smaller, due to changes in the porosity and morphological properties of the samples. On the base of these considerations about the morphological and structural properties, the decrease in the photocatalytic activity observed in sample belonging to series TTA compared with TT samples can be attributed to the decrease in surface area at fixed crystallite size.

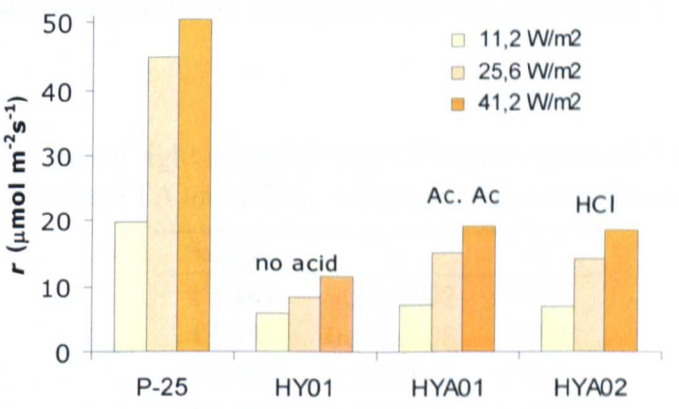

Fig. 5.26. TCE degradation rates of TiO_2 catalyst: comparison between P-25 and catalysts prepared by sol-gel without acid followed by hydrothermal treatment in mixture H_2O/EtOH with X_{H_2O}=0.59 at 150 °C/8 hours. Initial TCE concentration was 29±1 μM (716±10 ppmv), 8% RH. Reaction rates are per unity surface area of irradiated support.

With respect to the correlation between reaction rate and incident light intensity, samples belonging to TTA series show half order dependence, similarly to TT samples (Table 5.7)

In a similar fashion as for thermal TiO_2 nanoparticles, Fig. 5.26 shows the results of the photocatalytic test carried out on hydrothermal samples HYA01 and HYA02, compared with P-25 and the analogous TiO_2 obtained without acidic catalysis (HY01).

In this case the hydrothermal treatment of TiO_2 obtained by acidic hydrolysis-condensation yield to photocatalyst with comparable activity than analogous samples prepared under uncatalysed conditions at the low incident light intensity and improved activity at medium and high light intensities. The type of acid employed during the hydrolysis-condensation reaction does not appear to sensibly influence the photocatalytic activity of resultant TiO_2 nanoparticles. When compared with reference catalyst P-25, the photocatalytic activity is still much lower in the whole light intensity range considered.

Table 5. 7. Effect of light intensity on TCE reaction rate on TiO_2 nanoparticles belonging to series TTA and HYA: values of α and correlation coefficient R.

Sample	α	R
TTA01	0.54±0.02	0.999
TTA02	0.52±0.08	0.994
TTA03	0.50±0.06	0.992
TTA04	0.49±0.07	0.991
HYA01	0.76±0.06	0.992
HYA02	0.78±0.09	0.994

The characterisation of the TiO_2 samples belonging to series HYA did not evidence particular differences in terms of surface area, porosity and anatase dimension compared with TiO_2 belonging to series HY.

It is interesting to notice that samples belonging to HYA series show respectively a 0.76 and a 0.78 order correlation between reaction rate and light intensity in the light intensity range under investigation. In the same range, the hydrothermally treated sample HY01 showed half order dependence with $\alpha=0.51\pm0.04$. This fact indicates that the intensity threshold where the transition from first order to half order occurs is different for the two sets of catalysts. In HYA samples the photocatalytic process is still the predominant process at the catalyst surface, while on HY sample the predominant process is the recombination. This can explain the difference in photocatalytic activity found at high light intensities, as for a given light intensity in the range under investigation the photon harvesting leading to photocatalytic process is higher for HYA than for HY catalyst.

5.7 Further investigation on calcined TiO_2

5.7.1 TiO_2 samples

In order to further investigate the role of the phase composition and in particular the role of rutile content in determine the photocatalytic activity of TiO_2 photocatalysts, another set of TiO_2 samples were tested. These samples were prepared by Dr. Hyeok Choi in the frame of a collaboration with Professor D.D.Dionysiou, Department of Civil and Environmental Engineering, University of Cincinnati. The synthesis procedure is essentially the same employed in the preparation of TT series samples, but with the benefit of using a consistent calcination time (1h) for all specimens. The calcination treatment was carried out up to 800 °C in order to achieve materials richer in rutile than those in the TT series. Six samples were prepared and characterised,

plus the amorphous powder and the reference catalyst Degussa P-25. The structural and crystallographic properties of these photocatalysts are summarised in Table 5.8.

TiO_2 before calcination was amorphous. TiO_2 nanoparticles treated at temperatures up to 600 °C were pure anatase. Calcination at 700 °C lead to a mixture rutile anatase 55:45 and pure rutile was obtained by calcination at 800 °C. The dimension of the TiO_2 crystals increases with the calcination temperature as expected.

The crystal size of the mixed rutile-anatase sample calcined at 700 °C refers to the mean crystal size of both components. On the other hand, the surface area and pore volume of calcined titania considerably decrease with calcinations temperature.

Table 5.8. Structural and crystallographic properties of TiO_2 nanoparticles obtained by sol-gel followed by calcination for 1h at temperature between 300 and 800 °C. Amorphous sample (not calcined) and P-25 are also reported for comparison purpose.

	Crystallographic		Structural	
Temp (°C)	Phase [a]	D [b] (nm)	SA [c] (m^2/g)	V [d] (cm^3/g)
20	-	-	498	0.65
300	A	5.8	289	0.45
400	A	10.1	132	0.37
500	A	15.8	80.1	0.31
600	A	27.8	42.7	0.23
700	A45%+R55%	53.8	15.2	0.12
800	R	75.8	4.3	0.07
P-25	A70%+R30%	35	55.4	-

[a] A=anatase; R=rutile. [b] Diameter calculated from the broadening of the (101) anatase peak using Scherrer's equation. [c] Specific surface area determined using the BET method in the range 0.05<P/P0<0.35. [d] BJH desorption pore volume calculated between 2 and 300 nm

The amorphous TiO_2 particles have very high surface area (~500 m^2/g) and pore volume (0.65 cm^3/g). During thermal treatment of TiO_2 particles, the

amorphous phase was compacted and its porous structure was collapsed. As a result, the surface area and porosity were dramatically reduced with increasing calcinations temperature. Catalyst prepared at 600 °C shows a surface area almost seven times lower than that of the sample calcined at 300 °C. The surface area and pore volume of rutile TiO_2 are only 4.3 m^2/g and 22.9 cm^3/g, respectively. The surface area, particle size, and phase composition trend with calcination temperature are comparable with that obtained for TT series, confirming the material properties reproducibility of the calcination method.

From the characterization, the properties of P-25 were very similar to those of TiO_2 calcined at 500-600 °C in terms of structural properties (i.e.: surface area) and to those of TiO_2 calcined at 600-700 °C in terms of crystallographic properties (i.e.: phase composition and crystal size).

5.7.2 Photocatalytic activity

No TCE conversion was observed during preliminary experiments carried out in the dark or in absence of catalyst, and no detectable TCE photo-oxidation on amorphous TiO_2 was observed. For this set of samples the TCE inlet concentration was 25±3 μM (610±42 ppmv) and RH=8%. The effect of radiation intensity was investigated in the range 5.1-20.8 W/m^2.

The correlation between the reaction rate and incident light intensity in the range 5.1-20.8 W/m^2 is reported in Table 5.9. In this light intensity range P-25 follows a first order dependence. Similarly photocatalysts containing rutile show a first order correlation, while anatase samples vary between half order and first order.

The results of the photocatalytic test of this series of TiO_2 nanoparticles are very similar to those obtained for photocatalysts belonging to TT series. The TCE reaction rate increases linearly with calcination temperature on samples made of anatase only, to drop drastically on anatase-rutile mixed and pure rutile photocatalyst (Fig. 5.27).

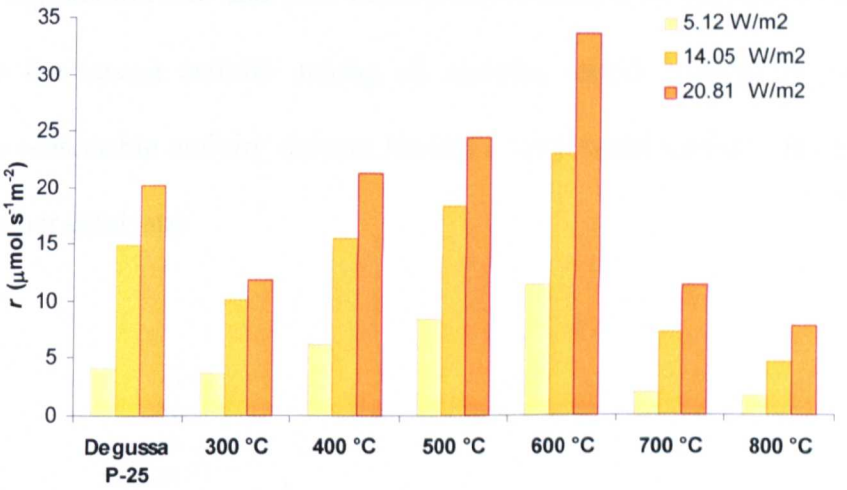

Fig. 5.27. TCE degradation rates of TiO_2 catalyst: comparison between P-25 and catalysts prepared by sol-gel followed by 1 h calcination at temperature between 300 and 800 °C. Initial TCE concentration was 25±3 μM (610±42 ppmv), 8% RH. Reaction rates are per unity surface area of irradiated support.

Table 5.9 Effect of light intensity (5.1-20.8 W/m^2) on TCE reaction rate on TiO_2 nanoparticles calcined at temperature between 300 and 800 °C: values of α and correlation coefficient R.

Sample	α	R
300	0.45±0.13	0.987
400	0.89±0.20	0.999
500	0.77±0.01	0.999
600	0.75±0.04	0.997
700	0.96±0.04	0.999
800	0.90±0.08	0.997

Sample calcined at 300 °C shows a TCE degradation rate comparable with that of P-25 at the lowest light intensity, and lower than that of P-25 in the

higher intensity range. TiO_2 photocatalyst calcined at 400 °C show comparable activity with that of Degussa P-25 in the whole light intensity range. Samples calcined at 500 and 600°C show improved activity compared with the reference catalyst P-25 in the whole light intensity range studied. The mixed phase sample prepared by calcination at 700 °C show a sensible decrease in the TCE degradation rate and pure rutile phase obtained by calcination at 800 °C shows the lowest activity among all samples tested. Noticeably pure rutile shows reasonable activity despite having a very small surface area compared with other catalysts/

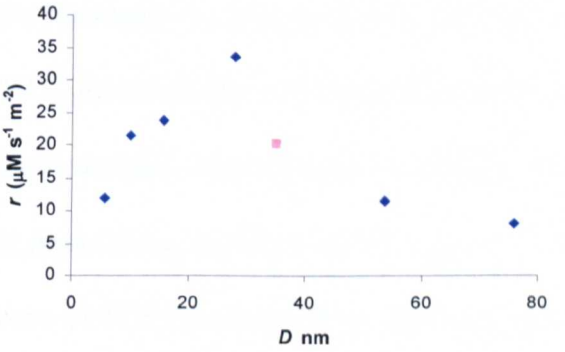

Fig. 5.28. TCE degradation rates of TiO_2 as function of mean crystal size. Diamonds denote catalyst prepared by calcination between 300 and 800 °C and square denotes Degussa P-25. Initial TCE concentration was 25±3 μM (610±42 ppmv), 8% RH. Reaction rates are per unity surface area of irradiated support.

In a similar fashion as for TT series samples, the high activity observed in samples calcined between 300-600 °C can be clearly related with the crystallite size of the anatase phase in the samples. Samples calcined up to 600 °C are made up of pure anatase with crystallite size that increases with calcination temperature. Also for this TiO_2 series an optimum value of 28 nm

(correspondent to sample crystallised at 600°C) was found (Fig 5.28). This value corroborate with the optimum crystallite size found during the TT series photocatalytic evaluation. In addition, it is close to anatase crystal dimension reported by Jung *et al* for TCE degradation in the gas phase (Jung *et al.*, 2002)

The photocatalytic activity drops dramatically in sample prepared at 700 and 800 °C. In these samples the crystallisation of titania at high temperatures lead to considerable crystal growth (53 and 75 nm respectively), but also to phase transformation: sample calcined at 700 °C contain 45% of rutile while titania calcined at 800 °C is pure rutile. Comparing these photoactivities with that of sample TT04, made of 5% rutile, and with P-25 made of 30% rutile, it is noticeable that the photoactivity decreases with rutile content in the sample. A decrease in the TiO_2 photocatalytic activity with presence and increase of rutile content in the photocatalysts, was reported already for the photo-oxidation of TCE in the liquid phase (Jung and Park, 1999, Jung *et al.*, 2002). These results indicate that in case of TCE photo-oxidation the presence of rutile may have a detrimental effect on the overall photocatalytic efficiency of the catalyst, probably due to dilution effect.

These results supports the conclusions drawn during the study of TT series, confirming that the crystal size of anatase is a most important factor than the surface area and that a linear correlation between crystal size and photoactivity exists for pure anatase photocatalysts due to fast interfacial charge transfer rate. They also confirmed the low activity of rutile titania obtained by sol-gel followed by calcination to which is unavoidably associated a very low surface area. The low activity of the rutile titania affects also the photocatalytic performance of mixed titania, proportionally to its presence in the sample.

5.8 Summary

A range of highly active calcined TiO_2 photocatalysts has been obtained by a modified sol-gel method, which exceed Degussa P-25 photoactivity for degradation of TCE in the gas phase. The effects of processing parameters on the structural, crystallographic, morphological and photocatalytic properties of sol-gel obtained TiO_2 have been studied. In particular the effect of acidic hydrolysis condition during the hydrolysis-condensation reaction and the impact of thermal and hydrothermal treatment as crystallisation methods have been investigated. It was found that calcination temperature and water content rule the titania crystal growth in the thermal and hydrothermal processes, respectively. For given crystallisation conditions, the acidic hydrolysis during the hydrolysis step does not affect the structural and crystallographic properties of the titania. However, it has an important effect on the morphology of the particle aggregates.

With regard to the photocatalytic properties, it was found that samples obtained by hydrothermal treatment show much lower activity compared with TiO_2 crystallised by calcination, despite having higher surface area. The photoactivity strongly depends on the crystal size of titania and also on the presence and percentage of rutile in the photocatalyst. A linear relationship between crystal size and photoactivity was found in anatase titania, probably due to faster interfacial charge transfer rate at catalyst surface. The best performing sample was pure anatase, with an optimal crystal size of 28 nm. The presence of rutile has a negative effect on the photocatalytic activity probably due to its low activity towards TCE photodegradation. The synthesis procedure has proved to be highly reproducible with respect to material

properties and photocatalytic activities as demonstrated by studies carried out on Cincinnati's prepared specimens.

Chapter 6

Nitrogen doped TiO_2

6.1 Introduction

The understanding of the photocatalytic mechanism and the development of materials for photocatalytic applications went through considerable development in the last few decades. However, despite this progress, the design of a photocatalyst that can be used under solar or natural illumination still represent a major challenge for the scientific community in the field of photocatalysis (Section 2.2.7.1).

In Chapter 5 the improved photocatalytic activity under UV irradiation of a range of TiO_2 samples obtained by a modified sol-gel method have been reported and discussed. The enhanced activity of some of these TiO_2 nanoparticles was attributed to a fast interfacial electron transfer at the catalyst surface with adsorbed species during the photocatalytic process.

In the present chapter, the modification of these improved TiO_2 materials by means of anionic doping is reported. The purpose is to obtain incorporation of N atoms into the TiO_2 lattice, which should either shift the photocatalytic activation to visible light range, or create crystalline defects on the catalyst surface which might result in enhanced charge separation, leading to higher activity also under UV light (Section 2.2.7.3).

6.2 Samples prepared

The synthesis procedure of N-doped TiO_2 photocatalysts is based on the modified sol-gel scheme reported in the previous chapter, which consists of a hydrolysis-condensation reaction, followed by calcination. The introduction of N atoms in the titania crystal lattice has been carried out in different ways:

1. During hydrolysis-condensation reaction by addition of NH_3 or triethylamine (NEt_3) to the reaction mixture (method 1).
2. On the amorphous TiO_2 by addition of NH_3 or triethylamine (NEt_3) to a suspension of amorphous TiO_2 (method 2).
3. By hydrothermal reaction of $TiOSO_4$ in presence of NH_3 (method 3).

The synthetically routes are fully described in the methodology part (Section 4.1.3), and Table 6.1 summarises the experimental conditions for samples obtained.

Table 6. 1. Process conditions for preparation of N-doped TiO_2.

Sample	Method	Source of N	Thermal Crystallisation	TiO_2 colour
N-$TiO_2$01	1	NEt_3	450 °C, 1 h	Light yellow
N-$TiO_2$02	1	NH_3	550 °C, 1 h	Light yellow
N-$TiO_2$03	2	NEt_3	550 °C, 1 h	Light yellow
N-$TiO_2$04	2	NH_3	450 °C, 1 h	Light yellow
N-$TiO_2$05	3	NH_3	450 °C, 1 h	Light yellow

The TiO_2 powders show a light yellow colour, indicating a change in the crystal structure with N insertion in titania lattice, that is analytically investigated in the following paragraphs.

6.3 Characterisation

6.3.1 X-ray studies

XRD analyses of all samples obtained show that only pure anatase was obtained and diffraction patterns are reported in Fig.6.1.

Table 6. 2. Crystallographic and structural properties of N-doped TiO_2.

Sample	Crystallographic Phase	D^a (nm)	Structural SA^b (m^2/g)	$V_{PORE}{}^c$ (cm^3/g)
N-Ti01	Anatase	20.4	87,3	0.384
N-Ti02	Anatase	28.1	62,2	0.256
N-Ti03	Anatase	20.2	88,6	0.308
N-Ti04	Anatase	27,8	65,4	0.287
N-Ti05	Anatase	9.0	121,8	0.245

a) Diameter calculated from the broadening of the (101) anatase peak using Scherrer's equation. b) Specific surface area determined using the BET method in the range $0.05<P/P_0<0.35$. c) BJH desorption pore volume calculated between 2 and 300 nm

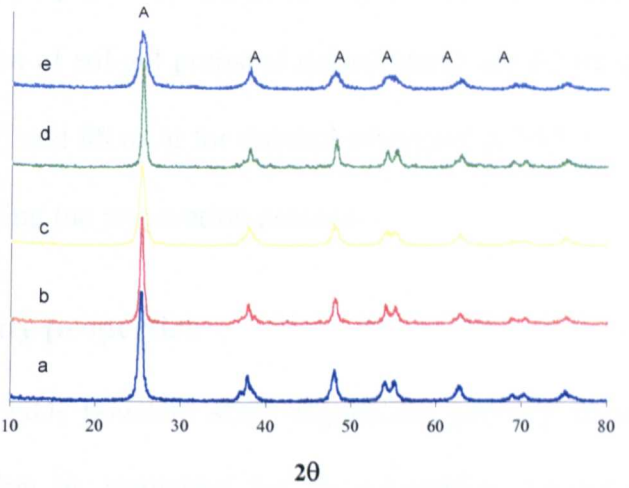

Fig. 6. 1. XRD patterns of N-doped TiO_2 samples a) N-Ti01; b) N-Ti02 c) N-Ti03; d) N-Ti04; e) N-Ti05. A= anatase.

All N-doped samples were identified as anatase, according with JCPDS 21-1272. As reported in Table 6.2, N-doped TiO_2 prepared by sol-gel and calcined at 450 and 550°C show crystal size of about 20 and 28 nm respectively, in good agreement with crystal size of sol-gel obtained pristine TiO_2 crystallised by calcinations at the same temperatures (Chapter 5). Thus, the crystallite size of sol-gel prepared N-doped TiO_2 varied with the calcinations temperature regardless the N-insertion method and the N source used. Interestingly, the

sample N-Ti05, shows a broad main anatase peak, indicating a small mean particle size of the material. N-Ti05 was prepared by hydrothermal procedure followed by calcination at 450 °C. It shows particle size of 9 nm, much smaller than crystal mean dimension of other samples treated at the same temperature (Table 6.2). This result agrees with trend reported in Chapter 5 in this work and other studies in the literature (Maira *et al*, 2000), where the hydrothermal process leaded to crystals with smaller mean size than those obtained by thermal crystallisation. The small particle size reflects also on the surface area of hydrothermally prepared doped titania, which shows the largest value (121,8 m^2/g). Surface area of sol-gel prepared doped titania are 62 m^2/g for powders calcined at 450 °C and 88 m^2/g for thermal treatment at 550 °C, regardless the N source used during the preparation process.

6.3.2 Porosity properties

The N-doped TiO_2 powders show significant porosity in the meso and macroporous region as suggested by N_2 adsorption desorption isotherms reported in Fig 6.2.

Isotherms are of type IV, according with BDDT classification(Chapter 4), and present clear hysteresis of type H2 at P/P0>0,4 for samples N-Ti02 and P/P0>0.55 for all other samples.

It was not possible to achieve a pore size distribution with the BJH method for these samples, probably due to the wide distribution along the meso and macroporous dimension range. N doped TiO_2 catalyst show similar pore volume (Table 6.2).

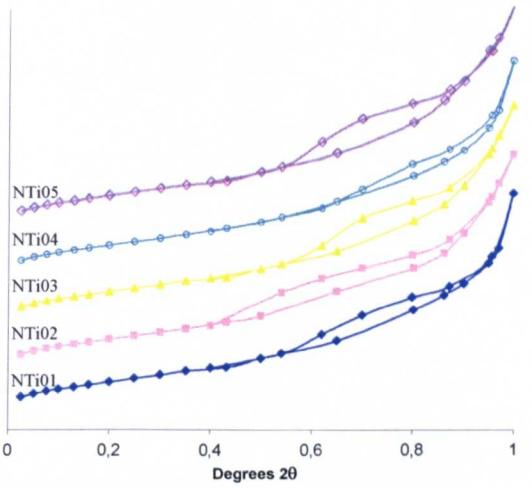

Fig. 6. 2. N_2 adsorption desorption isotherms of N-doped TiO_2.

6.3.3 XPS studies

The surface composition and chemical state of the elements in the N-doped TiO_2 samples was studied using X-ray Photoelectron Spectroscopy (XPS). The representative survey XPS spectrum of sample N-Ti05 with signals attribution is shown in Fig. 6.3. Signals from O 1s (528 eV), Ti 2p (457 eV), and N 1s (400 eV) can be easily recognised in the spectrum. The spectra of other samples show similar patterns, exception for the quantitative ratio of the elements. The atomic composition of the doped TiO_2 powders is reported in Table 6.3, which evidences different N contents at the catalysts surface for the different samples. N content between 1.9 and 4% was found in the samples.

Table 6. 3. Atomic composition % of N-doped TiO_2 catalysts.

Sample	Atomic composition %			
	O	Ti	C	N
N-Ti01	65,77	25,49	6,20	2,55
N-Ti02	64,53	26,58	6,76	2,12
N-Ti03	64,47	25,96	6,96	1,897
N-Ti04	65,18	25,21	7,33	2,984
N-Ti05	62,42	26,01	7,52	4,05

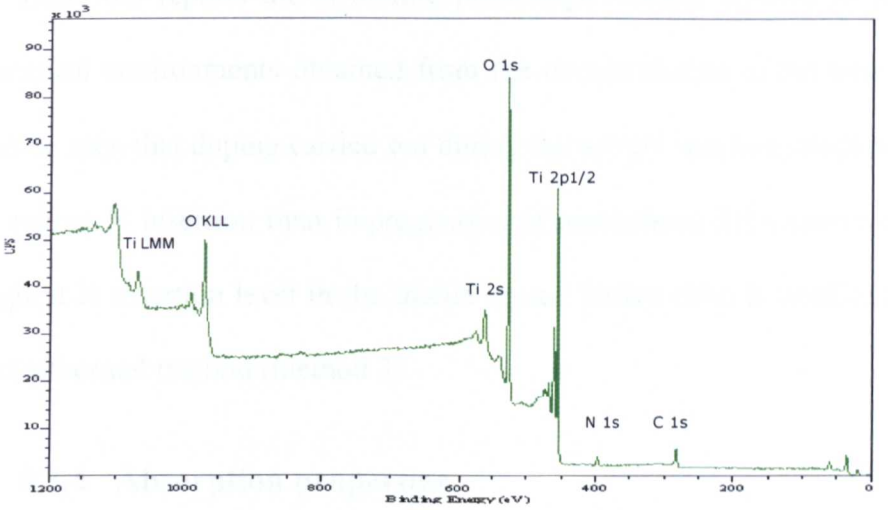

Fig. 6. 3. Survey XPS spectrum of sample N-Ti05.

The XPS peak of N 1s can be deconvoluted into two peaks centred at 399 and 396.5 respectively. The component at lower binding energy can be assigned to chemisorbed ammonium species that may derive from amination agent residues at the catalyst surface (Sathish *et al*, 2007). The component at higher binding energy is characteristic of N-Ti bond, and indicates an incorporation of N in the titania crystal lattice (Asahi *et al.*, 2001, Sathish *et al.*, 2007).

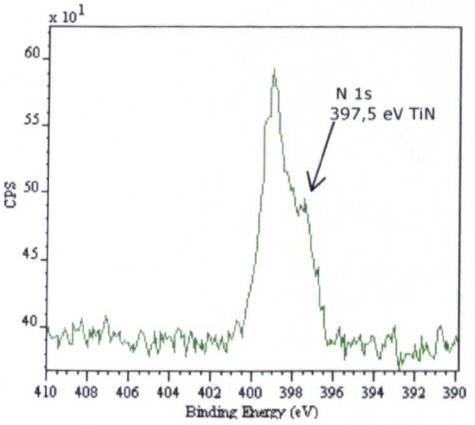

Table 6. 4. N atomic composition from deconvolution of N 1s peaks.

Sample	Atomic comp %	
	N-R	N-Ti
N-Ti01	1.58	0.97
N-Ti02	0.92	1.2
N-Ti03	1.257	0.64
N-Ti04	2.404	0.58
N-Ti05	1.94	2.1

Fig. 6. 4. N 1s XPS peak. Showing the shoulder attributed to N-Ti bond.

Table 6.3 reports the N atomic percentage relative relative to the two N chemical environments obtained from the deconvolution of the two peaks. It can be seen that doping carried out during the sol-gel reaction (method 1) leads to higher N insertion than impregnation of amorphous TiO_2 (method 2). The highest N insertion level in the titania crystal lattice (2%) is obtained with the hydrothermal method (method 3).

6.3.4 Absorption properties

The XPS analysis confirmed the insertion of N atoms into the titania crystal lattice. It was found in previous studies that the modification of the crystal composition with the introduction of anions in place of oxygen atoms lead to shift of absorption properties of doped titania.

The absorption spectra of $TiO_{2-x}N_x$ were recorded and compared with Degussa P-25 as reference material, as shown in Fig. 6.5.

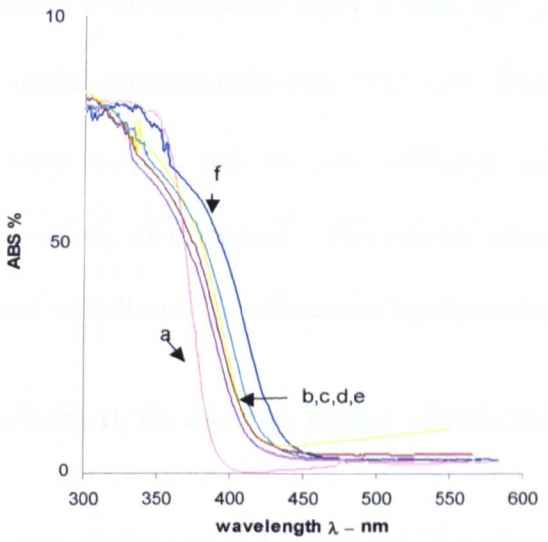

Fig. 6. 5. Optical absorption spectra of: a) Degussa P-25, b) N-Ti01, c) N-Ti02, d) N-Ti03, e) N-Ti04, f) N-Ti05.

The UV–vis absorption spectra collected in diffuse reflectance mode, of N-doped TiO_2 and TiO_2 P-25 samples are shown in Fig. 6.5. Commercial material P-25 shows an onset absorption at 405 nm, which corresponds to a bandgap energy Eg =3.1 eV. It can be seen from the figure that there is a shift in the onset absorption towards the longer wavelength region for all N-doped samples when compared to undoped TiO_2. The absorption spectrum of N-doped TiO_2 obtained by sol-gel method, are similar, with a shift between 25-30 nm, while the sample N-Ti05 shows al arger shift (60 nm) in the onset absorption.

6.4 Photocatalytic activity

The photocatalytic activity of N-doped TiO_2 materials in the gas phase were tested in the flat plate photoreactor using TCE as probe pollutant. Two different series of experiments were carried, using UV and visible irradiation sources, respectively.

All experiments were conducted using a total flow rate of 0.04 L s^{-1}, RH of 8%, and TCE initial concentration was 26±1 μM. Experiments under UV and visible light were carried out on two different supports, coated with a photocatalysts loading of 6 mg/cm^2. The results obtained for $TiO_{2-x}N_x$ were always compared with those of commercial material Degussa P-25.

6.4.1 Photocatalytic activity under visible light

It has been proven Section 6.3.4 that the N insertion in the titania crystal lattice was carried out successfully, and that the absorption properties of resulting $TiO_{2-x}N_x$ were expanded toward wavelengths in the visible range of the spectrum.

Experiments on Degussa P-25 under visible illumination did not show any photocatalytic conversion of TCE. This results was expected, and agrees with results reported in literature, as P-25's absorption onset is in the UV range, thus cannot be activated by the visible irradiation source.

However, also the evaluation of the photocatalytic properties of $TiO_{2-x}N_x$ samples under visible illumination yield no photocatalysis. In fact, no TCE conversion was recorded for all the N-doped samples, despite their capacity to absorb some visible light. The highest shift of the adsorption onset of the doped samples is of 60 nm, which means that the longest wavelength that can be absorbed is 450 nm. The emission spectrum of the visible irradiation source used in this work is reported in Figure 4.2. The visible lamps emit between 400 and 675 nm, but the portion of the spectrum emitted below 450 nm is very small and the portion in the UV range is less than 1%. Thus we can assume that the adsorption properties of N-doped catalysts are not sufficient for being activated under the visible irradiation conditions employed for the investigation.

6.4.2 Photocatalytic activity under UVA light

The photocatalytic activity of photocatalytic plates coated with N-doped TiO_2 was investigated also under UVA irradiation. The results of the photocatalytic experiments are reported in Fig. 6.6 and compared with the photoactivity of Degussa P-25. The photocatalytic activity of N-doped photocatalysts is higher or comparable with that of -25 at low light intensity. At high light intensity only sample N-Ti02 and N-Ti04 shows activity comparable with that of the commercial TiO_2 P-25.

For a given preparation method (see table 6.1) the N-doped samples obtained using NEt_3 as N source perform better than photocatalyst prepared by using NH_3 during the process. The hydrothermally obtained sample show an activity intermediate between the other two groups.

However it is important to recall that undoped samples prepared in Chapter 5 at similar conditions, which show similar structural properties (i.e. particle size) were found to perform much better than commercial P-25 under the same experimental conditions, for TCE photooxidation. The insertion of N in the crystal lattice of these photocatalysts lead to a decrease of the photocatalytic activity.

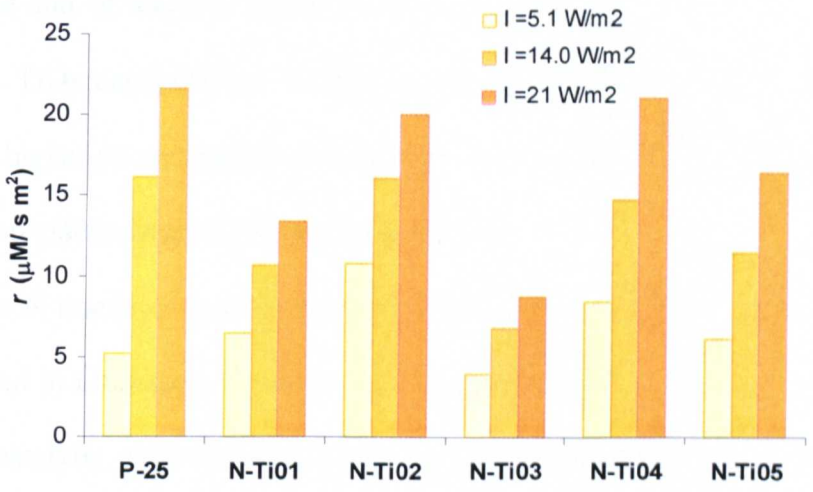

Fig. 6. 6. TCE degradation rates of N-doped TiO_2 photocatalyst under UVA irradiation at different light intensities, compared with Degussa P-25. Initial TCE concentration was 26±1 μM, 8% RH, Flowrate: 0.04 L/s. Reaction rates are per unit surface area of irradiated support.

The high activity of undoped TiO_2 nanoparticles was related with the good crystallinity of the samples and the optimum crystal size, which guaranteed a

fast charge transfer from the catalyst surface to the adsorbate species. The insertion of N into the crystal lattice can sensibly modify the crystallinity of the material, as crystal defects can be associated with doped materials. The doping centre itself can act as recombination centre during the photocatalytic process having a detrimental effect on the photocatalyst performance. Moreover, the N insertion gives rise to titanium nitride Ti-N, as also confirmed by XPS studies (Figure 6.4). Ti-N is an electron conductor, thus it may assist the electron-hole recombination process, leading to electron-hole pairs with shorter lifetime.

6.5 Summary

The aim of this part of the research work was the N-doping of the highly active TiO_2 nanoparticles developed and studied in Chapter 5, which show much higher photocatalytic activity than P-25 under UV light, in the attempt to develop visible light activated photocatalysts.

The N insertion was successfully carried out by following some procedures reported in Literature. However, no visible light activity was achieved, and the photocatalytic activity of N-doped nanoparticles under UV irradiation was lower than undoped TiO_2 with similar structural properties. It is hypotesised that the N doping creates energy levels that can act as recombination centres, decreasing the overall efficiency of the photocatalysts.

Chapter 7

TiO_2/WO_3 systems

7.1 Introduction

Coupling TiO_2 with another semiconductor is one of the approaches used to improve the photocatalytic activity of TiO_2 (Chatterjee and Dasgupta, 2005, Do *et al.*, 1993). TiO_2/WO_3 systems have recently raised the interest of researchers due to their photocatalytic and photoelectrocatalytic properties (Georgieva *et al.*, 2007, Georgieva *et al.*, 2005, Tada *et al.*, 2004).

WO_3 is a semiconductor with an energy bandgap of 2.8 eV that exists in several crystalline forms. It can absorb radiation of wavelength shorter than 420 nm, which fall in the visible range. Among all WO_3 crystalline forms, monoclinic and orthorhombic (Fuerte *et al.*, 2002) are the most commonly encountered in photocatalytic studies (Fuerte *et al.*, 2002).

In coupled semiconductors systems, the intimate contact between different oxide particles has been shown to have a fundamental role in improving the photocatalytic properties (Tada *et al.*, 2004). Thus, in the preparation and optimisation of TiO_2/WO_3 systems, synthetical pathway, experimental conditions and deposition methods can all play a crucial role in determining the final photocatalytic properties of the material.

In this chapter studies on two different coupled TiO_2/WO_3 systems are presented. A layered TiO_2/WO_3, and a novel TiO_2/WO_3 nanocomposite obtained through a one step hydrothermal reaction are investigated. The morphologic, structural and photocatalytic properties of both TiO_2/WO_3 systems are reported and discussed.

7.2 Layer structured TiO_2/WO_3 system

A common material configuration for semiconductor coupled systems is obtained by deposition of single oxides films forming a layered structure. This configuration is commonly achieved through techniques such as sol-gel (Song *et al.*, 2001), chemical vapour deposition CVD (Harizanov *et al.*, 1996), electrodeposition (de Tacconi *et al.*, 2003), and can utilise commercial starting materials. In the frame of a project in collaboration with the Institute of Physical Chemistry in the Bulgarian Academy of Science, Sofia, Bulgaria, a set of layered systems were tested in the gas phase photocatalytic reactor for photodegradation of TCE. Supports coated with both WO_3 and TiO_2 and supports coated with only WO_3 were evaluated.

7.2.1 Preparation and characterisation of supports

The photocatalytic supports coated with WO_3 and TiO_2 were prepared by Jenia Georgieva from the Institute of Physical Chemistry in the Bulgarian Academy of Science. In this section the preparation method and characterisation of these TiO_2/WO_3 layered systems are reported briefly as a comprehensive description and discussion of these systems can be found in literature (Georgieva *et al.*, 2005, Georgieva *et al.*, 2007).

WO_3 single coatings and WO_3/TiO_2 layered coatings were prepared on stainless steel (SS304) supports, by an electrosynthesis/electrodeposition technique from precursors solutions. Na_2WO_4 was used as W precursor and after WO_3 deposition the coated SS plates were annealed at 350 °C for 30 minutes to allow crystallisation of the oxide. TiO_2 was deposited on top of the

WO_3 layer by electrosynthesis/deposition from $TiOSO_4$ solution, and then annealed at 400 °C for 1 hour.

XRD analysis show that the coatings are composed of anatase TiO_2 and monoclinic WO_3. The crystal dimension analysis is not reported in Georgeva's work.

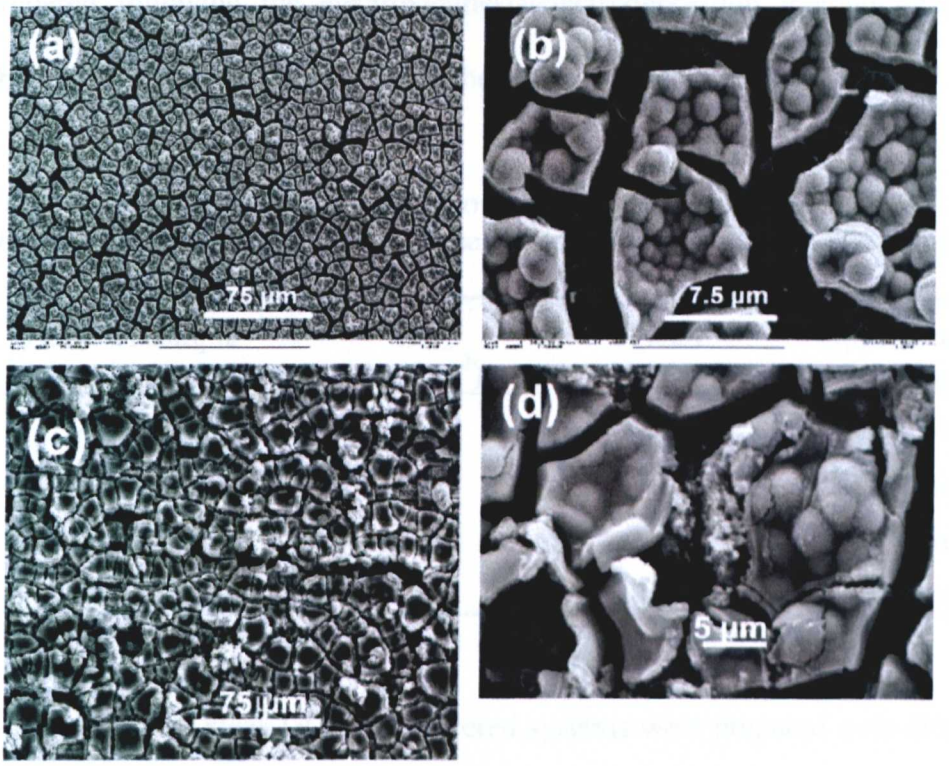

Fig. 7. 1. SEM micrographs of (a) and (b): plain WO_3 coating (loading: 1.2 mg/cm^2); (c) and (d): bi-layer TiO_2/WO_3 coatings, (loading 0.36 and 1.12 mg/cm^2 respectively) on SS 304 substrates (From Georgieva *et al*, 2007).

SEM micrographs showed that all coated supports present a similar morphology (Fig. 7.1). In all cases, the coatings appeared to be made up of large aggregates with variable dimension, between 5 and 20 µm, separated by cracks. In bilayered systems, the aggregates had a peculiar oxide distribution on the coating surface, which was studied by Energy Dispersed X-Ray

Spectroscopy (EDS) and Auger Electron Spectroscopy (AES). It was found that the aggregates consisted of TiO_2 while the cracks areas were made up of only WO_3, thus they are probably formed by shrinkage of the anatase film during drying and annealing steps.

Four stainless steel plates (dimensions: 10 cm long, 7.5cm wide) were prepared following the electrosynthesis/electrodeposition method described above. Loading and composition of these supports are reported in Table 7.1.

Table 7.1. TiO_2 and WO_3 loadings on stainless steel supports studied for the photodegradation of TCE in gas phase under UVA and visible light irradiation.

Name of sample	TiO_2 (mg/cm^2)	WO_3 (mg/cm^2)	Appearance of coatings
WO3-105	0.3	1.05	Green
WO3-09	0.55	0.9	Light green
WO3-110	/	0.8	Dark green
WO3-92	/	1.2	Dark green

Two stainless steel TiO_2/WO_3 layered systems were prepared with different oxides loading. In both bilayered systems WO_3 loading is higher than TiO_2. WO_3-TiO_2 loading ratio is 3.5 for sample WO3-105 and 1.6 for WO3-0.9. The other two stainless steel plates were coated with only WO_3 at different loadings for comparison purposes and in order to test WO_3 itself as photocatalyst for TCE degradation in the gas phase.

The specimens tested in the photocatalytic reactor were not fully characterised. However, being the preparation method and the oxides loading very similar with the coatings described above, they are assumed to have comparable morphology and composition.

7.2.2 Photocatalytic activity

Photoelectrocatalytic experiments for malachite green oxidation carried out using WO_3/TiO_2 bilayered systems obtained with the electreosynthesis-electrodeposition technique showed good photoelectrocatalytic activity under UV irradiation and also under visible light illumination (Georgieva *et al.*, 2007). For this reason the coated plates were tested for photodegradation of TCE in air under UV and visible light irradiation. The experiments were carried out using the photocatalytic reactor system in its initial set up, consequently the syringe pump was used to inject the pollutant into the system and all gas flows were controlled by flowmeters (Section 4.3.2.1). The experimental conditions are briefly reported in Table 7.2.

Table 7.2. Experimental condition for photocatalytic degradation of TCE on TiO_2/WO_3 layered systems.

	RUN 1	RUN 2
RH	8%	8%
Total flow rate (ml/h)	2300	1800
TCE injection rate (ml/h)	0.5	0.3
$[TCE]_i$ (ppm)	700	300
	15.4	15.4
UV Light intensity (W/m^2)	11.2	11.2
	45.0	45.0
Visible light intensity	not measured	not measured

Experiments under Run 1 conditions were first run carried out under visible and UVA light (343-380 nm with maximum irradiation peak at 365 nm). These conditions are comparable with those employed in evaluation of pure TiO_2 catalysts (Section 5.4.5.2). Results under visible light illumination did not show any TCE conversion for the coated plates. Surprisingly, even when the

photocatalytic supports were illuminated with UVA light, no photocatalytic process occurred.

Total flow rate and injection rate were changed in order to achieve a much lower TCE initial concentration (Run 2). Also under this condition, the catalysts did not show any activity for TCE degradation under either visible or UVA irradiation.

The results obtained from supports coated with WO_3 only, allow the assumtion that WO_3 is insufficient as a photocatalyst for TCE photodegradation. This finding is supported by the fact that, to the best of my knowledge, photodegradation of TCE using pure WO_3 as the photocatalyst has never been reported in the literature.

Concerning TiO_2/WO_3 mixed samples, unexpectedly, a total deactivation of TiO_2 derives from its coupling with WO_3 in this bilayered configuration. An accurate analysis of materials loading, surface morphology and semiconductors distribution at the surface can contribute the justification and understanding of these results. First of all, in the bilayered systems under study, the WO_3 loading is very high and in view of the WO_3/TiO_2 ratios, we can think about TiO_2 as the 'dopant' component. In layered systems, positive coupling effects have been reported when the WO_3 is loaded as a monolayer (~3% molar) on TiO_2 (Song *et al.*, 2001). It has also been observed that the activity of the mixed oxide systems decreases sharply with increasing WO_3 loading (Keller *et al.*, 2003). Moreover, given that WO_3 is not effective as a photocatalyst for TCE degradation, its high loading could affect the whole system by a dilution effect. However, considering that both components are exposed to light irradiation, some activity was expected due to presence of TiO_2.

During irradiation, electron-hole pairs are formed on both semiconductors. Even if WO_3 does not act as photocatalyst itself, it can act as sink for photoexited electrons, accepting them from TiO_2 conductive band, generating intermediate W (V) on the surface (Chapter 2). The reduced W(V) can then follow two paths: it can be oxidized to W(VI) by reaction with the holes following a recombination process, or it can react with an electron acceptor on the surface completing the photocatalytic reaction. This trapping mechanism is believed to drive the charge separation responsible for the improved activity in many Ti/W composites (Fuerte *et al.*, 2002, Do *et al.*, 1994, G. *et al.*, 1996).

$$W(VI) + e^-_{(TiO_2\,CB)} \rightarrow W(V) \qquad \text{(Eq. 7.1)}$$

$$W(V) + h^+ \rightarrow W(VI) \qquad \text{(Eq. 7.2)}$$

$$W(V) + O_2 \rightarrow W(VI) + {}^{\bullet}O_2 \qquad \text{(Eq. 7.3)}$$

Thus, in order to finalize the photocatalytic cycle, an electron acceptor must be reduced. For reaction in air, the electron acceptor specie involved in this step is O_2. It is evident that the rate of electron transfer from semiconductors to O_2 can influence the overall photocatalytic process.

The rate of electron transfer from catalyst surface to O_2 was recently determined in the frame of studies on a photocatalytic system with surface consisting of anatase TiO_2 deposited as striped pattern on top of monoclinic WO_3 on SnO_2-film-coated glass (Tada *et al*, 2004). The composition and morphology of these coatings are similar to the one of our layered systems, as shown in Fig. 7.2. In Tada's work, the photoinduced electron transfer from TiO_2 to WO_3 was demonstrated by mapping the surface reductive sites by photodeposition of Ag, however the gas phase photo-oxidation of acetaldehyde

(CH_3CHO) and liquid phase photo-oxidation of 2-naphtol decreased sensibly in the coupled system compared to those on plain TiO_2.

The authors rationalised these results in term of electron transfer rate from catalyst surface to the electron acceptor (O_2) in the photocatalytic system. For TiO_2 and TiO_2/WO_3 on SnO_2-film-coated glass it was found that the rate of electron transfer from TiO_2 to O_2 is two orders of magnitude higher than that from WO_3 to O_2. This means that once the photoexcited electrons go to WO_3 the reduction of O_2 can be so slow that it may deactivate the overall photocatalytic system. This effect can obviously become very important for high WO_3 loadings.

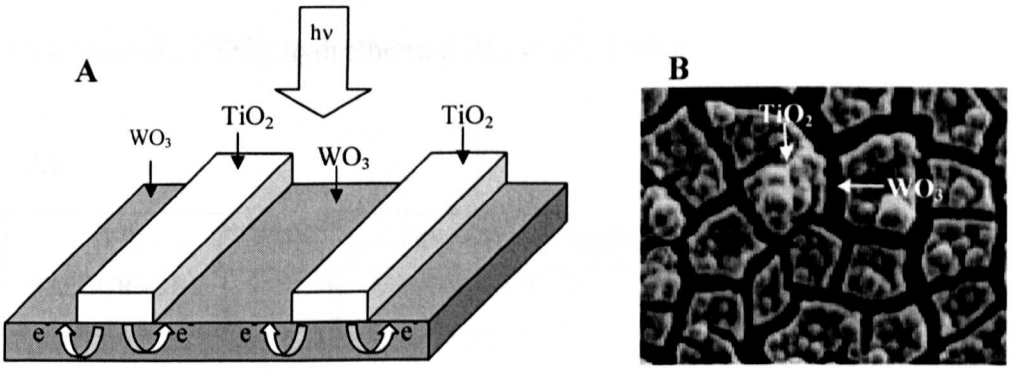

Fig. 7. 2. A) Scheme of Taka's photocatalytic system, with striped TiO_2 is deposited on WO_3, showing the electron transfer from TiO_2 to WO_3 upon illumination. B) SEM image of bilayered system under study in this work, which show similarity with Taka's system.

Conversely, the same paper describes the enhanced performances of coupled systems in electrochemically-assisted reactions. In electrochemical reaction the reduction of an electron acceptor is not necessarily required as the excited electrons are removed from the system by applying an external potential (O'Regan *et al.*, 1990). As mentioned before, the same bilayered

systems that are not active for TCE degradation under photocatalytic conditions show good performances in photoelectrochemical experiments (Georgieva *et al.*, 2005).

7.3 TiO_2/WO_3 mixed oxides

The deactivation issues encountered in the work with layered systems drove the research towards the preparation of mixed Ti/W oxides in homogeneous phase, with low W content.

So far, WO_3-doped TiO_2 photocatalysts in homogeneous phase have been prepared using mechanical method (Shifu *et al.*, 2005), sol–gel (Yang *et al.*, 2002, Yang *et al.*, 2005) impregnation (Zuo *et al.*, 2006), microemulsion (Fuerte *et al.*, 2002), hydrothermal (Ke *et al.*, 2008).

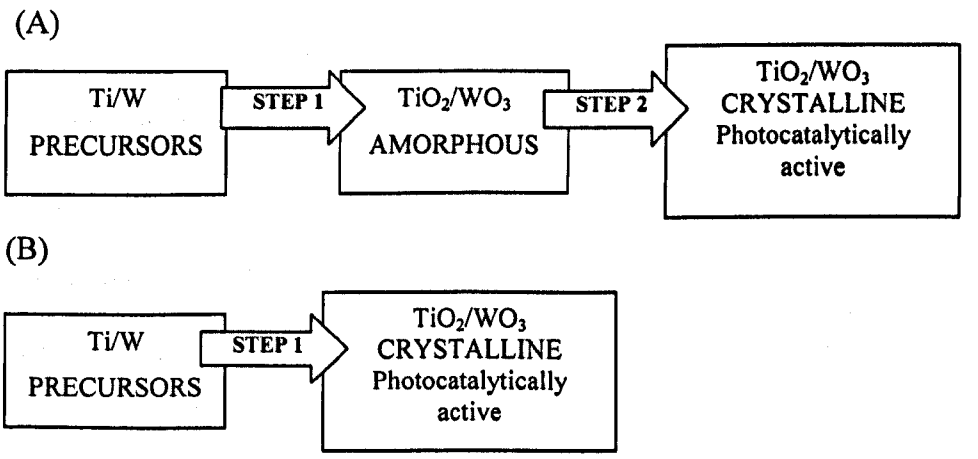

Fig. 7.3. Flow charts showing traditional two steps reaction scheme for TiO_2/WO_3 nanocomposites preparation (A), and one-step reaction scheme developed in this study (B)

In all of these synthetic methods, an amorphous precursor is first obtained (step 1), then a thermal treatment at relatively high temperatures (step 2) is carried

out to permit the formation of the final photoactive crystalline material (Fig. 7.3).

In the attempt to simplify the synthesis of TiO_2/WO_3 nanocomposites, a novel one-step synthesis based on hydrothermal method has been developed and optimised for photooxidation of TCE in gas phase.

7.3.1 A novel TiO_2/WO_3 nanocomposite

Hydrothermal treatment at high temperature of Titanium oxisulfate ($TiOSO_4$). It has been used for the preparation of TiO_2 nanoparticles (Kolen'ko *et al.*, 2003). Also WO_3 has been prepared by hydrothermal reaction, using H_2WO_4 as precursor (Kominami *et al.*, 2003). In Kominami's synthesis, orthorhombic WO_3 ($WO_3 \cdot 0.33H_2O$) and monoclinic WO_3 were obtained by treatment at 473 and 523 K respectively. However, the hydrothermal synthesis has not been used for the preparation of TiO_2 and WO_3 mixed oxides.

For samples synthesized in this work, ammonium metatungstate hydrate $((NH_4)_6(W_{12})_{41}) \cdot xH_2O$ and $TiOSO_4$ were used as W and Ti oxides precursors respectively. As starting point, pure Ti and W oxides, and Ti/W mixed oxides with 10% wt WO_3 were prepared using a mixture 1:1 water and ethanol as reaction media.

The product of the hydrothermal treatment of $TiOSO_4$ and of the mixed precursors were white powders, while by treatment of ammonium metatungstate, a very fine, light green powder was obtained.

The oxidation state of the components in the mixed oxide was analyzed by XPS spectroscopy. As shown in Fig. 7.4, sample surface is composed by Ti, O, C, F, N and W. The F signal is present because of a contamination in the

instrument chamber. Due to this contamination, only qualitative considerations can be done on the basis of this spectrum.

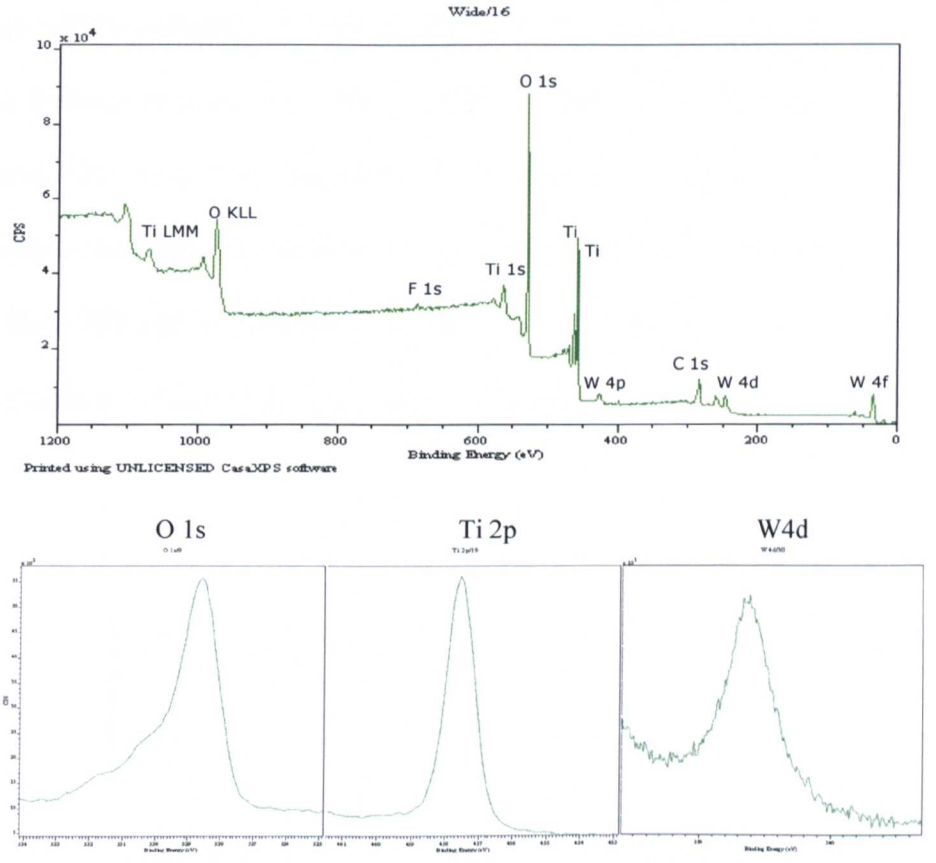

Fig. 7.4. XPS spectra of TiO_2/WO_3 10% wt WO_3. Top: survey spectrum. Bottom: O, Ti and W peaks.

The binding energy of Ti2p (457.5 eV) and W4d (247 eV) correspond to Ti(IV) and W(VI) with values typical of TiO_2 and WO_3 respectively. O 1s signal has a principal peak at 530 eV characteristic of oxide bond, and a clear shoulder at higher binding energies that correspond to hydroxyl bond. The C signal at 288 eV can be attributed to residues of ethanol on catalysts surface and adsorbed CO_2.

The crystallographic properties of the samples were investigated by X-ray spectroscopy (Fig. 7.5). From the hydrothermal reaction of $TiOSO_4$ anatase with good crystallinity was obtained (Fig. 7.5 a).

The diffraction pattern of the material obtained by hydrothermal treatment of W precursor was attributed to ammonium tungsten bronze of formula $(NH_4)_{0.33}WO_3$ in hexagonal form according to JCPDS 42-0452 (Fig. 7.5 c). The broad diffraction peaks of $(NH_4)_{0.33}WO_3$ indicate a low crystallinity of the material. Due to the unavailability of $(NH_4)_{0.33}WO_3$ single crystal, it was not possible to calculate the crystalline size of the bronze component using Bragg's law. Both diffraction patterns of anatase (23 nm crystal size) and bronze are identifiable in mixed oxide specimen (Fig. 7.5b).

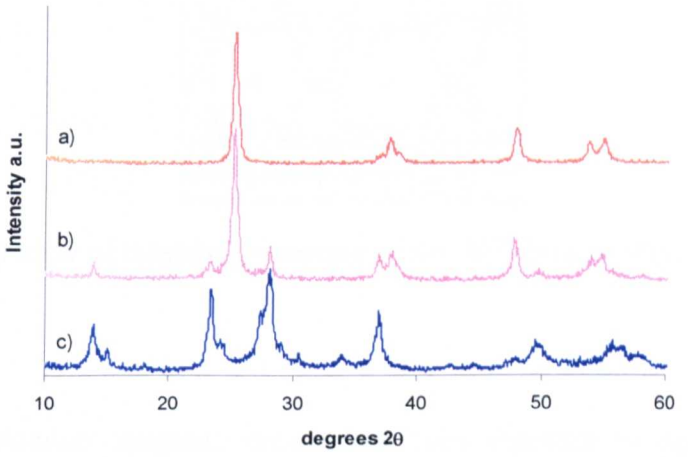

Fig. 7. 5. XRD pattern of a) TiO_2 anatase; b) mixed oxide 10% wt WO_3; c) $(NH_4)_{0.33}WO_3$

Tungsten bronzes are non-stoichiometric compounds with general formula $MxWO_3$ (with $0<x<1$) where M is an alkaline metal ion (i.e. Na^+) or NH_4^+. Peculiarity of this material is its structure which is shown in Fig. 7.6 (Fouad *et al.*, 2000). WO_6 octahedrons are joined through the corners forming a structure where two different channels type can be recognized: trigonal and octahedral channels. It is believed that trigonal channels host small ions such as Li^+ while octahedral channels host bigger cations such as NH_4^+. The presence of cations

in the crystal structure gives this materials interesting properties like electron conductivity.

Ammonium tungsten bronzes with hexagonal structure are traditionally prepared by solid state reaction of ammonium tungstate in a reducing atmosphere (H_2) at high temperatures, but hydrothermal methods have also been reported (Reis *et al.*, 1992).

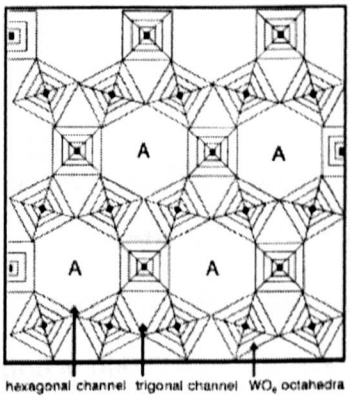

Fig. 7. 6. Top view of tunneling structure of M_xWO_3 bronze (Fouad *et al.*, 2000)

Pure ammonium tungstate bronze has been reported to decompose and undergo phase transition from hexagonal to monoclinic under calcinations at 500 °C. (Fouad *et al.*, 2000). A sample with 40% wt of WO_3 was calcined at 600 °C for 8 hours to investigate any change in the crystalline form.

From the XRD patterns registered before and after calcination shown in Fig. 7.7, it is clear that no changes in the diffraction patterns took place, hence there has been no phase transformation to the monoclinic WO_3 form in the composite. This fact can be explained supposing that TiO_2 has a stabilisation effect on the W oxide component in the composite, avoiding the phase transformation to monoclinic WO_3. Moreover, at this temperature some conversion from anatase to rutile is expected for TiO_2 (Fuerte *et al.*, 2002), but

no conversion of anatase to rutile was observed, showing that also that TiO_2 component is stabilised in the composite towards phase modification.

This is the first time that a $TiO_2/(NH_4)_{0.33}WO_3$ nanocomposite has been prepared with a easy one-step hydrothermal process (Puddu *et al.*, 2007).

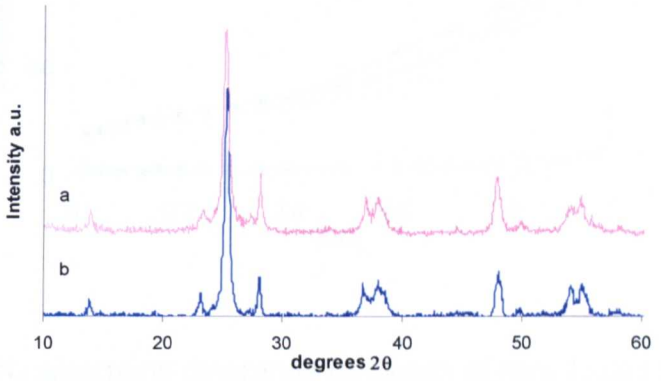

Fig. 7. 7. XRD pattern of $TiO_2/(NH_4)_{0.33}WO_3$ 40% wt $(NH_4)_{0.33}WO_3$ content a) before and b)after calcination at 600 °C for 8 hours

Fig. 7.8 shows the N_2 sorption isotherm of pure TiO_2, pure $(NH_4)_{0.33}WO_3$ and the mixed oxides. The isotherm of pure $(NH_4)_{0.33}\cdot WO_3$ matches that of a typical Type II (BDDT classification), which is usually attributed to non-porous materials or materials of very limited porosity (Section 3.2.2).

In contrast, pure TiO_2 and the mixed oxide samples present isotherms indicative of significant porosity. These N_2 sorption isotherms may generally be classified as Type IV, with clear inflection and hysteresis loop in the relative pressure $P/P_0>0.4$. The hysteresis loop can be classified as type H2, characteristic of slit-shaped pores. At relative pressures approaching P/P_0 = 0.95, the pure TiO_2 and mixed oxide exhibit significant sorption, which can be attributed to the presence of large pores or macropores arising from interparticle voids.

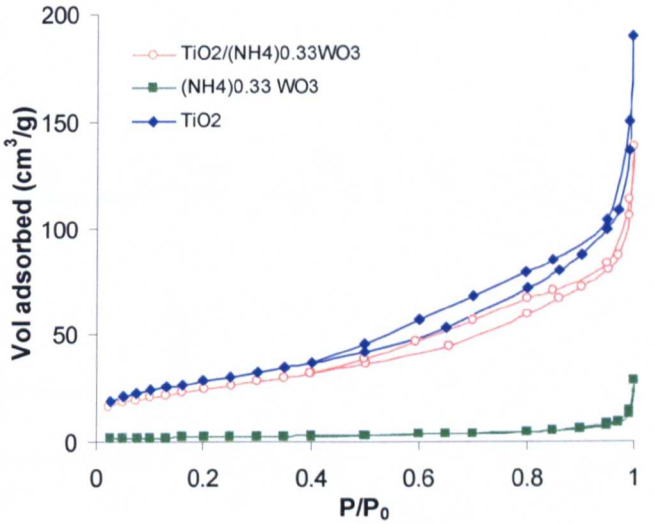

Fig. 7. 8. N_2 adsorption desorption isotherms of pure Ti and W oxides and of a $TiO_2/(NH_4)_{0.33}WO_3$ nanocomposite with 10% wt $(NH_4)_{0.33}WO_3$.

7.3.2 Optimisation of synthesis parameters: Effect of solvent composition

7.3.2.1 Material properties

In solvothermal or hydrothermal reactions, solvent composition can affect the structure, size and composition of the products (Cheng *et al.*, 1995, Kim *et al.*, 2006). To evaluate this effect, mixed oxides with 10% $(NH_4)_{0.33}WO_3$ content were prepared using different H_2O-ethanol ratios. Solvothermal syntheses were carried out in pure water, pure ethanol and mixture of the two solvents, with H_2O concentration of 70, 50 and 30% v/v respectively. The process was carried out at 150 °C for 24 hours. The effect of solvent composition on material's properties are resumed in Table 7.3. Fig. 7.9 shows the X-ray diffraction patterns obtained from the mixed oxides.

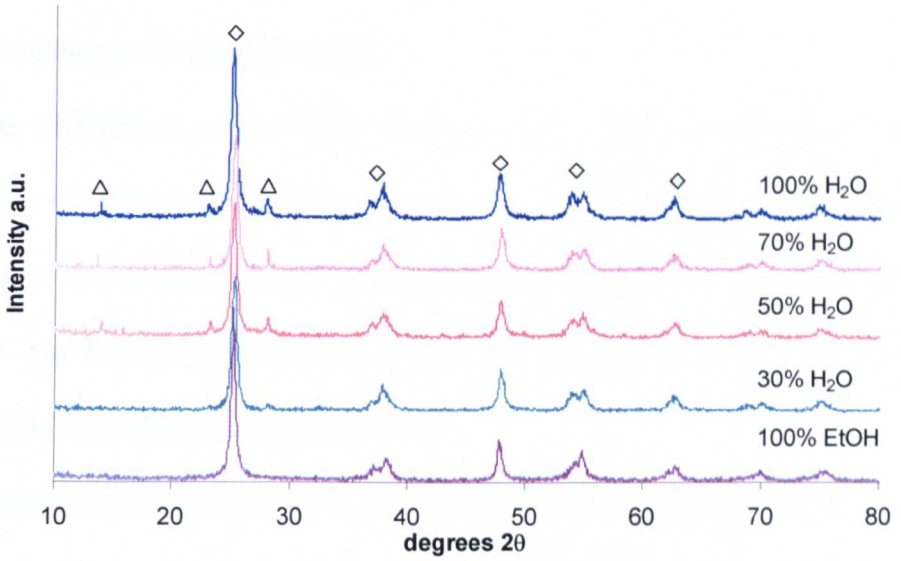

Fig. 7. 9. Diffraction patterns of 10% wt $TiO_2/(NH_4)_{0.33}WO_3$ composites prepared with different H_2O-ethanol ratios during solvothermal process. (◇=TiO_2; △=$(NH_4)_{0.33}WO_3$)

Table 7. 3. Effect of H_2O content on anatase textural properties

%H_2O	D^a (nm)	SA^b (m^2/g)	$V_{PORE}{}^c$ (cm^3/g)
100	22.67	104	0.16
70	22.06	120	0.13
50	23	136	0.135
30	23.47	112	0.18
0	43.52	89	0.19

[a] Diameter calculated from the broadening of the (101) anatase peak using Scherrer's equation. [b] Specific surface area determined using the BET method in the range 0.05<P/P0<0.35. [c] BJH desorption pore volume calculated between 2 and 300 nm

H_2O-rich mixtures lead to the formation of mixed oxides where diffraction peaks of both components are clearly identifiable. When ethanol is the solvent in excess, the intensity of the peaks relative to W bronze decrease sensibly. They disappeared completely when the reaction was carried out under pure alcohol thermal conditions.

The presence of H_2O has a fundamental role in the formation and crystallization of the$(NH_4)_{0.33}WO_3$ component. It is also worth noting that

there is no trace of precursor ammonium metatungstate or other crystalline intermediates in the final products.

The differences in the XRD patterns with respect to the presence and intensity of $(NH_4)_{0.33}WO_3$ diffraction peaks may be the result of two different scenarios. In the first, we can assume that no W bronze is formed in ethanol media and that the unreacted precursor is rinsed away during the washing procedure after filtration (Section 4.1.4).

Ammonium metatungstate, is soluble in water but it is not soluble in ethanol under ambient conditions. The presence of water allows the precursor dissolution and the crystallisation of the W bronze. On the other hand, the reaction of precursor in ethanol may give rise to an amorphous product not detectable by XRD.

Anatase crystal size does not appear to be highly affected by H_2O content being constant at values 23±1 nm. On the other hand, surface area reaches its highest value when a mixture 1:1 is used. Sample prepared in pure ethanol shows a larger anatase particle size, almost double with respect to the other samples, and a consequent lower surface area.

The N_2 sorption isotherms are reported in Fig. 7.10. All isotherms are of type IV with loops of H2 character in all cases and are characteristic of wide pore size distribution in the mesopore size range with significant adsorption starting at $P/P_0>0.4$. However, they show slightly different features depending on solvent composition. For 100% EtOH and 30% water isotherms the hysteresis loop is positioned $P/P_0>0.5$, with steep inclination at high partial pressures, indicating presence of large pores. For 50% to 100% water content

hysteresis loop is at P/P_0>0.4 with less steep trend at high partial pressures, showing smaller sorption properties at high pressures.

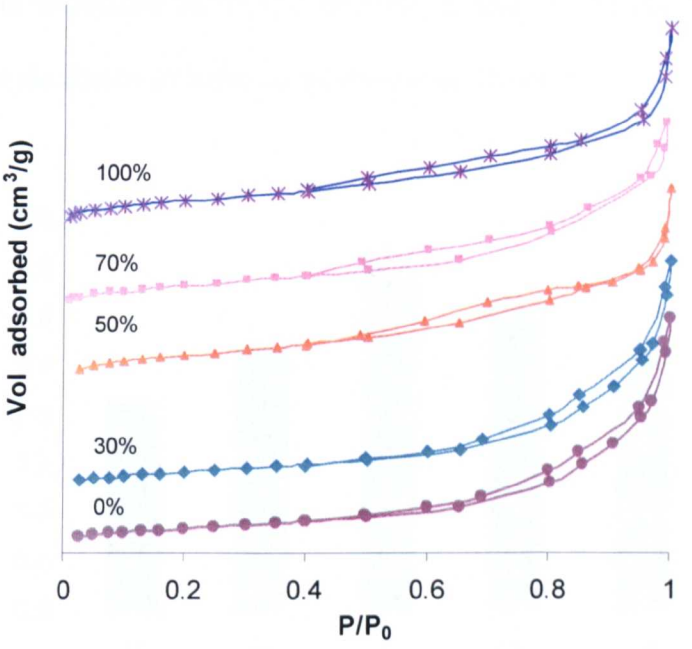

Fig. 7. 10. N_2 adsorption-desorption isotherms of $TiO_2/(NH_4)_{0.33}WO_3$ mixed oxides with 10% wt $(NH_4)_{0.33}WO_3$ prepared with different H_2O % during solvothermal process.

7.3.2.2 Photocatalytic activity

The effect of water content during hydrothermal process on photocatalytic properties of mixed oxides with 10% $(NH_4)_{0.33}WO_3$ wt was evaluated for the gas phase photodegradation of TCE. All experiments were conducted in a reaction-controlled regime using a total flow rate of 0.04 L/s, 8% RH, an initial concentration of TCE of 20.2±0.6 μM and an incident photon flux (UVA at 343-380 nm with maximum irradiation peak at 365 nm) on the supported catalyst of 5.53 W/m^2.

Results are reported in Fig. 7.11. The photocatalyst prepared under alcoholic conditions show the lowest average reaction rate. The reaction rate increases with increasing the H_2O content in the reaction media, up to a solvent ratio 1:1, and decreases at higher concentrations of water.

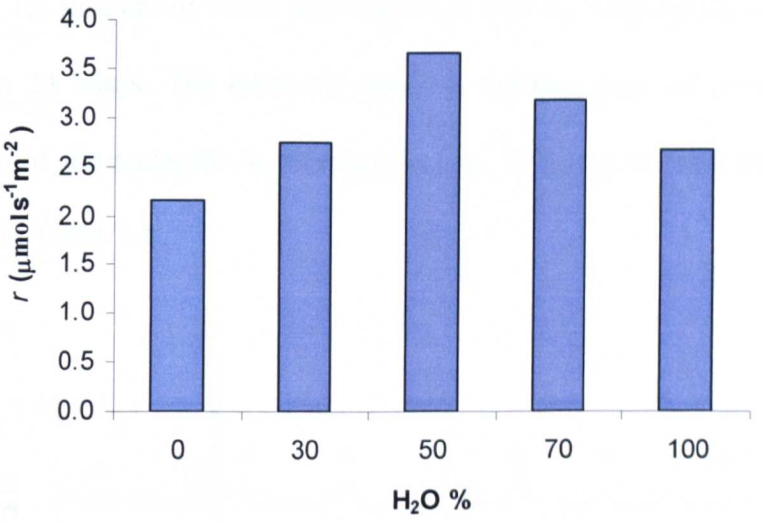

Fig. 7. 11. Reaction rate of mixed oxide 10% wt $(NH_4)_{0.33}WO_3$ loading prepared with different ethanol-water ratios during solvothermal process. Reaction rates are per unit surface area of irradiated coated supports.

The catalyst prepared with 100% ethanol did not show diffraction peaks relative to the $(NH_4)_{0.33}WO_3$ component, indicating either the absence or its presence as an amorphous phase. The other samples, where W bronze is present, show higher activity. This fact indicates that the crystallization of W bronze is an important parameter in the determination of final photocatalytic properties of the mixed oxides. Moreover, the optimum photocatalyst prepared by using a mixture 1:1 H_2O–ethanol was found to have the largest surface area. In general the photocatalytic activity grows with the surface area of the catalysts (Table 7.3) for this set of samples, thus surface area may also contribute to defining the photocatalytic performance.

7.3.3 Optimisation of synthesis parameters: Effect of reaction time

7.3.3.1 Material properties

Mixed oxides with 10% wt $(NH_4)_{0.33}WO_3$ content were prepared using the optimum 1:1 mixture of water and ethanol at 150 °C, varying the reaction time from 4 to 24 hours. The effect of different holding time on crystallographic properties of the materials is reported in Fig. 7.12 and textural properties are resumed in Table 7.4 .

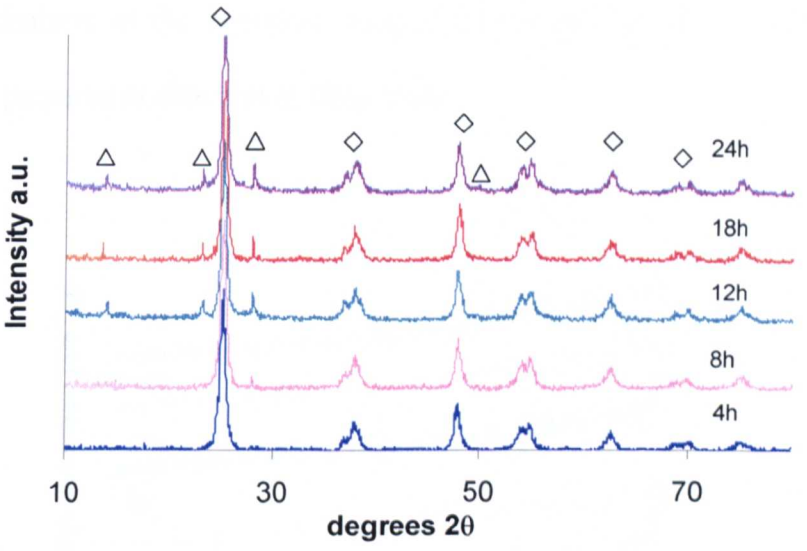

Fig. 7.12. X-Ray diffraction pattern of Ti/W mixed oxide with 10% wt $(NH_4)_{0.33}WO_3$ content, prepared in 1:1 mixture H_2O:Ethanol at 150 °C at different reaction times (◇=TiO_2; △=$(NH_4)_{0.33}WO_3$).

Holding time appears to have an effect on the crystallisation and growth of WO_3 component, while it doesn't affect much the anatase crystallographic properties. After 4 hours of reaction, anatase pattern could be clearly

identified, but no peaks from W bronze were detected. The $(NH_4)_{0.33}WO_3$ peak at 28.2 °2θ was detected after reaction for 8 hours. The complete diffraction pattern of anatse and WO_3 was then achieved after 12 hours of reaction. Further increase in the reaction time seemed not to change the diffraction pattern.

Variation in the surface area and porosity of mixed oxides with 10%wt WO_3 content were followed by N_2 adsorption-desorption analysis. N_2 sorption isotherms, shown in Fig. 7.13, are characteristic of a wide pore size distribution in the mesopore size range with significant adsorption starting at $P/P_0>0.4$. Similar features of the isotherms suggest similar porosity of the mixed oxide samples prepared at different holding times.

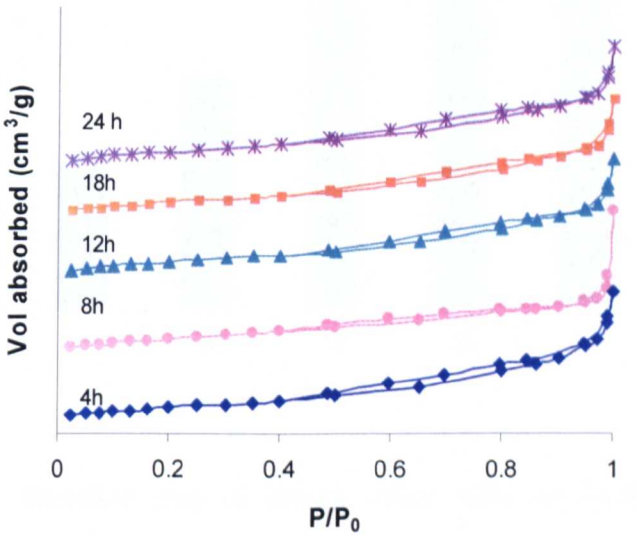

Fig. 7. 13. N_2 adsorption-desorption isotherms of mixed oxide with 10% wt $(NH_4)_{0.33}WO_3$ obtained at different hydrothermal holding time.

7.3.3.2 Photocatalytic activity

The results of photocatalytic activity of $TiO_2/(NH_4)_{0.33}WO_3$ 10% wt prepared at different holding times are reported in Fig. 7.14. All experiments

were conducted in a reaction-controlled regime using a total flow rate of 0.04 L/ s, 8% relative humidity, an initial concentration of TCE in synthetic air (20% O_2, 80% N_2; BOC gases) of 21± 2 μM and an incident photon flux (UVA at 343-380 nm with maximum irradiation peak at 365 nm) on the supported catalyst of 5.53 W/m^2.

The average reaction rate increased with increasing reaction time and doubles its value from 4 to 12 hours of holding time. Catalyst obtained by reaction longer than 12 hours did not show any further improvement in photocatalytic activity, thus 12 hours were considered to be the optimum reaction time.

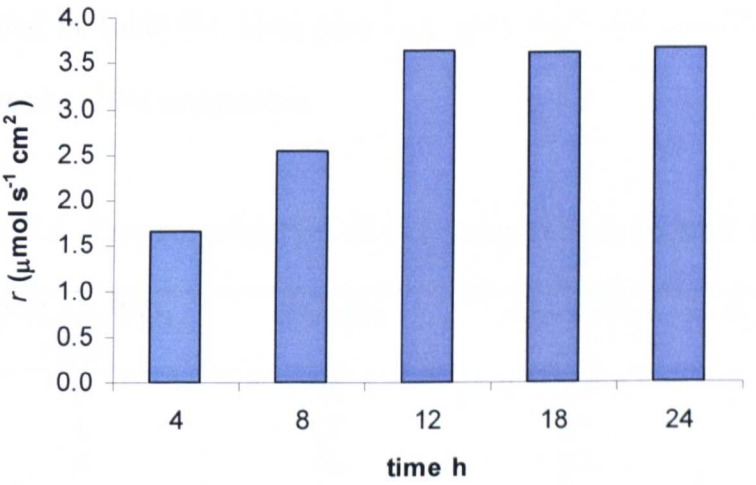

Fig. 7. 14. Reaction rate of mixed oxide 10% wt $(NH_4)_{0.33}WO_3$ loading prepared with 1:1 ethanol-water ratio during solvothermal process at different holding times. Reaction rates are per unit surface area of irradiated coated supports.

7.3.4 Optimisation of synthesis parameters: Effect of $(NH_4)_{0.33}WO_3$ loading

7.3.4.1 Material properties

Mixed oxide samples with $(NH_4)_{0.33}WO_3$ percentage between 1 and 40% wt were prepared using a solution 1:1 ethanol-water, reaction temperature of 150 °C and reaction time of 12 h. Pure TiO_2 and all mixed oxides were white powders, while by treatment of ammonium metatungstate a very fine, light green powder was obtained.

The structural properties of the nanocomposites were measured from duplicate XRD and N_2 adsorption–desorption analyses, and the results are reported in Table 7.4. Data relative to pure TiO_2 and pure $(NH_4)_{0.33}WO_3$ are also reported for comparison.

Table 7.4. Textural properties of TiO_2 samples with different WO_3 loading

$(NH_4)_{0.33}WO_3$ (%wt)	D [a] (nm)	SA [b] (m^2/g)	V_{PORE} [c] (cm^3/g)
0	30	100	0.30
1	28	86	0.17
5	26	87	0.21
10	23	136	0.22
20	21	102	0.24
40	18	99	0.20
100	-	7.6	-

[a] Diameter calculated from the broadening of the (101) anatase peak using Scherrer's equation. [b] Specific surface area determined using the BET method in the range 0.05<P/P0<0.35. [c] BJH desorption pore volume calculated between 2 and 300 nm

The anatase peak positions did not shift in the mixed oxides, indicating that the two oxides were present as distinct crystals and solid solutions were not formed, for all $(NH_4)_{0.33}WO_3$ loadings. The $(NH_4)_{0.33}WO_3$ peaks were not

detectable in material with 1% wt of $(NH_4)_{0.33}WO_3$, but started appearing from concentration of 5% wt of $(NH_4)_{0.33}WO_3$. Increasing the W oxide percentage, the $(NH_4)_{0.33}WO_3$ diffraction peaks increased in intensity and became sharper. In literature the same composite XRD pattern can be found in the work by Yang and colleagues although the crystal phase of $(NH_4)_{0.33}WO_3$ was not identified by the authors (Yang *et al.*, 2002). In Yang's work the Ti/W composites are obtained by a sol-gel method using $Ti(OBu)_4$ and ammonium tungstate in anhydrous alcohol at pH 10, followed by calcinations of obtained xerogels at 400 °C. In Yang's samples the W bronze was not detectable for concentration less than 40%wt. This might be an indication that the formation of W bronze by the novel hydrothermal process leads to a material with higher crystallinity, thus detectable even at very low concentrations.

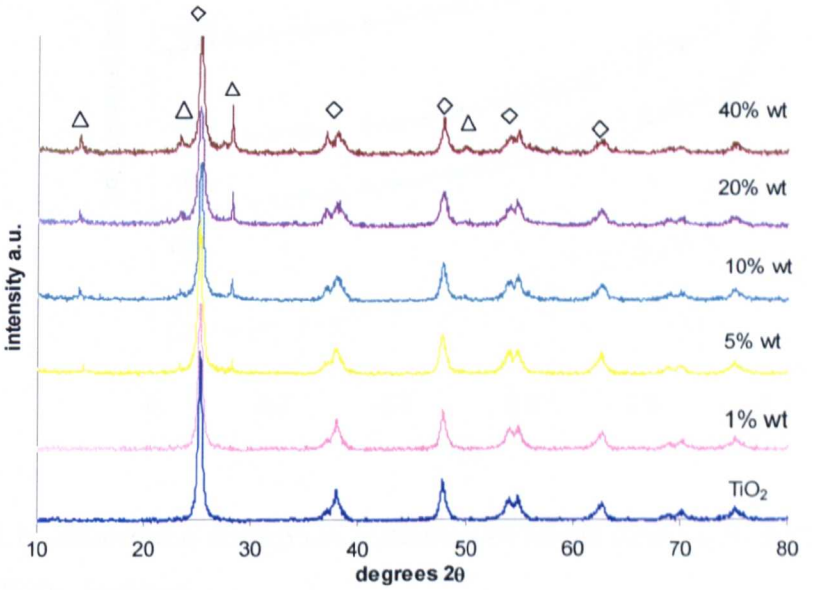

Fig. 7.15. XRD patterns of $TiO_2/(NH_4)_{0.33}WO_3$ composite with different $(NH_4)_{0.33}WO_3$ loading (◇=TiO_2; △=$(NH_4)_{0.33}WO_3$).

The anatase crystallite size as calculated from XRD patterns was found to be in the range 18–30 nm. The WO_3 loading was found to affect the size of the

anatase crystals in the nanocomposites with an inverse relationship, conversely the $(NH_4)_{0.33}WO_3$ loading did not significantly affect the porosity properties of the mixed oxides (i.e. pore size and pore volume).

Similar shapes of the isotherms suggest that the porosity of the mixed oxide nanocomposites is very similar to that of pure TiO_2 and both types of material have a relatively wide pore size distribution in the mesopore size range. Pure TiO_2 shows a sensibly higher pore volume compared with the mixed oxides (Table 5.4). This property can be also attributed to the presence of more interparticle voids in the material.

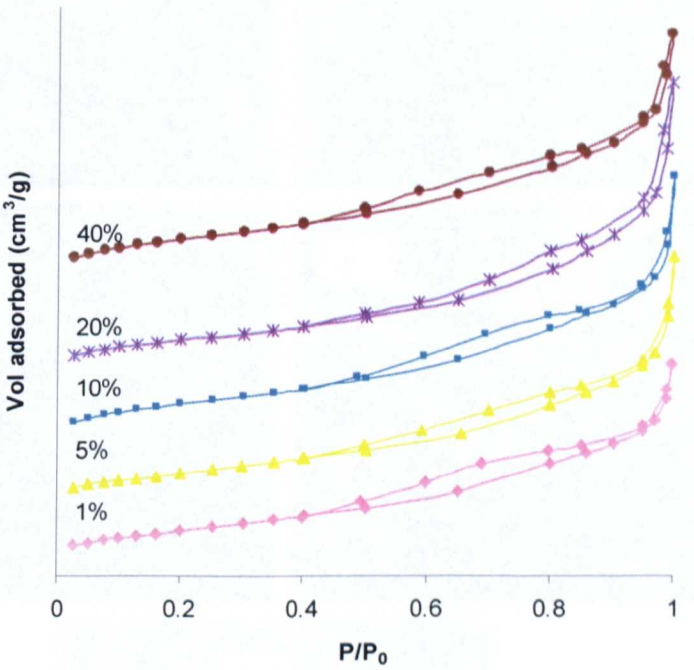

Fig. 7.16. N_2 adsorption-desorption isotherms of mixed oxide with different $(NH_4)_{0.33}WO_3$ loadings.

These observations were confirmed by morphological analysis carried out by SEM. The SEM micrographs shown in Fig. 7.17 provide visualisation of the textural properties of large portions of materials. Pure TiO_2 is made up of irregularly shaped aggregates with sizes between 0.1 and 1 μm.

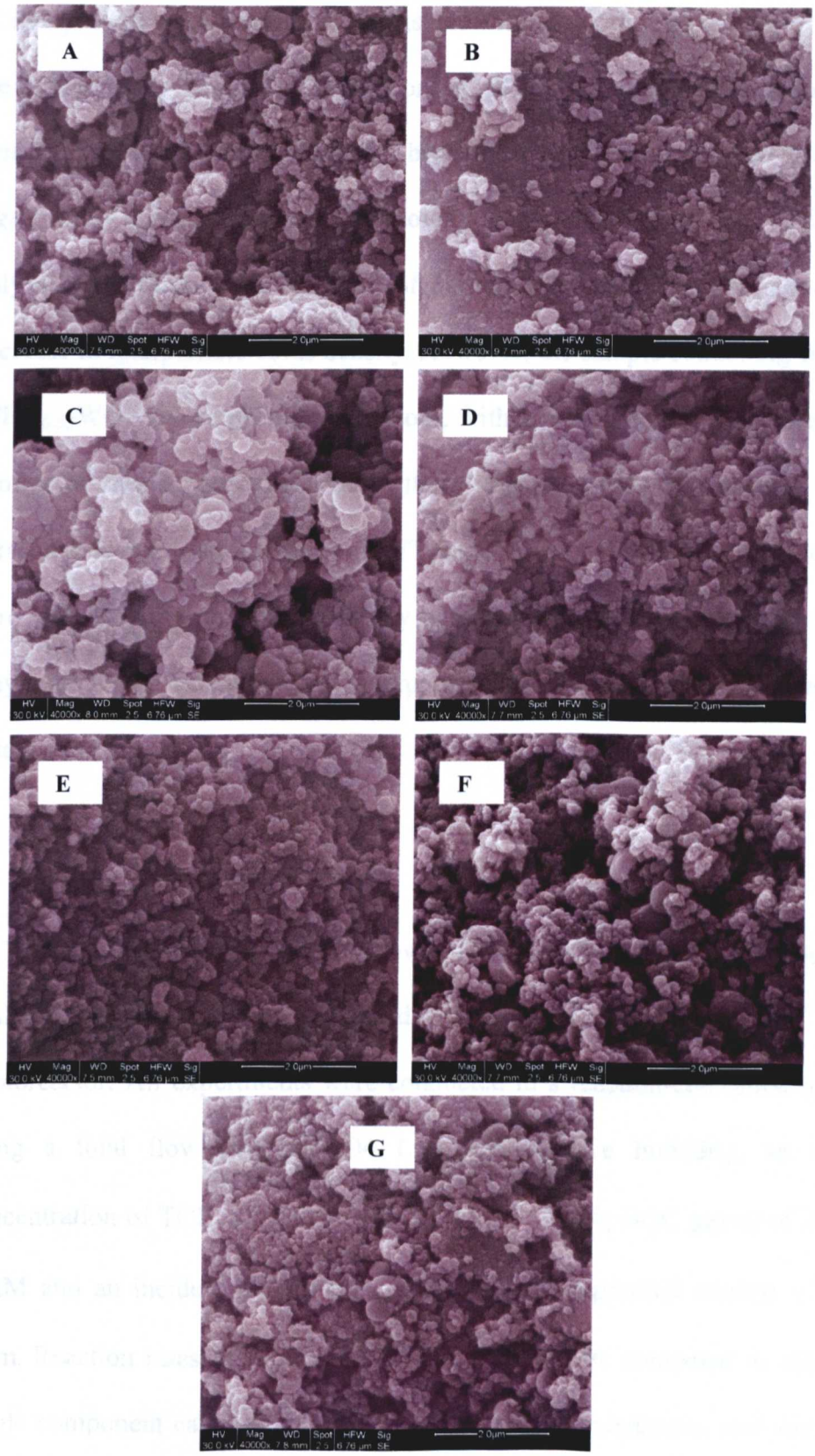

Fig. 7. 17. SEM micrographs of pure TiO_2 (A); pure $(NH_4)_{0.33}WO_3$ (B); mixed oxides with 1% (C); 5% (D); 10% (E) 20% (F) 40% (G) $(NH_4)_{0.33}WO_3$ content.

The particles generally exist in loose aggregates with a significant quantity of interparticle voids, which is consistent with the sorption data and justifies the higher pore volume. Comparison of SEM micrograph shows that the presence of ammonium tungstate bronze in the mixed oxides does not significantly affect the particle morphology. In the mixed oxides can be noticed only a slight increase in the level of particle aggregation and an associated decrease in interparticle voids density. However, the sample containing 10% wt $(NH_4)_{0.33}WO_3$ shows peculiar behaviour, with a morphological structure more similar to that of pure TiO_2 but with a slight increase in porosity, which corroborates with an increase in BET surface area (Table 5.5). Conversely, pure $(NH_4)_{0.33}WO_3$ exhibits a highly aggregated particle morphology, which may explain the lower level of interparticle voids evident from the sorption data.

7.3.4.2 Photocatalytic activity

The photocatalytic activity of novel $TiO_2/(NH_4)_{0.33}WO_3$ materials was evaluated in the gas phase photodegradation of TCE in the flat plate photoreactor. All experiments were conducted in a reaction-controlled regime using a total flow rate of 0.04 L s, 8% relative humidity, an initial concentration of TCE in synthetic air (20% O_2, 80% N_2; BOC gases) of 24.8 ± 2 μM and an incident photon flux (UVA) on the supported catalyst of 5.53 W/m. Reaction rates of the mixed oxide samples were compared to those of single component catalysts evaluated under the same conditions, and with that of commercial TiO_2 Degussa P-25 reference catalyst.

No TCE degradation was detected in the dark or in the absence of catalyst. Therefore, all variation in TCE concentration was ascribed to the photocatalytic activity of the catalyst.

Results on photocatalytic experiments are shown in Fig. 5.17. Pure $(NH_4)_{0.33}WO_3$ did not show any photocatalytic activity towards TCE under the operating conditions used.

In this study, the activity of the hydrothermal TiO_2 sample was similar to that of P-25. This result confirms the efficacy of the hydrothermal synthesis using $TiOSO_4$ as precursor for pure highly active TiO_2 preparation (Kolen'ko *et al.*, 2004).

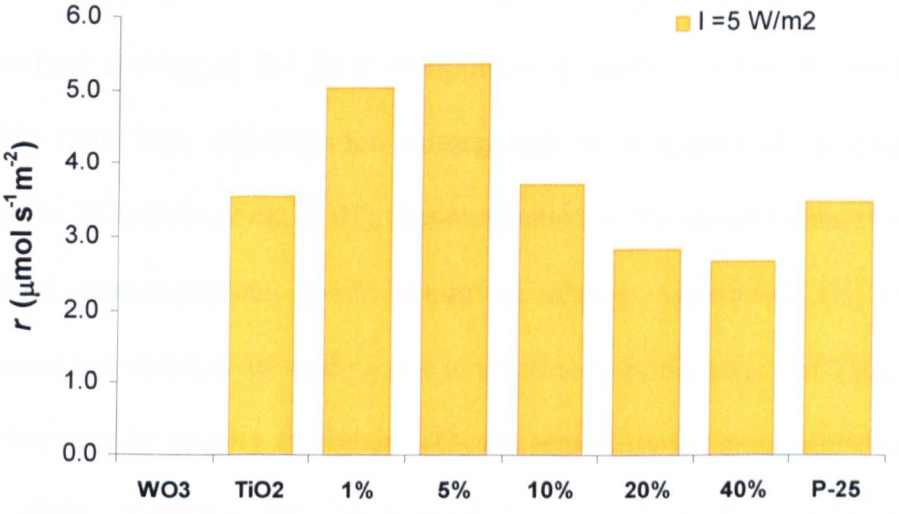

Fig. 7. 18. Reaction rate of mixed oxide with different $(NH_4)_{0.33}WO_3$ loadings prepared with 1:1 ethanol-water ratio for 12 hours. Initial TCE concentration was 24.8 ± 2 μM, 8% RH, flowrate: 0.04 L/s. Reaction rates are per unity surface area of irradiated support.

The nanocomposites with $(NH_4)_{0.33}WO_3$ contents of 1–5% wt showed up to 42% higher photocatalytic activity compared to that of TiO_2 despite having a lower surface area (Table 5.5). Composite with 10%wt $(NH_4)_{0.33}WO_3$ shows

activity comparable with pure TiO_2 and P-25, while for $(NH_4)_{0.33}WO_3$ loadings of 20 and 40% wt a reduced activity is recorded.

The photocatalytic activity of the $TiO_2/(NH_4)_{0.33}WO_3$ composites prepared by the novel one step synthesis developed in this work reaches an optimum $(NH_4)_{0.33}WO_3$ loading of 5%wt, and then decreases for higher W bronze loadings. Similar behaviour has been reported in literature for Ti/W composites prepared by ball milling of pure anatase and monoclinic WO_3 (Shifu *et al.*, 2005), and for Ti/W coatings prepared by sol-gel (Rampaul *et al.*, 2003, G. *et al.*, 1996, Bosc *et al.*, 2006). Also a ternary system composed of $WO_3/SiC/TiO_2$ showed the same behaviour (Keller *et al.*, 2003). In all these cases WO_3 was found to be inactive as photocatalyst and the maximum photocatalytic activity in the Ti/W composites is reached at low W loading, max 10% mol. This concentration corresponds to a theoretical monolayer coverage on TiO_2 (Eibl *et al.*, 2001). Rationalisation of the experimental results arise from considerations about improved charge separation of Ti/W nanocomposites with low W loading due to electron trapping action of WO_3.

The decrease in activity at higher WO_3 concentration is considered due to dilution effect of inactive WO_3 component. In contrast, Fuerte at al report a Ti/W mixed oxide obtained by microemulsion synthesis where the activity for photodegradation of toluene under visible light, increases with WO_3 content in orthorhombic crystalline form (Fuerte *et al.*, 2002). Orthorombic WO_3 alone was also found to be active under visible light for the degradation of toluene, which explains the improvement of activity at higher loadings.

Another important factor that influences the activity of TiO_2/WO_3 composites is the surface acidity. WO_3 is 15 times more acidic than TiO_2 (Tae

Kwon *et al.*, 2000) therefore its presence in the nanocomposite results in improved adsorption of hydroxyl and water at the surface and can modify the affinity of organic substrates for the catalyst surface, and as a consequence, the adsorption equilibrium and photooxidation activity of the catalyst.

A linear correlation between surface acidity and photocatalytic activity was found for decomposition of DCB by P-25 (Papp *et al.*, 1994). Loading WO_3 by impregnation on P-25 was found to increase the surface acidity of the resulting materials. The optimized photocatalyst was found 3.6% WO_3 content which correspond the maximum surface acidity. Kwon and colleagues report a value of 3% for WO_3 loading for maximum surface acidity and optimum degradation rate of 2-propanol and benzene in gas phase (Tae Kwon *et al.*, 2000). Loading of amorphous WO_3 improves the surface acidity as recently reported by Akurati and co-workers in their study on degradation of methylene blu in liquid phase by flam-made TiO_2/WO_3 nanoparticles (Akurati *et al.*, 2008). Recently, a novel TiO_2/WO_3 composite made of anatase and monoclinic WO_3 has been developed by surfactant assisted hydrothermal process followed by calcination (Ke *et al.*, 2008). Composites with 1:3, 4:1 and 1:1 TiO_2/WO_3 molar ratio show improved photocatalytic activity than pure TiO_2 obtained following in the same experimental conditions, for degradation of Rhodamine B in aqueous phase. The best composite was the 1:1 TiO_2/WO_3, which showed activity comparable with that of Degussa P-25.

An improved activity of the composite compared with pure components can be the result of the synergic effect of two or all the above factors, but the determination of the contribution of each factor to is difficult, as it depends on many variables such as composite preparation, crystal composition etc

The experimental results relative to the $TiO_2/(NH_4)_{0.33}WO_3$ nanocomposites prepared in this work show that $(NH_4)_{0.33}WO_3$ is not photocatalytically active. During the optimization of synthesis parameters, the crystallization of $(NH_4)_{0.33}WO_3$ component was found to be of fundamental importance. In fact, materials that did not show $(NH_4)_{0.33}WO_3$ diffraction pattern were found to be the less active for TCE photodegradation. The enhancement in the degradation rate compared with plain TiO_2 can therefore be attributed to presence of hexagonal WO_3, which lead to improved charge separation. Optimum loading corresponds with monolayer coverage, confirming previously reported results discussed above. However, at $(NH_4)_{0.33}WO_3$ loadings of 10% wt or higher, the activity reduced as a result of the dilution effect of the inactive $(NH_4)_{0.33}WO_3$ phase.

7.3.5 Studies at different light intensities

The dependence of reaction rate on irradiation intensity in the range 5-21 W/m^2 for novel $TiO_2/(NH_4)_{0.33}WO_3$ composites was studied. Photon flux was controlled by using 1, 3 and 5 UVA lamps kept at 10.5 cm from the catalyst surface. This distance has been proven to assure homogeneous illumination on the catalyst surface (Salvado-Estivill, 2007).

The reaction rates obtained for the composite catalysts and P-25 at the three intensities studied are reported in Fig. 7.19. By comparison among different nanocomposites we can see that for high light intensities the mixed oxides with 1 wt % $(NH_4)_{0.33}WO_3$ is most active. The reaction rate decreased steadily with increasing $(NH_4)_{0.33}WO_3$ loading in the catalyst for the three light intensities investigated.

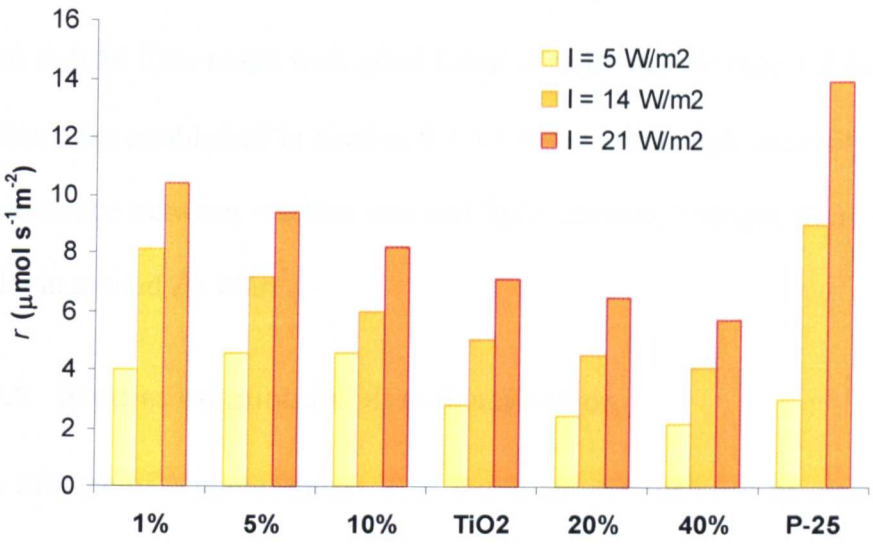

Fig. 7. 19. Reaction rate of mixed oxides at different light intensities. Initial TCE concentration was 24.8 ± 2 μM, 8% RH, flowrate: 0.04 L/s. Reaction rates are per unity surface area of irradiated support.

Table 7. 5. Effect of light intensity (5.0-21 W/m^2) on TCE reaction rate of $TiO_2/(NH_4)_{0.33}WO_3$ nanocomposites with different $(NH_4)_{0.33}WO_3$ loading: values of α and correlation coefficient R.

% wt $(NH_4)_{0.33}WO_3$	α	R
TiO_2	0.64±0.05	0.984
1	0.63±0.03	0.979
5	0.54±0.03	0.998
10	0.55±0.03	0.997
20	0.66±0.05	0.999
40	0.65±0.05	0.997

However, it is interesting to observe that the reaction rates of the composites at the photon flux of 14 and 21 W/m^2 are much lower than those of Degussa P-25. Moreover, increasing the photon flux, the difference in reaction rates between the composites and P-25 becomes larger. This is a clear indication that in the range of light intensities under study, the correlation of reaction rate and photon flux is different for P-25 and for the synthesised photocatalysts.

For mixed oxides and TiO_2 obtained by same hydrothermal process, values of α are in 0.54-0.66 range with good linear correlations, as reported in Table 7.5. It has been established in Section 5.4.5.1.1 that in this light intensity range, the dependence between reaction rate and light intensity changes from first to 0.6 order at around 20 W/m^2.

7.3.6 Studies on photocatalyst deactivation

The lifetime of a photocatalyst is an important parameter to be considered for the evaluation of its practical and commercial feasibility. Catalyst deactivation is a problem frequently encountered in photocatalysis (Sauer and Ollis, 1996). Usually the deactivation is due to refractive oxides produced during the photocatalytic process that are irreversibly absorbed at the catalyst surface. This issue has been widely studied and documented for toluene degradation on TiO_2 where benzoic acid formed during the oxidation process strongly bonds to catalyst surface, occupying active sites and leading to deactivation of the catalyst. Deactivation has been described in photodegradation of N and S containing contaminants (Ollis). Concerning TCE, deactivation of TiO_2 in gas phase reaction due to adsorbed CO and CO_2 on catalyst surface has been reported (Larson and Falconer, 1994).

To evaluate the lifetime of the novel $TiO_2/(NH_4)_{0.33}WO_3$ photocatalyst, TCE conversion was recorded during a 49 hours experiment, consisting of 2 cycles of illumination for 24 hours, separated by a dark period of 2.5 hours. The experiment was carried out using our best TiO_2/WO_3 composite with 5% wt WO_3 content; TCE feed concentration = 29 μmol. Light intensity was 5.12 W/m^2

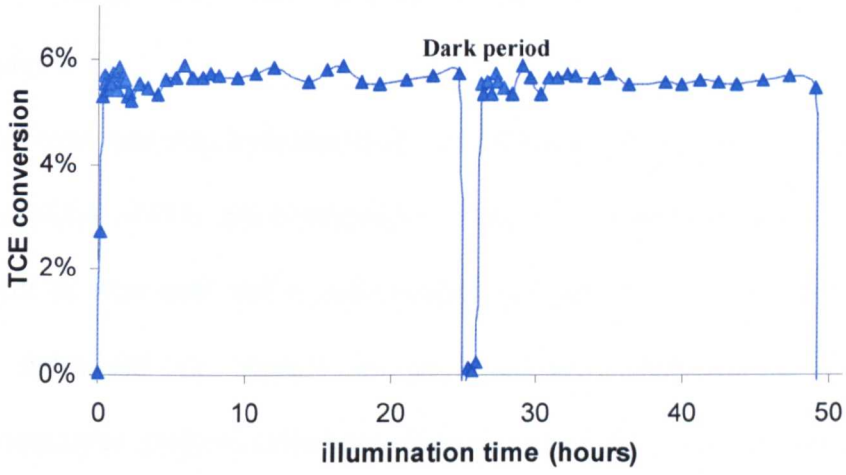

Fig. 7. 20. TCE conversion for 5% wt $(NH_4)_{0.33}WO_3$ over time; [TCE]i = 29 μmol; I= 5.12 W/m^2.

The experimental result shows no deactivation of the $TiO_2/(NH_4)_{0.33}WO_3$ catalyst with irradiation time during the whole experiment. TCE conversion of 5.6±0.5% was rapidly reached by the system and kept constant until the end of the first irradiation cycle, and recovered during the second cycle.

7.4 Summary

Two different $TiO_2/(NH_4)_{0.33}WO_3$ systems have been studied for photodegradation of TCE in the gas phase: a layered structure and a mixed oxide thick film.

The layered structured system demonstrates an interesting surface morphology that leads to useful photoelectrochemical properties. However, no photodegradation of TCE in gas phase was observed under UV and visible light. The complete inactivity of the layered materials was ascribed to the high

WO_3 loading which deactivate the system due to its low rate of electron transfer to O_2.

A novel one step hydrothermal synthesis was developed for preparation of $TiO_2/(NH_4)_{0.33}WO_3$ nanocomposite. Reaction conditions were studied in respect to structural and crystallographic properties of the resulting material, and optimised in respect to photocatalytic oxidation of TCE. Best photocatalytic performances were found for low $(NH_4)_{0.33}WO_3$ loading (up to 5%). Effect of light intensity and possible deactivation of the nanocomposites were also evaluated, showing a half order dependence of reaction rate with light intensity for synthesised photocatalysts and no deactivation after 50 hours of reaction.

Chapter 8

Conclusions and reccommendations

8.1 Conclusions

The aim of this research was the development, optimisation and comparison of TiO_2-based photocatalysts with enhanced photocatalytic activity for the photo-oxidation in the gas phase for indoor air application. Trichloroethylene, a common volatile organic compound, was chosen as probe pollutant.

Three different TiO_2-based photocatalytic systems have been studied: pristine TiO_2, N-doped TiO_2 and TiO_2/WO_3. For the photocatalyst preparation, modified sol-gel and/or hydrothermal synthesis approaches were used.

The synthesis parameters were varied in order to study their impact on photocatalysts' properties and activity. The materials properties were characterised by a wide range of analytical techniques such as X-ray diffraction, N_2 adsorption, electron microscopies, diffuse reflectance and X-ray photoelectron spectroscopy. The photocatalytic properties were evaluated in a flat-plate single-pass photocatalytic reactor, at initial TCE concentration in the μM range, RH of 8%, flowrate of 0.04 L/s. The photoactivity was systematically studied at different incident light intensities, in the range 5-41 W/m^2 and compared with the activity of commercial material TiO_2 P-25 as reference photocatalyst. The structural and morphological properties of synthesised photocatalyst were correlated to the structural and morphological properties of the materials.

8.1.1 Studies on pristine TiO_2

A wide range of mesoporous bare TiO_2 were prepared by a modified sol-gel procedure, consisting of a hydrolysis-condensation step followed by a

crystallization process. The effect of acidic catalysis during the hydrolysis-condensation reaction and the impact of calcination and hydrothermal treatment as crystallization methods were fully investigated.

Depending on the crystallization process, the materials show significant morphological and structural properties. The impact of crystallization parameters on crystal growth was assessed. In the case of calcination it was possible to modulate with high reproducibility the titania crystal dimension, by increasing the firing temperature in the range 300-800 °C. An increase in the crystal size was achieved by increasing the calcination temperature regardless the addition of acid during the hydrolysis-condensation step of the amorphous TiO_2. In the case of hydrothermal process an increase in crystal size was found by increasing the water content in the H_2O/ethanol reaction media. Particle size in the range 13-64 nm and 5-11 nm were obtained for calcination and hydrothermal process respectively, to which correspond surface areas in the range 100-33 and 250-170 m^2/g.

It was found that acidic sol-gel preparation yield to TiO_2 materials with significant differences in particles morphology and porosity compared with materials prepared under uncatalysed sol-gel and crystallised at same conditions. For a given crystal size, the morphologic difference leads to a reduction of surface area.

The photoactivity under UVA irradiation strongly depends on the crystal size of titania and also on the presence and percentage of rutile in the photocatalyst. A linear correlation between the photocatalytic activity and the crystal size was found as long as no rutile was present in the sample. Pure anatase obtained by uncatalysed sol-gel and calcined at temperature between

400 and 600 °C show an enhanced photocatalytic activity compared with TiO_2 P-25. The optimum anatase crystal size of 28 nm exhibits a photocatalytic activity that exceeds that of P-25 by a 2 folds.

The correlation between crystal size and photoactivity for anatase was attribute to the faster interfacial charge transfer rate at catalyst surface. The presence of rutile was found to have a detrimental effect on the overall photoactivity probably due to its low activity towards TCE photodegradation.

8.1.2 Studies on N-doped TiO_2

The best performing pristine TiO_2 were doped with N in the attempt of obtaining a visible active photocatalyst. Different N insertion levels in the titania crystal lattice were achieved by sol-gel and hydrothermal procedures, with the latter leading to higher N-doping. However, no photocatalytic activity under visible illumination was recorded under low irradiation intensities. Moreover, the activity of the original bare TiO_2 materials under UVA light was reduced by doping, probably due to higher density of recombination centre associated with the N doping.

8.1.3 Studies on $TiO_2/(NH_4)_{0.33}WO_3$ systems

The importance of photocatalyst design and relative spatial arrangement in mixed oxide photocatalysts was assessed during this study. A layered system composed of anatase TiO_2 deposited on an layer of monoclinic WO_3 was found to be photocatalytic inactive under UVA and visible light for photodegradation of TCE. By comparison with similar systems reported in the literature, the inactivity of these layered photocatalytic systems was ascribed to the high WO_3

loading which deactivates the system due to its low rate of electron transfer to O_2.

In the frame of studies about TiO_2/WO_3 mixed photocatalytic systems, a novel one-step hydrothermal synthesis was developed and optimised for the preparation of $TiO_2/(NH_4)_{0.33}WO_3$ nanocomposite with high photocatalytic activity at low UVA intensity. Synthesis parameters such as reaction time, solvent composition and WO_3 loading were optimised with respect to the photocatalytic oxidation of TCE. Best material was $TiO_2/(NH_4)_{0.33}WO_3$ with 5% wt $(NH_4)_{0.33}WO_3$ loading prepared by hydrothermal reaction at 150 °C for 12 hours, in mixture 1:1 water-ethanol.

The studies on the dependence of reaction rate on light intensity of the different set of samples show reaction orders between half and first order, and allow to evidence that the intensity threshold for transition from first order to half order, is different for the different photocatalysts.

8.1.4 Practical implications

The practical application of photocatalytic processes based on the use of TiO_2 in indoor air remediation devices requires the development of photocatalyst capable to perform high conversions, possibly in a sustainable way. The photocatalysts prepared during this research, exhibit a substantial potentiality for the implementation of indoor air cleaning technologies. These materials exhibit enhanced photactivity especially at low incident UVA light intensities. This is a fundamental requirement for the implementation of a cost-effectiveness and sustainable photocatalytic technology in commercial devices

for indoor air treatments. However, the coating technology used for catalyst immobilisation must be optimized in order to guarantee stability under operational conditions.

8.2 Recommendations for future work

The results achieved during this work open to several possibilities for further work concerning the study of fundamental aspects of the photocatalytic process and the applicability of the optimized photocatalysts developed in this thesis for practical applications in indoor air treatment.

- The major limitation in the evaluation of the photocatalysts prepared in this work concerns its immobilisation. A suitable immobilisation method for the preparation of stable coatings must be developed and assessed.
- A high activity has been proven for the photo-oxidation of TCE as model pollutant. Therefore, it is suggested the evaluation of the photocatalytic behaviour of the optimised photocatalysts towards other gaseous substrates.
- The evaluation of the catalysts for the abatement of multicomponent VOCs systems reproducing the air composition and pollution concentration found in enclosed environments is also highly recommended. This investigation would assess the feasibility of the materials in real indoor air conditions. It would also provide important insights for the elucidation of reaction kinetics and mechanisms in multicomponent systems.

- Further research concerning the optimisation of the photocatalysts for visible light activation is needed. The evaluation of prepared N-doped samples under high irradiation intensity in the visible light range is also advised.
- In this thesis, the evaluation of the photocatalysts performances was restricted to a laboratory scale. Considering the practical implication of this research, the scale up of the photocatalytic system and the testing of the best photocatalysts in photocatalytic air cleaning prototypes is strongly encouraged.
- The applicability of TiO_2 materials is not confined to the field of photocatalysis but concern various research topics such as energy storage and H_2 production. Thus, expanding the field of application of the optimised TiO_2 based materials developed in this thesis is highly recommended.

Bibliography

AKIRA FUJISHIMA, T. N. R., DONALD A. TRYK (2000) Titanium Dioxide photocatalysis. *Journal of Photochemistry and Photobiology C: Photochemistry Reviews,* 1, 1-21.

AKURATI, K. K., VITAL, A., DELLEMANN, J.-P., MICHALOW, K., GRAULE, T., FERRI, D. & BAIKER, A. (2008) Flame-made WO_3/TiO_2 nanoparticles: Relation between surface acidity, structure and photocatalytic activity. *Applied Catalysis B: Environmental,* 79, 53-62.

ALBERICI, R. M., MENDES, M. A., JARDIM, W. F. & EBERLIN, M. N. (1998) Mass spectrometry on-line monitoring and MS_2 product characterization of TiO_2/UV photocatalytic degradation of chlorinated volatile organic compounds. *Journal of the American Society for Mass Spectrometry,* 9, 1321-1327.

ANDREOZZI, R., CANTERINO, M. & MAROTTA, R. (2006) Fe(III) homogeneous photocatalysis for the removal of 1,2-dichlorobenzene in aqueous solution by means UV lamp and solar light. *Water Research,* 40, 3785-3792.

ANPO, M. & TAKEUCHI, M. (2003) The design and development of highly reactive titanium oxide photocatalysts operating under visible light irradiation. *Journal of Catalysis,* 216, 505-516.

ARAÑA, J., DOÑA-RODRÍGUEZ, J. M., GONZÁLEZ-DÍAZ, O., TELLO RENDÓN, E., HERRERA MELIÁN, J. A., COLÓN, G., NAVÍO, J. A. & PÉREZ PEÑA, J. (2004) Gas-phase ethanol photocatalytic degradation study with TiO_2 doped with Fe, Pd and Cu. *Journal of Molecular Catalysis A: Chemical,* 215, 153-160.

ARQUES, A., AMAT, A. M., SANTOS-JUANES, L., VERCHER, R. F., MARÍN, M. L. & MIRANDA, M. A. (2007) 2,4,6-Triphenylthiapyrylium cation as homogeneous solar photocatalyst. *Catalysis Today,* 129, 37-42.

ASAHI, R., MORIKAWA, T., OHWAKI, T., AOKI, K. & TAGA, Y. (2001) Visible-Light Photocatalysis in Nitrogen-Doped Titanium Oxides. *Science,* 293, 269-271.

ATKINS, P. W. (1998) Physical Chemistry, New York, Freeman.

ATTARD, G., BARNES, C. (1998) Surfaces, Oxford; New York, Oxford University Press.

BALÁZSI, C. & PFEIFER, J. (2002) Development of tungsten oxide hydrate phases during precipitation, room temperature ripening and hydrothermal treatment. *Solid State Ionics,* 151, 353-358.

BARRETT, E. P., JOYNER, L. G. & HALENDA, P. P. (1951) The Determination of Pore Volume and Area Distributions in Porous Substances. I. Computations from Nitrogen Isotherms. *Journal of the American Chemical Society,* 73, 373-380.

BLAKE, N. R. & GRIFFIN, G. L. (1988) Selectivity control during the photoassisted oxidation of 1-butanol on titanium dioxide. *Journal Physical Chemistry,* 92, 5697-5701.

BOSC, F., EDWARDS, D., KELLER, N., KELLER, V. & AYRAL, A. (2006) Mesoporous TiO_2-based photocatalysts for UV and visible light gas-phase toluene degradation. *Thin Solid Films,* 495, 272-279.

BOUZAZA, A., VALLET, C. & LAPLANCHE, A. (2006) Photocatalytic degradation of some VOCs in the gas phase using an annular flow reactor: Determination of the contribution of mass transfer and chemical reaction steps in the photodegradation process. *Journal of Photochemistry and Photobiology A: Chemistry,* 177, 212-217.

BRUNAUER, S., EMMETT, P. H. & TELLER, E. (1938) Adsorption of Gases in Multimolecular Layers. *Journal of the American Chemical Society,* 60, 309-319.

CAI, K. F., HE, X. R. & ZHANG, L. C. (2008) Fabrication, properties and sintering of ZnO nanopowder. *Materials Letters,* 62, 1223-1225.

CHATTERJEE, D. & DASGUPTA, S. (2005) Visible light induced photocatalytic degradation of organic pollutants. *Journal of Photochemistry and Photobiology C: Photochemistry Reviews,* 6, 186-205.

CHEN, Y., CRITTENDEN, J. C., HACKNEY, S., SUTTER, L. & HAND, D. W. (2005) Preparation of a Novel TiO_2-Based p-n Junction Nanotube Photocatalyst. *Environmental Scence and Technology,* 39, 1201-1208.

CHEN, Y., STATHATOS, E. & DIONYSIOU, D. D. (2008) Microstructure characterization and photocatalytic activity of mesoporous TiO_2 films with ultrafine anatase nanocrystallites. *Surface and Coatings Technology,* 202, 1944-1950.

CHENG, H., MA, J., ZHAO, Z. & QI, L. (1995) Hydrothermal Preparation of Uniform Nanosize Rutile and Anatase Particles. *Cheistry of Materials,* 7, 663-671.

CHENG, P., DENG, C., DAI, X., LI, B., LIU, D. & XU, J. (2008). Enhanced energy conversion efficiency of TiO_2 electrode modified with WO_3 in dye-sensitized solar cells. *Journal of Photochemistry and Photobiology A: Chemistry,* 195, 1, 144-150.

CHICHINA, M., TICHY, M., CHURPITA, O. & HUBICKA, Z. (2005) *WDS 05 Proceedings of Contributed Papaers, Part II,* 325-331.

CIESLA, P., KOCOT, P., MYTYCH, P. & STASICKA, Z. (2004) Homogeneous photocatalysis by transition metal complexes in the environment. *Journal of Molecular Catalysis A: Chemical,* 224, 17-33.

COMEAP (2004) Guidance on the Effects on Health of Indoor Air Plootants. *[online] Available from: <http:\\advisorybodies.doh.gov.uk/comeap/PDFS/guidanceindoorairqualitydec04.pdf>.*

DE TACCONI, N. R., CHENTHAMARAKSHAN, C. R., RAJESHWAR, K., PAUPORTE, T. & LINCOT, D. (2003) Pulsed electrodeposition of WO_3-TiO_2 composite films. *Electrochemistry Communications,* 5, 220-224.

DE TACCONI, N. R., CHENTHAMARAKSHAN, C. R., WOUTERS, K. L., MACDONNELL, F. M. & RAJESHWAR, K. (2004) Composite WO_3-TiO_2 films prepared by pulsed electrodeposition: morphological aspects and electrochromic behavior. *Journal of Electroanalytical Chemistry,* 566, 249-256.

DEMEESTERE, K., VISSCHER, A. D., DEWULF, J., LEEUWEN, M. V. & LANGENHOVE, H. V. (2004) A new kinetic model for titanium dioxide mediated heterogeneous photocatalytic degradation of

trichloroethylene in gas-phase. *Applied Catalysis B: Environmental,* 54, 261-274.

DENG, X., YUE, Y. & GAO, Z. (2002) Gas-phase photo-oxidation of organic compounds over nanosized TiO_2 photocatalysts by various preparations. *Applied Catalysis B: Environmental,* 39, 135-147.

DHANANJAY S BHATKHANDE, V. G. P. A. A C M. B. (2002) Photocatalytic degradation for environmental applications - a review. *Journal of Chemical Technology & Biotechnology,* 77, 102-116.

DIBBLE, L. A. & RAUPP, G. B. (1990) *Catalysis Letters,* 4, 345.

DIBBLE, L. A. & RAUPP, G. B. (1992) Fluidized-bed photocatalytic oxidation of trichloroethylene in contaminated air streams. *Environmental and Science Technology,* 26, 492-495.

DO, Y. R., LEE, W., DWIGHT, K. & WOLD, A. (1994) The Effect of WO_3 on the Photocatalytic Activity of TiO_2. *Journal of Solid State Chemistry,* 108, 198-201.

DO, Y. R., LEE, W. I., DWIGHT, K. & WOLD, A. (1993) The Effect of WO_3 on the Photocatalytic Activity of TiO_2. *Journal of Solid State Chemistry,* 108, 198-201.

EIBL, S., GATES, B. C. & KNOZINGER, H. (2001) Structure of WO_x/TiO_2 Catalysts Prepared from Hydrous Titanium Oxide Hydroxide: Influence of Preparation Parameters. *Langmuir,* 17, 107-115.

EPA, U.S. (2002) The Inside Story: A Guide to Indoor Air Quality. [online] Available from:<http://www.epa.gov/iaq/pubs/insidest.html.

EPA, U. S. (2008) Ozone Generators that are Sold as Air Cleaners. [online] Available from:< http://www.epa.gov/iaq/pubs/ozonegen.html>

FLEGLER, S. L., HECKMAN, J. W. & KLOMPARENS, K. L. N. Y., W.H. (1993) Scanning and Transmission Electron Microscopy: an Introduction. *Freeman.*

FOUAD, N. E., NOHMAN, A. K. H., MOHAMED, M. A. & ZAKI, M. I. (2000) Characterization of ammonium tungsten bronze $[(NH_4)_{0.33}WO_3]$ in the thermal decomposition course of ammonium paratungstate. *Journal of Analytical and Applied Pyrolysis,* 56, 23-31.

FU, X., CLARK, L. A., ZELTNER, W. A. & ANDERSON, M. A. (1996) Effects of reaction temperature and water vapor content on the heterogeneous photocatalytic oxidation of ethylene. *Journal of Photochemistry and Photobiology A: Chemistry,* 97, 181-186.

FUERTE, A., HERNANDEZ-ALONSO, M. D., MAIRA, A. J., MARTINEZ-ARIAS, A., FERNANDEZ-GARCIA, M., CONESA, J. C., SORIA, J. & MUNUERA, G. (2002) Nanosize Ti-W Mixed Oxides: Effect of Doping Level in the Photocatalytic Degradation of Toluene Using Sunlight-Type Excitation. *Journal of Catalysis,* 212, 1-9.

FUJISHIMA, A. & HONDA, K. (1972) Electrochemical Photolysis of Water at a Semiconductor Electrode. *Nature,* 238, 37-38.

FUJISHIMA, A., KOHAYAKAWA, K. & HONDA, K. (1975) *Journal of the Electrochemical Society,* 1487.

G., M., L., P., A., S., M., V. A., R., C., G., C., C., M., V., R. & G., S. (1996) Influence of tungsten oxide on structural and surface properties of sol–gel prepared TiO_2 employed for 4-nitrophenol photodegradation

Journal of the Chemical Society, Faraday Transactions, 92, 819 - 829.

GAO, W., LI, M., KLIE, R. & ALTMAN, E. I. (2006) Growth and characterization of model oxide catalysts. *Journal of Electron Spectroscopy and Related Phenomena,* 150, 136-149.

GEORGIEVA, J., ARMYANOV, S., VALOVA, E., POULIOS, I. & SOTIROPOULOS, S. (2007) Enhanced photocatalytic activity of electrosynthesised tungsten trioxide-titanium dioxide bi-layer coatings under ultraviolet and visible light illumination. *Electrochemistry Communications,* 9, 365-370.

GEORGIEVA, J., ARMYANOV, S., VALOVA, E., TSACHEVA, T., POULIOS, I. & SOTIROPOULOS, S. (2005) Photoelectrochemical behaviour of electrodeposited tungsten trioxide and electrosynthesised titanium dioxide single component and bilayer coatings on stainless steel substrates. *Journal of Electroanalytical Chemistry,* 585, 35-43.

GOGATE, P. R. & PANDIT, A. B. (2004) A review of imperative technologies for wastewater treatment I: oxidation technologies at ambient conditions. *Advances in Environmental Research,* 8, 501-551.

GORA, A., TOEPFER, B., PUDDU, V. & LI PUMA, G. (2006) Photocatalytic oxidation of herbicides in single-component and multicomponent systems: Reaction kinetics analysis. *Applied Catalysis B: Environmental,* 65, 1-10.

GOUMA, P. I. & MILLS, M. J. (2001) Anatase to rutile transformation in Titania powders. *Journal American Chemical Society,* 84, 619.

GUO, B., LIU, Z., HONG, L. & JIANG, H. (2005) Sol gel derived photocatalytic porous TiO_2 thin films. *Surface and Coatings Technology,* 198, 24-29.

HAMID, M. A. & RAHMAN, I. (2003) Preparation of Titanium Dioxide (TiO2) thin films by sol-gel dip coating method. *Malaysian Journal of Chemistry,* 5, 86.

HAN, Z., ZHU, H., SHI, J., PARKINSON, G. & LU, G. Q. (2007) Preparation of mesoporous cadmium sulfide nanoparticles with moderate pore size. *Journal of Solid State Chemistry,* 180, 902-906.

HARIZANOV, O. A., GESHEVA, K. A. & STEFCHEV, P. L. (1996) Sol-gel and CVD-metal oxide coatings for solar energy utilization. *Ceramics International,* 22, 91-94.

HAWES, W. & TRIPPETT, S. (1968) Steric Hyndrance of the Alkaline Hydrolysis of Phosphinate Esters. *Chemical Communication,* 577.

HENCH, L. L. & WEST, J. K. (1990) The sol-gel process. *Chemical Reviews,* 90, 33-72.

HENNIG, H. (1999) Homogeneous photo catalysis by transition metal complexes. *Coordination Chemistry Reviews,* 182, 101-123.

HIDALGO, M. C., AGUILAR, M., MAICU, M., NAVÍO, J. A. & COLÓN, G. (2007) Hydrothermal preparation of highly photoactive TiO_2 nanoparticles. *Catalysis Today,* 129, 50-58.

HOFFMANN, M. R., MARTIN, S. T., CHOI, W. & BAHNEMANN, D. W. (1995) Environmental Applications of Semiconductor Photocatalysis. *Chemical Reviews,* 95, 69-96.

HSU, C.-S., LIN, C.-K., CHAN, C.-C., CHANG, C.-C. & TSAY, C.-Y. (2006) Preparation and characterization of nanocrystalline porous TiO_2/WO_3 composite thin films. *Thin Solid Films,* 494, 228-233.

HUO, L., ZHAO, H., MAUVY, F., FOURCADE, S., LABRUGERE, C., POUCHARD, M. & GRENIER, J.-C. (2004) Synthesis and mixed conductivity of ammonium tungsten bronze with tunneling structures. *Solid State Sciences,* 6, 679-688.

HURUM, D. C., AGRIOS, A. G., CRIST, S. E., GRAY, K. A., RAJH, T. & THURNAUER, M. C. (2006) Probing reaction mechanisms in mixed phase TiO_2 by EPR. *Journal of Electron Spectroscopy and Related Phenomena,* 150, 155-163.

HURUM, D. C., AGRIOS, A. G., GRAY, K. A., RAJH, T. & THURNAUER, M. C. (2003) Explaining the Enhanced Photocatalytic Activity of Degussa P25 Mixed-Phase TiO_2 Using EPR. *Journal of Physical Chemistry B,* 107, 4545-4549.

HURUM, D. C., GRAY, K. A., RAJH, T. & THURNAUER, M. C. (2005) Recombination Pathways in the Degussa P25 Formulation of TiO_2: Surface versus Lattice Mechanisms. *Journal of Physical Chemistry B,* 109, 977-980.

IEH (2001) Indoor Air quality in the home: Final report on DETR Contract EPG 1/5/12, (Web Report W7) Leicester, UK, Institute for Environmental and Health. *[online] Available from:<http:\\www.le.ac.uk/ieh/publications/publications.html.*

ITO, S., YOSHIDA, S. & WATANABE, T. (2000) Preparation of Colloidal Anatase TiO_2 Secondary Submicroparticles by Hydrothermal Sol-Gel Method. *Chemistry Letters,* 29, 70.

JACOBY, W. A., BLAKE, D. M., NOBLE, R. D. & KOVAL, C. A. (1995) Kinetics of the Oxidation of Trichloroethylene in Air via Heterogeneous Photocatalysis. *Journal of Catalysis,* 157, 87-96.

JACOBY, W. A., NIMLOS, M. R., BLAKE, D. M., NOBLE, R. D. & KOVAL, C. A. (1994) Products, Intermediates, Mass Balances, and Reaction Pathways for the Oxidation of Trichloroethylene in Air via Heterogeneous Photocatalysis. *Environmental Science and Technology* 28, 1661-1668.

JUNG, K. Y. & PARK, S. B. (1999) Anatase-phase titania: preparation by embedding silica and photocatalytic activity for the decomposition of trichloroethylene. *Journal of Photochemistry and Photobiology A: Chemistry,* 127, 117-122.

JUNG, K. Y., PARK, S. B. & IHM, S.-K. (2002) Linear relationship between the crystallite size and the photoactivity of non-porous titania ranging from nanometer to micrometer size. *Applied Catalysis A: General,* 224, 229-237.

KALLALA, M., SANCHEZ, C. & CABANE, B. (1993) Structures of inorganic polymers in sol-gel processes based on titanium oxide. *Physical Review E,* 48, 3692.

KE, D., LIU, H., PENG, T., LIU, X. & DAI, K. (2008) Preparation and photocatalytic activity of WO_3/TiO_2 nanocomposite particles. *Materials Letters,* 62, 447-450.

KELLER, N., BARRAUD, E., BOSC, F., EDWARDS, D. & KELLER, V. (2007) On the modification of photocatalysts for improving visible light and UV degradation of gas-phase toluene over TiO_2. *Applied Catalysis B: Environmental,* 70, 423-430.

KELLER, V., BERNHARDT, P. & GARIN, F. (2003) Photocatalytic oxidation of butyl acetate in vapor phase on TiO_2, Pt/TiO_2 and WO_3/TiO_2 catalysts. *Journal of Catalysis,* 215, 129-138.

KESHMIRI, M., TROCZYNSKI, T. & MOHSENI, M. (2006) Oxidation of gas phase trichloroethylene and toluene using composite sol-gel TiO_2 photocatalytic coatings. *Journal of Hazardous Materials,* 128, 130-137.

KIM, E., WHANG, C., LEE, W. & KIM, Y. (2006) Photocatalytic property of SiO_2/TiO_2 nanoparticles prepared by sol-hydrothermal process. *Journal of Electroceramics,* 17, 899-902.

KIM, J., BONDARCHUK, O., KAY, B. D., WHITE, J. M. & DOHNALEK, Z. (2007) Preparation and characterization of monodispersed WO_3 nanoclusters on $TiO_2(110)$. *Catalysis Today,* 120, 186-195.

KIM, S.-S., KANG, D.-H., CHOI, D.-H., YEO, M.-S. & KIM, K.-W. (2008) Comparison of strategies to improve indoor air quality at the pre-occupancy stage in new apartment buildings. *Building and Environment,* 43, 320-328.

KOLEN'KO, Y. V., BURUKHIN, A. A., CHURAGULOV, B. R. & OLEYNIKOV, N. N. (2003) Synthesis of nanocrystalline TiO_2 powders from aqueous $TiOSO_4$ solutions under hydrothermal conditions. *Materials Letters,* 57, 1124-1129.

KOLEN'KO, Y. V., CHURAGULOV, B. R., KUNST, M., MAZEROLLES, L. & COLBEAU-JUSTIN, C. (2004) Photocatalytic properties of titania powders prepared by hydrothermal method. *Applied Catalysis B: Environmental,* 54, 51-58.

KOMINAMI, H., KATO, J.-I., MURAKAMI, S.-Y., ISHII, Y., KOHNO, M., YABUTANI, K.-I., YAMAMOTO, T., KERA, Y., INOUE, M., INUI, T. & OHTANI, B. (2003) Solvothermal syntheses of semiconductor photocatalysts of ultra-high activities. *Catalysis Today,* 84, 181-189.

KOMORNICKI, S., RADECKA, M. & SOBAS, P. (2004) Structural, electrical and optical properties of TiO_2-WO_3 polycrystalline ceramics. *Materials Research Bulletin,* 39, 2007-2017.

KUO-HUA WANG, HUAN-HUNG, T. & YUNG-HSU, H. (1998) A study of photocatalytic degradation of trichloroethylene in vapor phase on TiO_2 photocatalyst. *Chemosphere,* 36, 2763-2773.

KWON, Y. T., SONG, K. Y., LEE, W. I., J., C. G. & DO, Y. R. (2000) Photocatalytic behavior of WO3-Loaded TiO_2 in an Oxidation Reaction. *Journal of Catalysis,,* 191, 192.

LANGMUIR, I. (1916) The constitution and fundamental properties of solid and liquids. *Journal of the American Chemical Society,* 38, 2221.

LANGMUIR, I. (1918) The adsorption of gases on plane surfaces of glass OF mica and platinum. 40, 1361 - 1403.

LARSON, S. A. & FALCONER, J. L. (1994) Characterization of TiO_2 photocatalysts used in trichloroethene oxidation. *Applied Catalysis B: Environmental,* 4, 325-342.

LARSON, S. A., WIDEGREN, J. A. & FALCONER, J. L. (1995) Transient Studies of 2-Propanol Photocatalytic Oxidation on Titania. *Journal of Catalysis,* 157, 611-625.

LI, X. Z., LI, F. B., YANG, C. L. & GE, W. K. (2001) Photocatalytic activity of WOx-TiO2 under visible light irradiation. *Journal of Photochemistry and Photobiology A: Chemistry,* 141, 209-217.

LIM, T. H. & KIM, S. D. (2004) Trichloroethylene degradation by photocatalysis in annular flow and annulus fluidized bed photoreactors. *Chemosphere,* 54, 305-312.

LIN, C.-F., WU, C.-H. & ONN, Z.-N. Degradation of 4-chlorophenol in TiO_2, WO_3, SnO_2, TiO_2/WO_3 and TiO_2/SnO_2 systems. *Journal of Hazardous Materials,* In Press, Corrected Proof, 450.

LINSEBIGLER, A. L., LU, G. & YATES, J. T. (1995) Photocatalysis on TiO_2 Surfaces: Principles, Mechanisms, and Selected Results. *Chemical Reviews,* 95, 735-758.

LIQIANG, J., BAIFU, X., FULONG, Y., BAIQI, W., KEYING, S., WEIMIN, C. & HONGGANG, F. (2004) Deactivation and regeneration of ZnO and TiO_2 nanoparticles in the gas phase photocatalytic oxidation of n-C_7H_{16} or SO_2. *Applied Catalysis A: General,* 275, 49-54.

LITTER, M. I. (1999) Heterogeneous photocatalysis: Transition metal ions in photocatalytic systems. *Applied Catalysis B: Environmental,* 23, 89-114.

LIVAGE, J. (1998) Sol-gel synthesis of heterogeneous catalysts from aqueous solutions. *Catalysis Today,* 41, 3-19.

LIVAGE, J. J., HENRY, M. & SANCHEZ, C. (1988) Sol-gel chemistry of transition metal oxides. *Progress in Solid State Chemistry,* 18, 259-341.

MAIRA, A. J., YEUNG, K. L., LEE, C. Y., YUE, P. L. & CHAN, C. K. (2000) Size Effects in Gas-Phase Photo-oxidation of Trichloroethylene Using Nanometer-Sized TiO_2 Catalysts. *Journal of Catalysis,* 192, 185-196.

MAIRA, A. J., YEUNG, K. L., SORIA, J., CORONADO, J. M., BELVER, C., LEE, C. Y. & AUGUGLIARO, V. (2001) Gas-phase photo-oxidation of toluene using nanometer-size TiO_2 catalysts. *Applied Catalysis B: Environmental,* 29, 327-336.

MALATO, S., BLANCO, J., VIDAL, A. & RICHTER, C. (2002) Photocatalysis with solar energy at a pilot-plant scale: an overview. *Applied Catalysis B: Environmental,* 37, 1-15.

MANZINI, I., ANTONIOLI, G., BERSANI, D., LOTTICI, P. P., GNAPPI, G. & MONTENERO, A. (1995) X-ray absorption spectroscopy study of crystallization processes in sol-gel-derived TiO_2. *Journal of Non-Crystal Solid,* 192–193, 519-523.

METTS, T. A. & BATTERMAN, S. A. (2006) Effect of VOC loading on the ozone removal efficiency of activated carbon filters. *Chemosphere,* 62, 34-44.

MILLS, A. & HUNTE, S. L. (1997) An overview on semiconductor Photocatalysis. *Journal of Photochemistry and Photobloogy A: Chemistry,* 108, 1.

MINERO, C. (1999) Kinetic analysis of photoinduced reactions at the water semiconductor interface. *Catalysis Today,* 54, 205-216.

MORTERRA, C. (1988) An infrared spectroscopic study of anatase properties. 6. Surface hydration and strong Lewis acidity of pure and sulfate-doped preparations *Journal of the Chemical Society, Faraday Transactions,* 1, 1617.

NAVROTSKY, A., KLEPPA, O. J. & (1967) Enthalpy of the Anatase-Rutile Transformation *Journal of the American Ceramic Society,* 50.

NEFEDOV, V. I. V. I. (1988) X-ray photoelectron spectroscopy of solid surfaces

NGAOTRAKANWIWAT, P. & TATSUMA, T. (2004) Optimization of energy storage TiO_2-WO_3 photocatalysts and further modification with phosphotungstic acid. *Journal of Electroanalytical Chemistry,* 573, 263-269.

NIMLOS, M. R., JACOBY, W. A., BLAKE, D. M. & MILNE, T. A. (1993) Direct mass spectrometric studies of the destruction of hazardous wastes. 2. Gas-phase photocatalytic oxidation of trichloroethylene over titanium oxide: products and mechanisms. *Environmental Science and Technology,* 27, 732-740.

NISHIDE, T., YAMAGUCHI, H. & MIZUKAMI, F. (1995) Crystal modulation of tungsten oxide gels and films prepared by the sol-gel process using 2,4-pentanedione as an organic ligand. *Journal of Materials Science,* 30, 4946-4949.

O'REGAN, B., MOSER, J., ANDERSON, M. & GRAETZEL, M. (1990) Vectorial electron injection into transparent semiconductor membranes and electric field effects on the dynamics of light-induced charge separation. *Journal of Physical Chemistry,* 94, 8720-8726.

OHTANI, B., OGAWA, Y. & NISHIMOTO, S. I. (1997) Photocatalytic Activity of Amorphous-Anatase Mixture of Titanium(IV) Oxide Particles Suspended in Aqueous Solutions. *Journal of Physical Chemistry B,* 101, 3746-3752.

OU, H.-H. & LO, S.-L. (2007) Photocatalysis of gaseous trichloroethylene (TCE) over TiO_2: The effect of oxygen and relative humidity on the generation of dichloroacetyl chloride (DCAC) and phosgene. *Journal of Hazardous Materials,* 146, 302-308.

PAPP, J., SOLED, S., DWIGHT, K. & WOLD, A. (1994) Surface Acidity and Photocatalytic Activity of TiO_2, WO_3/TiO_2, and MoO_3/TiO_2 Photocatalysts. *Chemistry of Materials,* 6, 496-500.

PARIDA, K. M. & SAHU, N. (2008) Visible light induced photocatalytic activity of rare earth titania nanocomposites. *Journal of Molecular Catalysis A: Chemical,* 287, 151-158.

PARK, E.-H., JUNG, J. & CHUNG, H.-H. (2006) Simultaneous oxidation of EDTA and reduction of metal ions in mixed Cu(II)/Fe(III)-EDTA system by TiO_2 photocatalysis. *Chemosphere,* 64, 432-436.

PARK, J. K., MYOUNG, J. J., KYONG, J. B. & KIM, H. K. (2003) Reaction Mechanism for the Hydrolysis of Titanium Alkoxide. *Bulletin of Korean Chemical Society,* 24, 671.

PARMON, V., EMELINE, A. V. & SERPONE, N. (2002) Glossary of terms in photocatalysis amd radiocatalysis. *International Journal of Photoenergy,* 4, 91.

PATIL, P. S., MUJAWAR, S. H., INAMDAR, A. I., SHINDE, P. S., DESHMUKH, H. P. & SADALE, S. B. (2005) Structural, electrical and optical properties of TiO_2 doped WO_3 thin films. *Applied Surface Science,* 252, 1643-1650.

PERKES, P. (2008) Reading on Electron Microscopy. *[online] Available from:<http://acept.asu.edu/PiN/rdg/elmicr/elmicr.shtml*

PRIMET, M., PICHAT, P. & MATHIEU, M. V. (1971) Infrared study of the surface of titanium dioxides. I. Hydroxyl groups *Journal of Physical Chemistry,* 75, 1216.

PUDDU, V., MOKAYA, R. & PUMA, G. L. (2007) Novel one step hydrothermal synthesis of TiO_2/WO_3 nanocomposites with enhanced photocatalytic activity. *Chemical Comunications,* 4749.

QIU, X. & BURDA, C. (2007) Chemically synthesized nitrogen-doped metal oxide nanoparticles. *Chemical Physics,* 339, 1-10.

RAMPAUL, A., PARKIN, I. P., O'NEILL, S. A., DESOUZA, J., MILLS, A. & ELLIOTT, N. (2003) Titania and tungsten doped titania thin films on glass; active photocatalysts. *Polyhedron,* 22, 35-44.

RAN, F. Y., CAO, W., LI, Y. H. & ZHANG, X. N. (2007) Preparation of Nanosize Anatase TiO_2 Powders by Hydrothermal Synthesis *Key Engineering Materials* 336-338, 2017.

RAUPP, G. B., ALEXIADIS, A., HOSSAIN, M. M. & CHANGRANI, R. (2001) First-principles modeling, scaling laws and design of structured photocatalytic oxidation reactors for air purification. *Catalysis Today,* 69, 41-49.

REIS, K. P., RAMANAN, A. & WHITTINGHAM, M. S. (1992) Synthesis of novel compounds with the pyrochlore and hexagonal tungsten bronze structures. *Journal of Solid State Chemistry,* 96, 31-47.

REN, W., AI, Z., JIA, F., ZHANG, L., FAN, X. & ZOU, Z. (2007) Low temperature preparation and visible light photocatalytic activity of mesoporous carbon-doped crystalline TiO_2. *Applied Catalysis B: Environmental,* 69, 138-144.

REYES-CORONADO, D., RODRÍGUEZ-GATTORNO, G., ESPINOSA-PESQUEIRA, M. E., CAB, C., DE COSS, R. & OSKAM, G. (2008) Phase-pure TiO_2 nanoparticles: anatase, brookite and rutile, *Nanotechnology,* 19, 145605.

REYES, L. F., SAUKKO, S., HOEL, A., LANTTO, V. & GRANQVIST, C. G. (2004) Structure engineering of WO_3 nanoparticles for porous film applications by advanced reactive gas deposition. *Journal of the European Ceramic Society,* 24, 1415-1419.

RHEE, C. H., BAE, S. W. & LEE, J. S. (2005) Template -free Hidrothermal Synthesis of High Surface Area Notrogen-doped Titania Photocatalyst Active under Visible Light. *Chemistry Letters,* 34, 660.

ROBERT, D. (2007) Photosensitization of TiO_2 by MxOy and MxSy nanoparticles for heterogeneous photocatalysis applications. *Catalysis Today,* 122, 20-26.

RUTHVEN, D. M. (1984) Principles of Adsorption and Adsorption Processes, New York, Wiley.

SALVADO-ESTIVILL, I. (2007) Photocatalytic Oxidation of Indoor Air Pollutants: Kinetics, Modelling and Experimental validation. *PhD thesis.*

SALVADO-ESTIVILL, I., BRUCATO, A. & LIPUMA, G. (2007a) Two-Dimensional Modeling of a Flat-Plate Photocatalytic Reactor for Oxidation of Indoor Air Pollutants. *Industrial and Engineering Chemistry Research,* 46, 7489-7496.

SALVADO-ESTIVILL, I., HARGREAVES, D. M. & LIPUMA, G. (2007b) Evaluation of the Intrinsic Photocatalytic Oxidation Kinetics of Indoor Air Pollutants. *Environmental Science and Technology,* 41, 2028-2035.

SANCHEZ, C., LIVAGE, J., HENRY, M. & BABONNEAU, F. (1988) Chemical modification of alkoxide precursors. *Journal of Non-Crystalline Solids,* 100, 65-76.

SANGWICHIEN, C., ARANOVICH, G. L. & DONOHUE, M. D. (2002) Density functional theory predictions of adsorption isotherms with hysteresis loops. *Colloids and Surfaces A: Physicochemical and Engineering Aspects,* 206, 313-320.

SAUER M.L. , HALE M.A. & D.F., O. (1995) *Journal of Photochemistry and Photobiology A: Chemistry,* 88, 169.

SAUER, M. L. & OLLIS, D. F. (1994) Acetone Oxidation in a Photocatalytic Monolith Reactor. *Journal of Catalysis,* 149, 81-91.

SAUER, M. L. & OLLIS, D. F. (1996) Catalyst Deactivation in Gas-Solid Photocatalysis. *Journal of Catalysis,* 163, 215-217.

SCHRANK, S. G., JOSÉ, H. J. & MOREIRA, R. F. P. M. (2002) Simultaneous photocatalytic Cr(VI) reduction and dye oxidation in a TiO_2 slurry reactor. *Journal of Photochemistry and Photobiology A: Chemistry,* 147, 71-76.

SCLAFANI, A. & HERRMANN, J. M. (1996) Comparison of the Photoelectronic and Photocatalytic Activities of Various Anatase and Rutile Forms of Titania in Pure Liquid Organic Phases and in Aqueous Solutions. *Journal of Physical Chemistry,* 100, 13655-13661.

SERPONE, N. (1997) Relative photonic efficiencies and quantum yields in heterogeneous photocatalysis. *Journal of Photochemistry and Photobiology A: Chemistry,* 104, 1-12.

SERPONE, N. (2006) Is the Band Gap of Pristine TiO_2 Narrowed by Anion- and Cation-Doping of Titanium Dioxide in Second-Generation Photocatalysts? *Journal of Physical Chemistry B,* 110, 24287-24293.

SERPONE, N., MARUTHAMUTHU, P., PICHAT, P., PELIZZETTI, E. & HIDAKA, H. (1995) Exploiting the interparticle electron transfer process in the photocatalysed oxidation of phenol, 2-chlorophenol and pentachlorophenol: chemical evidence for electron and hole transfer between coupled semiconductors. *Journal of Photochemistry and Photobiology A: Chemistry,* 85, 247-255.

SHANNON, R. D., PASCK, J. A. & (1965) Kinetics of the Anatase-Rutile Transformation , *Journal of the American Ceramic Society,* 48, 391-398.

SHIFU, C., LEI, C., SHEN, G. & GENGYU, C. (2005) The preparation of coupled WO_3/TiO_2 photocatalyst by ball milling. *Powder Technology,* 160, 198-202.

SHIGEYUKI, S. M. & RUSTUM, R. (2000) Hydrothermal synthesis of fine oxide powders. *Bulletin of Material Science,* 23, 453-460.

SHIRAISHI, F., OHKUBO, D., TOYODA, K. & YAMAGUCHI, S. (2005) Decomposition of gaseous formaldehyde in a photocatalytic reactor with a parallel array of light sources: 1. Fundamental experiment for reactor design. *Chemical Engineering Journal,* 114, 153-159.

SING, K. (2001) The use of Nitrogen Adsorption for the Characterisation of Porous materials- A review. *Colloids and Surfaces A: Physicalchemistry and Enineering Aspects,* 187-188, 3.

SOMASUNDARAM, S., CHENTHAMARAKSHAN, C. R., DE TACCONI, N. R., BASIT, N. A. & RAJESHWAR, K. (2006) Composite WO_3-TiO_2 films: Pulsed electrodeposition from a mixed bath versus sequential deposition from twin baths. *Electrochemistry Communications,* 8, 539-543.

SONG, K. Y., PARK, M. K., KWON, Y. T., LEE, H. W., CHUNG, W. J. & LEE, W. I. (2001) Preparation of Transparent Particulate MoO_3/TiO_2 and WO_3/TiO_2 Films and Their Photocatalytic Properties. *Chem. Mater.,* 13, 2349-2355.

TADA, H., KOKUBU, A., IWASAKI, M. & ITO, S. (2004) Deactivation of the TiO_2 Photocatalyst by Coupling with WO_3 and the Electrochemically Assisted High Photocatalytic Activity of WO_3. *Langmuir,* 20, 4665-4670.

TAE KWON, Y., YONG SONG, K., IN LEE, W., JIN CHOI, G. & RAG DO, Y. (2000) Photocatalytic Behavior of WO_3-Loaded TiO_2 in an Oxidation Reaction. *Journal of Catalysis,* 191, 192-199.

TATSUMA, T., TAKEDA, S., SAITOH, S., OHKO, Y. & FUJISHIMA, A. (2003) Bactericidal effect of an energy storage TiO_2-WO_3 photocatalyst in dark. *Electrochemistry Communications,* 5, 793-796.

TERZIAN, R. & SERPONE, N. (1995) Heterogeneous photocatalyzed oxidation of creosote components: mineralization of xylenols by illuminated TiO_2 in oxygenated aqueous media. *Journal of Photochemistry and Photobiology A: Chemistry,* 89, 163-175.

TSAI, S.-J. & CHENG, S. (1997) Effect of TiO_2 crystalline structure in photocatalytic degradation of phenolic contaminants. *Catalysis Today,* 33, 227-237.

WACHS, I. E., KIM, T. & ROSS, E. I. (2006) Catalysis science of the solid acidity of model supported tungsten oxide catalysts. *Catalysis Today,* 116, 162-168.

WANG, C. C. & YING, J. Y. (1999) Sol-Gel Synthesis and Hydrothermal Processing of Anatase and Rutile Titania Nanocrystals. *Chem. Mater.,* 11, 3113-3120.

WARREN, B. E. (1990) X-ray Diffraction, New York, Dover.

WATTS, J. F. (1998) An Introduction to Surface Analysis by XPS and AES, Wiley.

YAMASHITA, H., HARADA, M., MISAKA, J., TAKEUCHI, M., IKEUE, K. & ANPO, M. (2002) Degradation of propanol diluted in water under visible light irradiation using metal ion-implanted titanium dioxide photocatalysts. *Journal of Photochemistry and Photobiology A: Chemistry,* 148, 257-261.

YANAGISAWA, K. & OVENSTONE, J. (1999) Crystallization of Anatase from Amorphous Titania Using the Hydrothermal Technique: Effects of Starting Material and Temperature. *J. Phys. Chem. B,* 103, 7781-7787.

YANG, H., SHI, R., ZHANG, K., HU, Y., TANG, A. & LI, X. (2005) Synthesis of WO_3/TiO_2 nanocomposites via sol-gel method. *Journal of Alloys and Compounds,* 398, 200-202.

YANG, H., ZHANG, D. & WANG, L. (2002) Synthesis and characterization of tungsten oxide-doped titania nanocrystallites. *Materials Letters,* 57, 674-678.

YU, B. F., HU, Z. B., LIU, M., YANG, H. L., KONG, Q. X. & LIU, Y. H. (2008) Review of research on air-conditioning systems and indoor air quality control for human health. *International Journal of Refrigeration,* In Press, Corrected Proof.

YU, J.-G., YU, J. C., CHENG, B., HARK, S. K. & IU, K. (2003a) The effect of F^-doping and temperature on the structural and textural evolution of mesoporous TiO_2 powders. *Journal of Solid State Chemistry,* 174, 372-380.

YU, J., LIU, S., XIU, Z., YU, W. & FENG, G. Synthesis of sulfur-doped TiO_2 by solvothermal method and its visible-light photocatalytic activity. *Journal of Alloys and Compounds,* In Press, Corrected Proof.

YU, J., WANG, G., CHENG, B. & ZHOU, M. (2007) Effects of hydrothermal temperature and time on the photocatalytic activity and microstructures of bimodal mesoporous TiO_2 powders. *Applied Catalysis B: Environmental,* 69, 171-180.

YU, J., YU, H. C., CHENG, B., ZHOU, M. & ZHAO, X. (2006) Enhanced photocatalytic activity of TiO_2 powder (P25) by hydrothermal treatment.*Journal of Molecular Catalysis A: Chemical,* 253, 112-118

YU, J., YU, J. C., LEUNG, M. K. P., HO, W., CHENG, B., ZHAO, X. & ZHAO, J. (2003b) Effects of acidic and basic hydrolysis catalysts on the photocatalytic activity and microstructures of bimodal mesoporous titania. *Journal of Catalysis,* 217, 69-78.

YU, K., ZHAO, J., GUO, Y., DING, X., HARI, B., LIU, Y. & WANG, Z. (2005) Sol-gel synthesis and hydrothermal processing of anatase nanocrystals from titanium n-butoxide. *Materials Letters,* 59, 2515-2518.

YUAN, M., SHAN, Z., TIAN, B., TU, B., YANG, P. & ZHAO, D. (2005) Preparation of highly ordered mesoporous WO_3-TiO_2 as matrix in matrix-assisted laser desorption/ionization mass spectrometry. *Microporous and Mesoporous Materials,* 78, 37-41.

ZHAN, J. H., YANG, X. G., XIE, Y., LI, B. F., QAIN, Y. T. & JIA, Y. B. (1999) A solvothermal route for the synthesis of ammonium tungsten bronze. *Solid State Ionics,* 126, 373-377.

ZHANG, H., YANG, D. & MA, X. (2007) Synthesis of flower-like CdS nanostructures by organic-free hydrothermal process and their optical properties. *Materials Letters,* 61, 3507-3510.

ZHANG, Z., WANG, C. C., ZAKARIA, R. & YING, J. Y. (1998) Role of Particle Size in Nanocrystalline TiO2-Based Photocatalysts. *J. Phys. Chem. B,* 102, 10871-10878.

ZHAO, J. & YANG, X. (2003) Photocatalytic oxidation for indoor air purification: a literature review. *Building and Environment,* 38, 645-654.

ZHOU, M. & YU, J. (2008) Preparation and enhanced daylight-induced photocatalytic activity of C,N,S-tridoped titanium dioxide powders. *Journal of Hazardous Materials,* 152, 1229-1236.

ZUO, G.-M., CHENG, Z.-X., CHEN, H., LI, G.-W. & MIAO, T. (2006) Study on photocatalytic degradation of several volatile organic compounds. *Journal of Hazardous Materials,* 128, 158-163.